

UNIVERSITY of CALIFORNIA
Santa Barbara

**Nonclassical Light Emission From Single Self-Assembled InAs
Quantum Dots**

A dissertation submitted in partial satisfaction of the
requirements for the degree of

Doctor of Philosophy

in

Electrical and Computer Engineering

by

Alper Kiraz

Committee in charge:

Professor Ataç İmamoğlu, Chair
Professor Pierre M. Petroff
Professor Evelyn Hu
Professor Hideo Mabuchi
Professor Mark Sherwin

September 2002

The dissertation of Alper Kiraz is approved:

Chair

September 2002

**Nonclassical Light Emission From Single Self-Assembled InAs
Quantum Dots**

Copyright 2002

by

Alper Kiraz

Acknowledgements

I am very grateful to my advisor Professor Ata İmamoglu for being always enthusiastic, helpful, and inspirational, providing the nutritious experimental and theoretical environment in the group, teaching me how to approach to problems, introducing me to the field, and much more. I would also like to thank to Professors Evelyn Hu, and Pierre Petroff for their collaborations, my other committee members Professors Mark Sherwin, and Hideo Mabuchi for their comments and suggestions.

I would like to thank especially to Dr. Peter Michler, and Dr. Christoph Becher who practically gifted me my Ph.D. I hope I can do the same during my post-doctoral researcher years. I am thankful to Lidong Zhang for his microdisk processing, and Winston V. Schoenfeld for the growth of the quantum dots. I am also grateful to Dr. Bruno Gayral, Stefan Flth, and Dr. Junji Urayama for the joint experiments we have performed, my colleagues Charles Reese for helping me with FDTD simulations, and Kian-Giap Gan for his help with the femtosecond laser.

Curriculum Vitæ

Alper Kiraz

Personal

Born February 5, 1976
İzmir, Turkey

Education

06/2000 – 09/2002 Ph.D. Electrical and Computer Engineering, University of California, Santa Barbara.
Dissertation: A Single Quantum Dot Two Photon Entangled State Generator. Under the supervision of Ataç İmamoğlu

09/1998 – 06/2000 M.S. Electrical and Computer Engineering, University of California, Santa Barbara.

09/1993 – 06/1998 B.S. Electrical-Electronics Engineering, Bilkent University, Ankara, Turkey.

Work Experience

Research Assistant University of California, Santa Barbara (April 1999 - Present)
Experimental Semiconductor Quantum Optics

Teaching Assistant University of California, Santa Barbara
Communication Electronics, Engineering Mathematics (Fall 1998)
Lab Ass. (clean room): Integrated Circuit Design and Manufacturing (Winter 1999)
Lab Ass.: Digital logic (Summer 2001)

Engineering Intership Bilkent University, Ankara, Turkey (Summer 1998)
Computational Electromagnetics

Publications

A. Kiraz, S. Fälth, C. Becher, B. Gayral, L. Zhang, E. Hu, W. V. Schoenfeld, P. M. Petroff, and A. Imamoglu
“Photon correlation spectroscopy of a single quantum dot,”
Phys. Rev. B **65**, 161303(R) (2002).

P. Michler, A. Imamoglu, **A. Kiraz**, C. Becher, M. D. Mason, P. J. Strouse, S. K. Buratto, W. V. Schoenfeld, P. M. Petroff
“Nonclassical radiation from a single quantum dot,” Phys. Stat. Sol. (b) **229** 399-405 (2002).

A. Kiraz, P. Michler, C. Becher, B. Gayral, A. Imamoglu, L. Zhang, E. Hu, W. V. Schoenfeld, and P. M. Petroff
“Cavity-quantum electrodynamics using a single InAs quantum dot in a microdisk structure,” Appl. Phys. Lett. **78**, 3932-3934 (2001).

P. Michler, **A. Kiraz**, C. Becher, Lidong Zhang, E. Hu, A. Imamoglu, W. V. Schoenfeld, and P. M. Petroff,
“Quantum dot lasers using high-Q microdisk cavities,” Phys. Stat. Sol. (b) **224**, 797-801 (2001).

C. Becher, **A. Kiraz**, P. Michler, A. Imamoglu, W. V. Schoenfeld, P. M. Petroff, L. Zhang, and E. Hu,
“Nonclassical radiation from a single self-assembled InAs quantum dot,” Phys. Rev. B **63**, 121312(R) (2001).

T. Sulchek, R. J. Grow, G. G. Yaralioglu, S. C. Minne, C. F. Quate, S. R. Manalis, **A. Kiraz**, A. Aydinler, A. Atalar,
“Parallel atomic force microscopy with optical interferometric detection,” Appl. Phys. Lett. **78**, 1787-1789 (2001).

P. Michler, **A. Kiraz**, C. Becher, W. V. Shoenfeld, P. M.

Petroff, L. Zhang, E. Hu, and A. Imamoglu,
“A quantum dot single photon turnstile device,” *Science* **290**,
2282-2285 (2000).

P. Michler, **A. Kiraz**, L. Zhang, C. Becher, E. Hu, and
A. Imamoglu,
“Laser emission from quantum dots in microdisk structures,”
Appl. Phys. Lett. **77**, 184-186 (2000).

Presentations

Invited Talk: “Single Photons from a Single Quantum Dot,”
Optical Society of America, Annual Meeting, Long Beach,
California (2001).

Poster Presentation: “Generation of regulated single photons
by pulsed excitation of a single InAs quantum dot,” Interna-
tional Conference on Quantum Information, Rochester, New
York (2001).

Invited Talk: “A single quantum dot single photon turnstile
device,” Southwest Quantum Information and Technology Net-
work (SQuInt) Third Annual Meeting, Pasadena, California
(2001).

Postdeadline Paper: “Photon antibunching from a single self-
assembled InAs quantum dot,” International Quantum Elec-
tronics Conference (IQEC), Nice, France (2000) (IPD1.5).

Abstract

Nonclassical Light Emission From Single Self-Assembled InAs Quantum Dots

by

Alper Kiraz

We describe quantum optical experiments using single self-assembled InAs quantum dots in photonic nanostructures. Even though cryogenic temperatures are required to observe their atom-like characteristics, absence of a *trapping requirement* renders quantum dots very useful in a number of experiments previously not demonstrated using atoms.

The inherit two-level nature of their single excitonic and biexcitonic transitions allow the observation of photon antibunching under continuous wave excitation. Under pulsed excitation conditions, the photon antibunching phenomenon gives rise to triggered single photon emission, provided that free-carriers have much shorter lifetimes than quantum dot ground state carriers. This new nonclassical light source, i.e. *single photon turnstile device*, promises applications in quantum cryptography, and quantum information processing.

We have observed weak coupling cavity quantum electrodynamics (cavity-QED) regime by tuning the single excitonic transition into resonance with a high quality factor microdisk whispering gallery mode. Such a coupling that resulted in the enhancement of spontaneous emission rate by at least 3.4, can be used in improving the collection efficiency of our single photon source.

Carrier-carrier interactions also bring additional richness to quantum dot physics allowing the observation of a stable cascade system (biexciton - single exciton cascade) and charged exciton phenomenon. We performed photon correlation measurements that demonstrated the cascaded emission and gave evidence for the

identification of charged emission peaks. Photons emitted by the biexciton - single exciton cascade are also predicted to constitute a two-photon polarization entangled state, similar to the case in atomic cascades. Under nonresonant excitation conditions, we have not observed any polarization correlations; this is probably due to the short spin lifetimes of ground state carriers.

Finally we propose an experimental scheme for observing two-photon interference using the single quantum dot single photon source. Observation of two-photon interference from our single photon source can lead to free space quantum teleportation, and quantum information processing experiments. We demonstrate the results of linewidth measurements under nonresonant continuous wave and pulsed excitation conditions that revealed linewidths as small as $5.6 \mu\text{eV}$. The fact that the measured linewidths were ~ 10 times larger than the transform limited values prevented us from observing two-photon interference.

Contents

1	Introduction	1
2	Self-Assembled InAs Quantum Dots	5
2.1	Growth	5
2.2	Photoluminescence Characteristics	8
2.3	Microdisk Processing	11
3	Photon Antibunching	13
3.1	Degree of Second Order Coherence	14
3.2	Photon Antibunching in Resonance Fluorescence of a Two-Level System	19
3.3	Modelling a Single Quantum Dot as a Three-Level System	21
3.4	Analysis of Photon Antibunching in a Single Quantum Dot	24
3.5	Experiments	26
3.5.1	Hanbury Brown and Twiss Setup	26
3.5.2	Photon Antibunching in Single InAs Quantum Dots	29
3.5.3	Time-Correlated Single Photon Counting Experiments	34
4	Triggered Single Photon Emission	37
4.1	Generation of Single Photons From a Single Two-Level Emitter	39
4.1.1	A Strongly Damped Two-Level Emitter	40
4.1.2	Monte Carlo Simulations	41
4.2	Single InAs Quantum Dot Single Photon Turnstile Device	42
4.2.1	Analysis of a Three-Level Emitter	43
4.2.2	Experimental Results	45
5	Cavity-QED Using Single Quantum Dots	52
5.1	Analysis of Cavity-Single Quantum Dot Interaction	53
5.2	Microdisk Whispering Gallery Modes	56

5.2.1	Analysis of Whispering Gallery Modes	56
5.2.2	Experimental Analysis of Whipering Gallery Modes	59
5.3	Experimental Results	61
5.3.1	Demonstration of the Purcell Effect by Photon Correlation Ex- periments	61
5.3.2	Direct Proof of the Purcell Effect by TCPC Experiments . . .	68
5.4	Spectral Changes in the Quantum Dot and WGM Emissions	72
5.5	Inhibited Spontaneous Emission due to Microdisk Cavities	74
5.5.1	Inhibited Spontaneous Emission Phenomenon	74
5.5.2	Analysis of Inhibited Spontaneous Emission in a Microdisk Cavity	77
6	Photon Correlation Spectroscopy	80
6.1	Analysis of a Three-Level System for Cross-Correlation Measurements	81
6.2	Photon Correlation Spectroscopy Experiments using single Quantum Dots	85
6.3	Comparison of Cascade Emission Experiments using Atoms and Quan- tum Dots	95
6.4	Entangled State Generation Using the Three-Level Cascade in Quan- tum Dots	96
7	Two-Photon Interference	98
7.1	Proposed Scheme	99
7.2	Analysis of Two-Photon Interference	100
7.2.1	Model of a Quantum Dot for Two-Photon Interference	101
7.2.2	Calculation of Coincidence Detection Rate	104
7.2.3	Solution of Two-Photon Interference for Single Quantum Dots	106
7.3	Dephasing in Single Quantum Dots	109
7.4	Experimental Results	113
7.5	p-shell Excitation	116
8	Conclusion	118
8.1	Cavity-QED Experiments	118
8.2	Two-Photon Interference Experiments	120
	Bibliography	121
A	Calculation of $g^{(2)}(\tau)$	130
A.1	Two-Level System with Little Dephasing	130
A.2	Dephased Two-Level System	133

A.3	Comments on the Calculation of Second Order Correlation Functions .	134
B	Jaynes-Cummings Hamiltonian	135
B.1	Rabi Oscillations	135
B.2	Normal Model Splitting	137
B.3	AC Stark Effect	138

Chapter 1

Introduction

For the last two decades quantum optical experiments have been performed mostly using low density atomic beams [1] or trapped single ions [2, 3], revealing various nonclassical phenomena. However due to the stringent experimental requirements in trapping single atoms or single ions, such experiments have not become widely practical. With their atom-like characteristics, self-assembled InAs quantum dots emerge as a material system that can be used in making various quantum optical phenomena more practical. The biggest advantage in quantum dot research is that due to their solid nature, no trapping technique is necessary in performing experiments. Furthermore, as a result of the advanced semiconductor growth techniques, our quantum dots can be grown at very low densities such that we can isolate a single quantum dot within the optical resolution of a regular micro photoluminescence setup, without the need for special near-field or other techniques. Hence, at cryogenic temperatures it is very convenient to investigate the atom-like properties of single quantum dots.

The first experimental result we present in this thesis is the observation of photon antibunching phenomenon in the emission of single InAs quantum dots. This phenomenon is a proof of the two-level nature of the single excitonic transition. As it is shown in Chapter 3, we observed almost ideal photon antibunching signa-

tures which is very promising for further quantum optical experiments. In addition to photon antibunching from the single excitonic emission, we also observed photon antibunching from the biexcitonic emission, this result is presented in Chapter 6.

We demonstrate the triggered single photon source operation from quantum dots in Chapter 4. This is the demonstration of a new type of light source, i.e. *single photon turnstile device*, that already received quite a lot of interest from the community. We believe single photon sources will be stimulating for other quantum optical results in the future. This result once more showed the clear advantage of single quantum dots over single atoms. Although photon antibunching was observed in 1977 [1] using single atoms, single photon operation has not been demonstrated due to experimental difficulties until this year (2002 [4]). In contrast, photon antibunching and triggered single photon source operation from single quantum dots have been demonstrated with a small time separation in the year 2000 [5, 6].

Following these results, in Chapter 5 we show our results on cavity quantum electrodynamics (cavity-QED) using single InAs quantum dots. In this regard, quantum dots have the advantage that due to their semiconductor nature they can be placed in semiconductor microcavities such as micropillar structures, microdisk, or photonic band gap microcavities. With their low mode volumes and relatively high mode quality factors these microcavities are the quantum dot counterparts of the Fabry-Perot cavities used in atomic cavity-QED experiments. We demonstrate an *enhancement* in the spontaneous emission rate of a single excitonic transition of a single quantum dot by a factor of at least 3.4 due to its resonant coupling to a microdisk whispering gallery mode. We also demonstrate that the emission of a single quantum dot can be tuned in resonance with a cavity mode by changing the temperature, providing a tuning range of ~ 3 meV between 4 - 50 K. This weak coupling cavity-QED regime is also important for single photon source operation from single quantum dots. Light emitted from a single quantum dot can be efficiently extracted by coupling it to a microcavity mode. Although microdisk cavities are not suitable for such a purpose due to their non-directional output, our demonstrations

of microcavity mode - quantum dot tunability constitutes a demonstration of the principle.

In addition to the enhancement in the spontaneous emission rate of the single excitonic emission resonantly coupled to a microdisk whispering gallery mode, we observed *inhibition* in spontaneous emission when the emission peak is out of resonance with any whispering gallery modes in a microdisk cavity. As explained in Chapter 5 this is caused by the changed *photonic environment* that modifies the available optical mode density, and zero point field fluctuations such that an inhibition in spontaneous emission rate is observed. Both the small thickness ($d \sim \lambda$) of the microdisk cavities, and the microdisk whispering gallery modes that the quantum dot emission is out of resonance with, have a role in this combined effect. We typically observed inhibition factors of 2 - 4 for different quantum dots located in microdisk cavities.

Three-level nature of the ground state of single InAs quantum dots also allow an experimental quantum optical analysis of a prototype three-level system. From such an analysis, in Chapter 6 we demonstrate the cascaded emission of photons in the ground state of a single quantum dot. This cascaded emission may also lead to generation of polarization entangled photon pairs; however we have not observed this effect, probably due to the short spin lifetimes of ground state carriers. From photon correlation measurements we can clearly identify the single excitonic, and biexcitonic emission peaks of a single quantum dot. Hence, this method is an alternative to the conventional identification of the single excitonic and biexcitonic emission peaks by their power and magnetic field dependent characteristics. In addition, this method provides strong evidence for the identification of charged exciton peak in the single quantum dot spectrum.

In Chapter 7 we present our proposal to obtain two-photon interference using the single quantum dot single photon source. This proposal is motivated by the use of our single photon source in free space quantum information processing in a linear optics quantum computation scheme [7]. Our proposal relies on the interfer-

ence of two consecutive photons emitted from the same quantum dot at the input of a beam splitter. Since the first requirement to observe two-photon interference with our proposal is to achieve transform limited emission, we performed linewidth measurements on single excitonic transitions of single quantum dots. Under nonresonant continuous wave and pulsed excitation conditions we obtained linewidths as small as $5.6 \mu\text{eV}$. However, since these linewidth measurements were still > 10 times larger than the spontaneous emission defined linewidths, we have not succeeded in observing the two-photon interference phenomenon. We discuss the excitation of a single quantum dot from a higher excited state (p-shell) as a method to observe transform limited single photon pulses.

Chapter 2

Self-Assembled InAs Quantum Dots

Single self-assembled InAs quantum dots, also identified as *artificial atoms*, have drawn a large amount of interest from the community, demonstrating an exciting crossing point between semiconductor and atomic physics. By now it is widely accepted that these nanostructures exhibit features in transport [8, 9] and optical spectroscopy [10, 11, 12] that indicate full three dimensional confinement of carriers.

In this chapter it is aimed to give an introduction to the growth and basic optical characteristics of single InAs quantum dots before the discussion of the quantum optical experiments in the following chapters. The processing steps of the microdisk structures are also explained in this chapter as these structures serve as both mesas and microcavities in our experiments. A detailed explanation of the cavity properties of the microdisk structures is given later in Chapter 5.

2.1 Growth

Self-assmebled InAs quantum dots are grown by molecular beam epitaxy (MBE) using the *Stranski-Krastanov* growth method [13]. As illustrated in Fig-

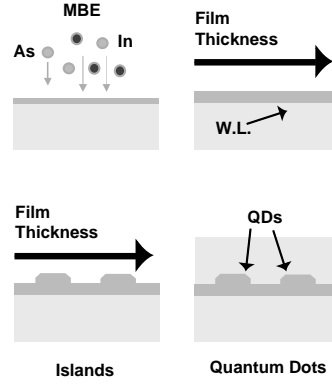


Figure 2.1: Schematic of the InAs quantum dot growth process.

ure 2.1, during the MBE growth, In and As atoms are first deposited on a clean GaAs substrate held at high temperature where they self assemble into smooth epitaxial atomic layers. The layer by layer growth then continues until a build up in the strain and surface energy of the epitaxial film switches the growth to the island mode. This change in the surface morphology is dictated by the minimization of the film energy. The growth of self-assembled quantum dots is finalized by covering the smaller band gap material of the islands with a wider band gap epitaxial film. The formation of a thin wetting layer is inherent to the process. While island formation is initiated at a critical thickness of ~ 1.6 monolayer (9.68 \AA), at the end of the island formation, wetting layer remains with a thickness of ~ 1 monolayer (6.05 \AA).

The quantum dots' exact shape, dimensions and composition are not known accurately. In our samples, size distribution of the quantum dots is controlled by the *partially covered island* (PCI) technique [14, 15], in which, the growth sequence during the capping of InAs islands is modified by introducing growth interruptions. This technique reveals thinner, more elongated quantum dots that often have a ring-like shape as shown in Figure 2.2. Typical dot dimensions are 100 nm base diameter and 1-2 nm thickness in growth direction. Due to their smaller thicknesses, these

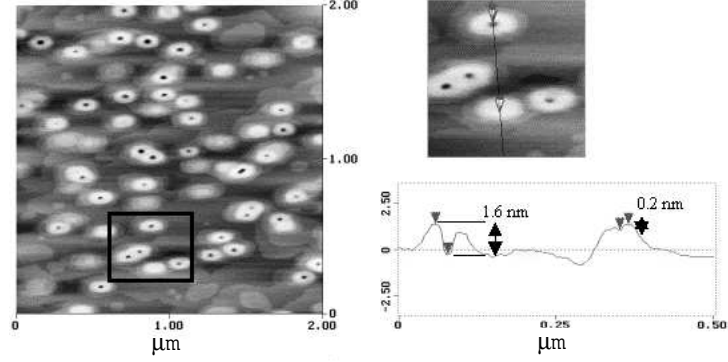


Figure 2.2: AFM picture of Quantum Dots

quantum dots emit at lower energies (1.25 - 1.3 eV) allowing the usage of Si based detectors. We note that the ring shape of our quantum dots does not effect our experiments as we do not apply magnetic fields [16]. The confinement energies for both electrons and holes in these quantum dots are larger than 50 meV. Energy separation between the ground and excited exciton (electron-hole) states typically exceeds 20 meV [17]. A random in plane distribution of islands is observed on the surface. The quantum dot density of our samples can be made constant at 10^{10} cm^{-2} or with a gradient in density from zero to 10^{10} cm^{-2} in the In flow direction. These two different density profiles can be achieved by rotating or not rotating the wafer during the MBE growth, respectively.

Layer structures of the samples investigated are shown in Figure 2.3. Both bulk and microdisk samples are based on an AlAs/GaAs short-period superlattice and a GaAs buffer layer for substrate smoothing. Quantum dots are embedded in the center of a 200 nm thick GaAs layer in both samples. In microdisk sample there is a 0.5 μm thick $\text{Al}_{0.65}\text{Ga}_{0.35}\text{As}$ post layer underneath the GaAs capping layer.

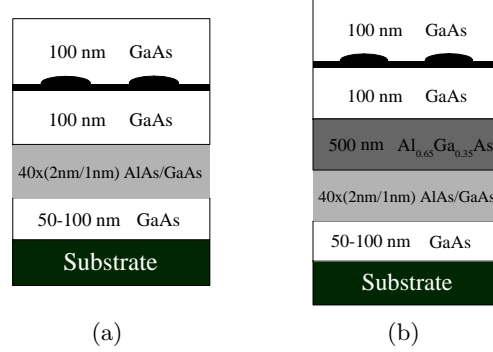


Figure 2.3: Layers of (a) bulk and (b) microdisk samples

2.2 Photoluminescence Characteristics

Photoluminescence measurements rely on laser excitation with a photon energy larger than that of quantum dot transitions, and detection of the fluorescence from various recombination channels. In addition to revealing emission energies of specific recombination channels of a single quantum dot, this experiment allows for the localization of the quantum dot within the optical resolution of the setup.

Our micro-photoluminescence setup is a low-temperature diffraction limited scanning optical microscope in which spectral detection is done by a spectrometer and a Charge Coupled Device (CCD) detector (Figure 2.4). The quantum dot samples are mounted in a He-flow cryostat (Oxford Ins., Microstat) allowing for temperature tuning from 4 - 300 K. The cryostat is moved by computer-controlled translation stages having a minimum step size of 10 nm (Melles-Griot, Nanomover), due to the vibrations induced from outside, our scanning resolution is ~ 100 nm. The sample is excited either with a continuous wave diode laser (operating at 785 nm), a continuous wave Ti:Sa laser (Spectra-Physics 3900S, operating at 760 nm), or a mode-locked Ti:Sa laser (Custom built system, 82 MHz, 250 fs, operating at 790 nm), generating electron-hole pairs in the GaAs barrier layer which are subsequently captured by the quantum dots within a short timescale (< 35 ps) [18]. Excitation and

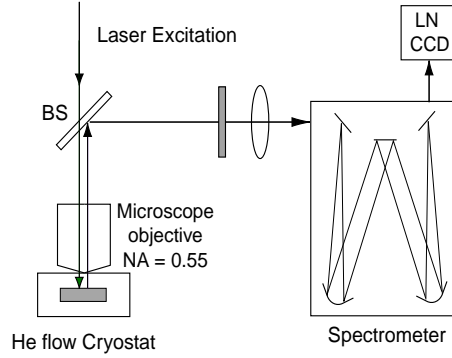


Figure 2.4: Photoluminescence setup

collection are done through the same microscope objective ($NA = 0.55$) in normal direction (diffraction limit: $1.7 \mu m$). After filtering the scattered laser light and the emission from the GaAs substrate and wetting layer, the collected luminescence is dispersed by a 50 cm spectrometer (Acton Research Spectrapro-500i, spectral resolution: $70 \mu eV$) and detected by a Si CCD (Princeton Instruments Spex X 400B Digital CCD) detector.

Figure 2.5(a) shows typical power dependent photoluminescence spectra from a single InAs quantum dot located in a bulk sample under continuous wave excitation taken at 4 K. The sharp peaks observed in that figure are indications of the three dimensional carrier confinement [10, 11, 12] created by the bandgap difference between the InAs quantum dot and the surrounding GaAs (Figure 2.5(b)). At low pump powers, the single exciton emission dominates the spectrum, whereas at higher pump powers, biexciton emission from the s-shell together with p-shell and higher excited state emissions become dominant. Single exciton emission corresponds to the recombination of an exciton in the ground state of the quantum dot in the absence of another exciton; while biexciton emission is the recombination of a ground-state exciton in the presence of another one. Due to carrier-carrier interactions, the biexciton emission has an energy shift from the single exciton emission. In our

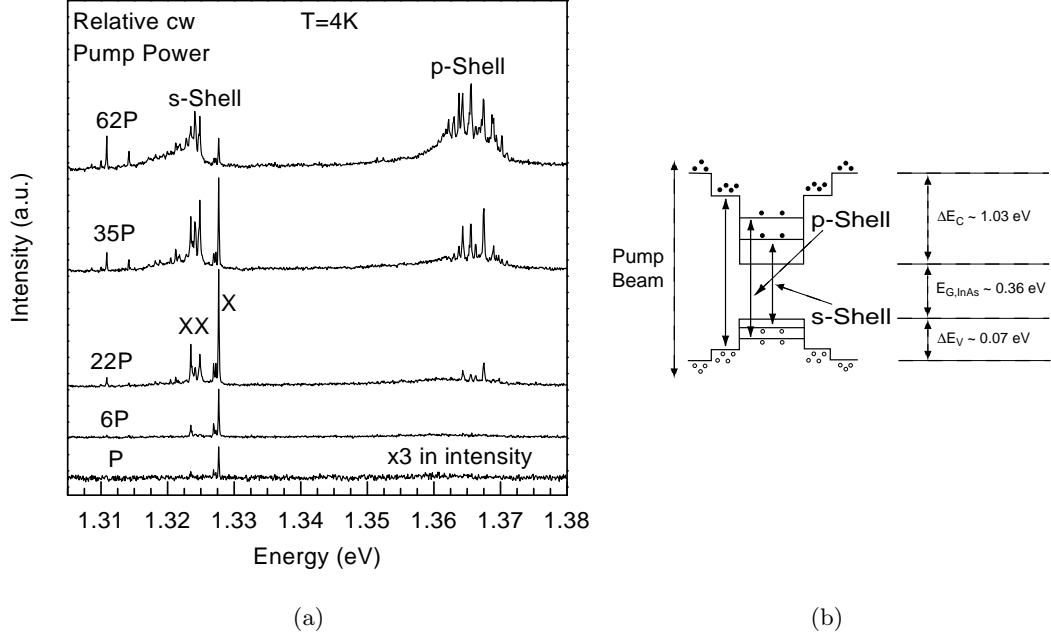


Figure 2.5: (a) PL spectra of a quantum dot for various powers of the continuous wave Ti:Sa laser at 760 nm . Single exciton transition, biexciton transition, s-Shell transitions, and p-Shell transitions are visible. (b) Fundamental single quantum dot transitions, marked band offsets are for room temperature (the drawing is not to scale) .

samples this energy shift is $\sim 3.5\text{ meV}$ on the lower energy (red) side. This is an extremely crucial property that is key for all the results achieved in following chapters. This inherent *anharmonicity* in the excitonic energy levels allows for the separate investigation of the single exciton and biexciton emissions by proper spectral filtering. Another signature of biexciton emission is the quadratic dependence of its intensity to pump power (Figure 2.5(a)).

The spectrum of a single quantum dot is in general extremely rich as depicted in Figure 2.5(a). This richness arises primarily from the fact that the confinement length-scale is much larger than the lattice spacing, giving rise to multi-

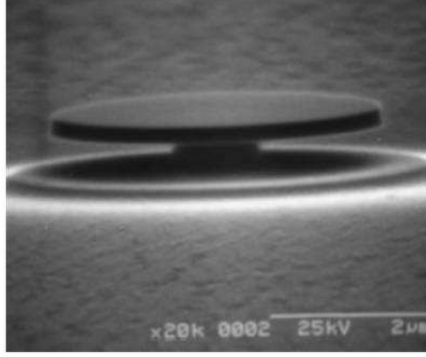


Figure 2.6: The microdisk structure that consists of a $5\ \mu\text{m}$ diameter disk and a $0.5\ \mu\text{m}$ post. The GaAs disk area is $200\ \text{nm}$ thick and contains InAs quantum dots.

electron-hole excitations that differ in energy from the fundamental one by only a few meV. In Figure 2.5(a) charged exciton lines with small red or blue detuned emission energies are also seen together with the single-exciton, biexciton, and p-shell emissions. These several emission channels will be discussed in Chapter 6. At low excitation powers all the emission lines in Figure 2.5(a) are narrow while they broaden at higher excitation due to the interaction with free-carriers.

2.3 Microdisk Processing

Microdisk structures are processed using a two-step etching technique [19, 20]. We used photolithography in defining circles with diameters ranging from 1.5 to $6\ \mu\text{m}$. Cylindrical microdisk layers are then etched using a HBr-based wet etchant. Etched regions are masked by either $1\ \mu\text{m}$ thick photoresist or $50\ \text{nm}$ thick Ti. The HBr-based etch solution produces isotropic etching, with the disk diameter reduced (lateral etching) during the vertical etch into the material. The etchant is also optimized to reveal minimal surface roughness at the end of vertical etching. After delineation of the microdisk feature, the pedestal layer is defined by etching in a dilute HF solution, which has a high selectivity in etching AlGaAs with high Al

content in preference to GaAs. Scanning electron micrographs reveal the top disk layer to have a smooth, nonfaceted surface with an almost vertical etched profile (Figure 2.6). Since the Q-values of microdisk whispering modes are limited by surface roughness, minimum surface roughness is a very stringent requirement for cavity-QED experiments (Chapter 5).

Chapter 3

Photon Antibunching

Under continuous wave excitation, a two-level emitter emits photons one-by-one. After a photon is emitted, the system is necessarily in the radiatively inactive ground state and a second photon cannot be emitted immediately after the first one. The emission probability *recovers* its mean value only after the excited-state occupancy reaches the steady-state population, determined by the excitation and relaxation rates. Hence photons emitted from a single two-level emitter are *anti-bunched*, this is the essence of the photon antibunching phenomenon. As we discuss in this chapter, this phenomenon requires a quantum mechanical analysis, it cannot be explained by classical wave description of light.

The first prediction of this phenomenon dates to 1976 [21] with the first experimental demonstration in 1977 [1] using single Na atoms. Since then, photon antibunching has been observed in various different systems: a single stored Mg^+ ion (1987 [3]), a single *pentacene* molecule (1992 [22]), a single *terrylene* molecule (2000 [23]), a single chemically synthesized CdSe quantum dot (2000 [5]), a single nitrogen-vacancy center in diamond (2000 [24, 25]). The underlying two-level structure of single InAs quantum dots also gives rise to photon antibunching (2000 [26, 6], 2001 [27]) as presented in this chapter.

In this chapter we first introduce the second order photon correlation func-

tion. Thereafter we analyze the photon antibunching phenomenon by solving the second order photon correlation function for both an ideal two-level system and a single quantum dot, and then we present our experimental results.

3.1 Degree of Second Order Coherence

Coherence properties of a light source can be fully analyzed by measuring all of its coherence functions. The general n^{th} degree coherence function is given as [28]:

$$g^{(n)}(\mathbf{r}_1 t_1, \dots, \mathbf{r}_n t_n; \mathbf{r}_{n+1} t_{n+1}, \dots, \mathbf{r}_{2n} t_{2n}) = \frac{\langle \hat{E}^-(\mathbf{r}_1 t_1) \dots \hat{E}^-(\mathbf{r}_n t_n) \hat{E}^+(\mathbf{r}_{2n} t_{2n}) \dots \hat{E}^+(\mathbf{r}_{n+1} t_{n+1}) \rangle}{\langle \hat{E}^{(-)}(\mathbf{r}_1 t_1) \hat{E}^{(+)}(\mathbf{r}_1 t_1) \rangle \dots \langle \hat{E}^{(-)}(\mathbf{r}_{2n} t_{2n}) \hat{E}^{(+)}(\mathbf{r}_{2n} t_{2n}) \rangle^{1/2}} \quad (3.1.1)$$

where we use the quantized electromagnetic field defined as [29]:

$$\begin{aligned} \hat{\mathbf{E}}(\mathbf{r}, t) &= \int \hat{\mathbf{E}}_{\mathbf{k}}(\mathbf{r}, t) d\mathbf{k}, \\ \hat{\mathbf{E}}_{\mathbf{k}}(\mathbf{r}, t) &= \hat{\mathbf{E}}_{\mathbf{k}}^+(\mathbf{r}, t) + \hat{\mathbf{E}}_{\mathbf{k}}^-(\mathbf{r}, t) = i\sqrt{\frac{\hbar\omega_{\mathbf{k}}}{2\epsilon_0 V}} \epsilon_{\mathbf{k}} \left(\hat{a}_{\mathbf{k}} e^{-i\omega_{\mathbf{k}} t + i\mathbf{k} \cdot \mathbf{r}} - \hat{a}_{\mathbf{k}}^\dagger e^{i\omega_{\mathbf{k}} t - i\mathbf{k} \cdot \mathbf{r}} \right) \end{aligned} \quad (3.1.2)$$

$\epsilon_{\mathbf{k}}$, $\hat{a}_{\mathbf{k}}$, and $\hat{a}_{\mathbf{k}}^\dagger$ denote the field polarization vector, single mode photon annihilation, and creation operators respectively. Among the coherence functions in Equation 3.1.1, the *first* and *second* orders are commonly measured in laboratory. "Young's Double Slit Experiment" and "Hanbury Brown and Twiss Experiment" are the most characteristic experiments in determining the first and second order coherence functions respectively.

Assuming no dependence on \mathbf{r}_n , the first order coherence function, which measures the correlations of the field amplitude, can be written as:

$$g^{(1)}(\tau) = \frac{\langle \hat{E}^-(t + \tau) \hat{E}^+(t) \rangle}{\langle \hat{E}^{(-)}(t) \hat{E}^{(+)}(t) \rangle} \quad (3.1.3)$$

which reduces to:

$$g^{(1)}(\tau) = \frac{\langle \hat{a}_{\mathbf{k}}^\dagger(t + \tau) \hat{a}_{\mathbf{k}}(t) \rangle}{\langle \hat{a}_{\mathbf{k}}^\dagger(t) \hat{a}_{\mathbf{k}}(t) \rangle} \quad (3.1.4)$$

for a single mode field. $\hat{a}_{\mathbf{k}}(t) = e^{-i\omega_{\mathbf{k}}t}\hat{a}_{\mathbf{k}}$, and $\hat{a}_{\mathbf{k}}^\dagger(t) = e^{i\omega_{\mathbf{k}}t}\hat{a}_{\mathbf{k}}^\dagger$ are single mode photon annihilation and creation operators in the Heisenberg picture. We will not analyze the general properties of $g^{(1)}(\tau)$ for different light sources, such an analysis can be found in Ref. [28]. However it is important to note that various different light sources can reveal the same first order coherence function. Moreover, nonclassical nature of different light sources is also non-visible in the first order coherence function for most cases. For instance a classical single-mode light source (single mode thermal state, or a coherent state), and a single photon Fock state both have their first order coherence functions equal to $e^{i\omega\tau}$.

Differences between classical and nonclassical light sources are most conveniently revealed by the second order coherence function measurements. Considering the quantized electromagnetic field, and assuming no dependence on \mathbf{r}_n , the second order coherence function is:

$$\begin{aligned} g^{(2)}(\tau) &= \frac{\langle E^-(t)E^-(t+\tau)E^+(t+\tau)E^+(t) \rangle}{\langle E^-(t)E^+(t) \rangle^2} \\ &= \frac{\langle : \hat{I}(t+\tau)\hat{I}(t) : \rangle}{\langle \hat{I}(t) \rangle^2} \end{aligned} \quad (3.1.5)$$

:: denotes the normal ordering of the field amplitudes. For a single mode field Equation 3.1.5 can be further simplified to:

$$g^{(2)}(\tau) = \frac{\langle \hat{a}_{\mathbf{k}}^\dagger(t)\hat{a}_{\mathbf{k}}^\dagger(t+\tau)\hat{a}_{\mathbf{k}}(t+\tau)\hat{a}_{\mathbf{k}}(t) \rangle}{\langle \hat{a}_{\mathbf{k}}^\dagger(t)\hat{a}_{\mathbf{k}}(t) \rangle^2} \quad (3.1.6)$$

For a classical electromagnetic field:

$$\mathbf{E}(\mathbf{r}, t) = \int \mathbf{E}_{\mathbf{k}}(\mathbf{r}, t) d\mathbf{k}, \quad \mathbf{E}_{\mathbf{k}}(\mathbf{r}, t) = \mathbf{E}_{\mathbf{k}}^* e^{-i\omega_{\mathbf{k}}t + i\mathbf{k} \cdot \mathbf{r}} + \mathbf{E}_{\mathbf{k}} e^{i\omega_{\mathbf{k}}t - i\mathbf{k} \cdot \mathbf{r}} \quad (3.1.7)$$

The fluctuations in the field intensity are given by the following distribution function:

$$\begin{aligned} g_{classical}^{(2)}(\tau) &= \frac{\langle E(t)E(t+\tau)E^*(t+\tau)E^*(t) \rangle}{\langle E(t)E^*(t) \rangle^2} \\ &= \frac{\langle I(t+\tau)I(t) \rangle}{\langle I(t) \rangle^2} \end{aligned} \quad (3.1.8)$$

$I(t)$ corresponds to the average field intensity measured at time t . Classical second order coherence function ($g_{classical}^{(2)}(\tau)$) can be different from the quantum mechanical second order coherence function ($g^{(2)}(\tau)$) since $\langle : \hat{I}(t + \tau) \hat{I}(t) : \rangle$ is not necessarily equal to $\langle I(t + \tau) I(t) \rangle$ for all light sources.

Some observations can be made on the value of $g_{classical}^{(2)}(\tau)$. For $\tau = 0$:

$$g_{classical}^{(2)}(0) = \frac{\langle I(t)^2 \rangle}{\langle I(t) \rangle^2} \quad (3.1.9)$$

Considering the random process $I(t)$, if we assume that different intensity measurements at different times are independent from each other, and identical to each other, Cauchy's inequality:

$$2I(t_1)I(t_2) \leq I(t_1)^2 + I(t_2)^2 \quad (3.1.10)$$

can be used to derive the inequality [28]:

$$\left(\frac{I(t_1) + I(t_2) + \dots + I(t_N)}{N} \right)^2 \leq \frac{I(t_1)^2 + I(t_2)^2 + \dots + I(t_N)^2}{N} \quad (3.1.11)$$

Using ergodicity due to the independence of $I(t_i)$:

$$\langle I(t) \rangle = \frac{I(t_1) + I(t_2) + \dots + I(t_N)}{N} \quad (3.1.12)$$

$$\langle I(t)^2 \rangle = \frac{I(t_1)^2 + I(t_2)^2 + \dots + I(t_N)^2}{N} \quad (3.1.13)$$

Equations 3.1.11, 3.1.12, and 3.1.13 reveal:

$$\langle I(t) \rangle^2 \leq \langle I(t)^2 \rangle \Rightarrow g_{classical}^{(2)}(0) \geq 1 \quad (3.1.14)$$

Hence, classical second order coherence function at zero time delay can have the values in the range:

$$1 \leq g_{classical}^{(2)}(0) < \infty \quad (3.1.15)$$

Another important inequality can also be derived for $g_{classical}^{(2)}(\tau)$ at a general delay time τ . Again starting from Cauchy's inequality in Equation 3.1.10, the following inequality can be derived:

$$\begin{aligned} & (I(t_1)I(t_1 + \tau) + \dots + I(t_N)I(t_N + \tau))^2 \\ & \leq (I(t_1)^2 + \dots + I(t_N)^2) (I(t_1 + \tau)^2 + \dots + I(t_N + \tau)^2) \end{aligned} \quad (3.1.16)$$

Using the ergodicity property, and independent identical random processes, Equation 3.1.16 reduces to:

$$\langle I(t)I(t + \tau) \rangle \leq \langle I(t)I(t)^2 \rangle \Rightarrow g^{(2)}(\tau) \leq g^{(2)}(0) \quad (3.1.17)$$

From Equations 3.1.15, and 3.1.17 we can deduce the range for $g^{(2)}(\tau)$ as:

$$1 \leq g_{classical}^{(2)}(\tau) < \infty \quad (3.1.18)$$

Now we would like to analyze the second order coherence functions of a coherent state, and an n-photon Fock state, to highlight the main points relevant for our work.

Coherent state: Coherent state is defined as the eigenfunction of the photon annihilation operator:

$$\hat{a}_{\mathbf{k}}|\alpha_{\mathbf{k}}\rangle = \alpha_{\mathbf{k}}|\alpha_{\mathbf{k}}\rangle$$

$$g^{(2)}(\tau) = \frac{\langle \alpha_{\mathbf{k}} | \hat{a}_{\mathbf{k}}^\dagger(t) \hat{a}_{\mathbf{k}}^\dagger(t + \tau) \hat{a}_{\mathbf{k}}(t + \tau) \hat{a}_{\mathbf{k}}(t) | \alpha_{\mathbf{k}} \rangle}{\langle \alpha_{\mathbf{k}} | \hat{a}_{\mathbf{k}}^\dagger(t) \hat{a}_{\mathbf{k}}(t) | \alpha_{\mathbf{k}} \rangle^2} = \frac{|\alpha|^4}{|\alpha|^4} = 1$$

This result can also be also obtained by taking the coherent state as a classical single mode electric field state defined in Equation 3.1.7, and calculating the second order coherence function using Equation 3.1.8.

n photon Fock state: For an n photon Fock state Equation 3.1.6 can be used to obtain:

$$\begin{aligned} g^{(2)}(\tau) &= \frac{\langle n_{\mathbf{k}} | \hat{a}_{\mathbf{k}}^\dagger(t) \hat{a}_{\mathbf{k}}^\dagger(t + \tau) \hat{a}_{\mathbf{k}}(t + \tau) \hat{a}_{\mathbf{k}}(t) | n_{\mathbf{k}} \rangle}{\langle n_{\mathbf{k}} | \hat{a}_{\mathbf{k}}^\dagger(t) \hat{a}_{\mathbf{k}}(t) | n_{\mathbf{k}} \rangle^2} \\ &= \begin{cases} \frac{n-1}{n} & ; n > 0 \\ 0 & ; n = 0 \end{cases} \end{aligned} \quad (3.1.19)$$

Equation 3.1.19 implies $g^{(2)}(\tau) < 1$ for all Fock states. This result which is due to the nonclassical nature of the photon number states is contradictory with the range given in Equation 3.1.18 for a classical light source. Hence $g^{(2)}(0) < 1$ is a clear indication of nonclassical light emission. This is indeed the definition of the photon antibunching phenomenon:

$$0 \leq g^{(2)}(0) < 1 \quad (3.1.20)$$

defines a photon antibunched light source in general. As seen in the Equation 3.1.19, among the n photon Fock states, the single photon Fock state has the strongest nonclassicality as $g^{(2)}(\tau) = 0$ for that state.

At this stage it is also relevant to analyze the photon antibunching from multi identical single photon Fock state emitters. As it was calculated in Equation 3.1.19, for an ideal single photon Fock state generator; $g^{(2)}(0) = 0$. Consider N identical independent such sources whose second order coherence function is $g^{(2)}(\tau)$. The second order coherence function for the collective emission can then be calculated by substituting the intensity operator below into Equation 3.1.5:

$$\hat{I}(t) = \hat{I}_1(t) + \dots + \hat{I}_N(t)$$

revealing the following equation:

$$\begin{aligned} g_N^{(2)}(\tau) &= \frac{Ng^{(2)}(\tau) + \{\langle (I_1(t+\tau) + \dots + I_N(t+\tau)) \rangle^2 - \{\langle I_1(t) \rangle^2 + \dots + \langle I_N(t) \rangle^2\}\}}{\langle (I_1(t+\tau) + \dots + I_N(t+\tau)) \rangle^2} \\ &= 1 + (g^{(2)}(\tau) - 1) \frac{\langle I_1(t) \rangle^2 + \dots + \langle I_N(t) \rangle^2}{\langle (I_1(t+\tau) + \dots + I_N(t+\tau)) \rangle^2} \\ &= \frac{N - 1 + g^{(2)}(\tau)}{N} \end{aligned} \quad (3.1.21)$$

Hence for N ideal single photon Fock state generators:

$$g_N^{(0)}(\tau) = 1 - \frac{1}{N} \quad (3.1.22)$$

This equality has a rather important practical significance: It allows the usage of photon antibunching experiments to identify single two-level emitters. If the emission

is not due to a single emitter, $g_N^{(2)}(0) > 0.5$. Hence, $g_N^{(2)}(0) = 0.5$ can be regarded as an experimental boundary to separate a single two-level emitter from multiple ones.

3.2 Photon Antibunching in Resonance Fluorescence of a Two-Level System

In this section we analyze photon antibunching in the emission of a single two-level emitter. This analysis is in direct relevance to the case of single quantum dots as we will see in the next sections. We will hereafter call the second order coherence function as the second order photon correlation function in the text.

In experimental terms, the second order photon correlation function ($g^{(2)}(\tau)$) corresponds to the relative detection probability of a photon at time τ given that another photon detection has occurred at time 0. Its expression in terms of the field components is given in Equation 3.1.5 and repeated below for convenience:

$$g^{(2)}(\tau) = \frac{\langle E^{(-)}(t)E^{(-)}(t+\tau)E^{(+)}(t+\tau)E^{(+)}(t) \rangle}{\langle E^{(-)}(t)E^{(+)}(t) \rangle^2} \quad (3.2.1)$$

For a two-level emitter, the field components can be expressed in terms of the two-level emitter operators, assuming the far-field, this source-field expression [28] is given as:

$$\hat{\mathbf{E}}^{(+)}(\mathbf{r}t) = -\frac{e\omega_0^2|\mu_{eg}|\sin\alpha}{4\pi\epsilon_0c^2|\mathbf{r}|}\mathbf{i}\hat{\sigma}_{ge}(t - \frac{|\mathbf{r}|}{c}) \quad (3.2.2)$$

where $\hat{\sigma}_{ge} = |g\rangle\langle e|$ and $\hat{\sigma}_{eg} = |e\rangle\langle g|$ are the two-level emitter projection operators, and μ_{eg} , α , and \mathbf{i} , are the dipole matrix element, angle between the vectors $\mu_{eg}-\mathbf{r}$, and unit vector in transverse direction, respectively. Using Equation 3.2.2, Equation 3.2.1 can be expressed in terms of the atomic operators as:

$$g^{(2)}(\tau) = \frac{\langle \hat{\sigma}_{eg}(t)\hat{\sigma}_{eg}(t+\tau)\hat{\sigma}_{ge}(t+\tau)\hat{\sigma}_{ge}(t) \rangle}{\langle \hat{\sigma}_{eg}(t)\hat{\sigma}_{ge}(t) \rangle^2} = \frac{\langle \hat{\sigma}_{eg}(t)\hat{\sigma}_{ee}(t+\tau)\hat{\sigma}_{ge}(t) \rangle}{\langle \hat{\sigma}_{ee}(t) \rangle^2} \quad (3.2.3)$$

Appendix A contains the detailed study of the second order photon correlation function for a general two-level emitter depicted in Figure 3.1, under continuous

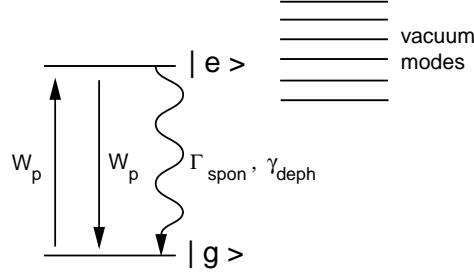


Figure 3.1: Laser driven two-level emitter

wave resonant excitation conditions, considering spontaneous emission and other coherence dephasing mechanisms. In this section however, a two-level emitter that has fast coherence dephasing mechanisms (strongly damped coherences) is analyzed only, as it is relevant to single quantum dots under nonresonant excitation conditions (Chapter 7).

Assuming strongly damped coherences, the two-level emitter in Figure 3.1 can be analyzed in the rate equation limit:

$$\frac{d}{dt} \begin{bmatrix} \langle \hat{\sigma}_{ee}(t) \rangle \\ \langle \hat{\sigma}_{gg}(t) \rangle \end{bmatrix} = \begin{bmatrix} -\Gamma_{\text{spont}} - W_p & W_p \\ \Gamma_{\text{spont}} + W_p & -W_p \end{bmatrix} \begin{bmatrix} \langle \hat{\sigma}_{ee}(t) \rangle \\ \langle \hat{\sigma}_{gg}(t) \rangle \end{bmatrix} \quad (3.2.4)$$

Using Equation 3.2.4 and quantum regression theorem (Appendix A), the unnormalized second order correlation function $G^{(2)}(\tau) = \langle \hat{\sigma}_{eg}(t') \hat{\sigma}_{ee}(t' + \tau) \hat{\sigma}_{ge}(t') \rangle = G_{ee}(\tau)$ can be found by the solution of the following set of differential equations and initial conditions:

$$\frac{d}{d\tau} \begin{bmatrix} G_{ee}^{(2)}(\tau) \\ G_{gg}^{(2)}(\tau) \end{bmatrix} = \begin{bmatrix} -\Gamma_{\text{spont}} - W_p & W_p \\ \Gamma_{\text{spont}} + W_p & -W_p \end{bmatrix} \begin{bmatrix} G_{ee}^{(2)}(\tau) \\ G_{gg}^{(2)}(\tau) \end{bmatrix} \quad (3.2.5)$$

$$G_{ee}^{(2)}(\tau = 0) = 0$$

$$G_{gg}^{(2)}(\tau = 0) = \langle \hat{\sigma}_{ee}(t') \rangle$$

satisfying the closed system relationship:

$$\langle \hat{\sigma}_{ee}(t) \rangle + \langle \hat{\sigma}_{gg}(t) \rangle = 1 \Rightarrow G_{ee}^{(2)}(\tau) + G_{gg}^{(2)}(\tau) = \langle \hat{\sigma}_{ee}(t') \rangle.$$

In the above set of equations, substituting $\langle \hat{\sigma}_{ee}(t') \rangle$ by its steady-state value $\frac{W_p/2}{\Gamma_{spon} + W_p}$, an analytical solution for the normalized second order correlation function can be obtained:

$$g^{(2)}(\tau) = 1 - e^{-(\Gamma_{spon} + W_p)\tau} \quad (3.2.6)$$

Equation 3.2.6 at two pump powers is depicted in Figure 3.2. In that figure, the principal signature of photon antibunching is the dip at $\tau = 0$, which corresponds to vanishing probability of simultaneous emission of more than one photons from the two-level emitter. The effect of spontaneous emission and pumping rate causes the second order photon correlation function to reach the value 1 for large τ . The transition time from $g^{(2)} = 0$ to $g^{(2)} = 1$ is given by $1/(\Gamma + W_p)$ which is the recovery time of the excited state population of the two-level emitter (Appendix A). The level $g^{(2)} = 1$ corresponds to Poissonian photon statistics indicating that photons emitted by a time separation much larger than $1/(\Gamma + W_p)$ are independent from each other.

3.3 Modelling a Single Quantum Dot as a Three-Level System

Resonance fluorescence analyzed in the previous section is experimentally achievable using atoms [1]. The gaseous state of atoms hardly causes any stray light due to the laser. Hence it is possible to separate the atomic fluorescence from the excitation laser beam simply by properly locating the detector. However in the resonance fluorescence experiments using quantum dots, the solid nature of the samples cause a large amount of stray laser light, making separate detection of quantum dot fluorescence very hard. To solve this problem, it is possible to pump the quantum

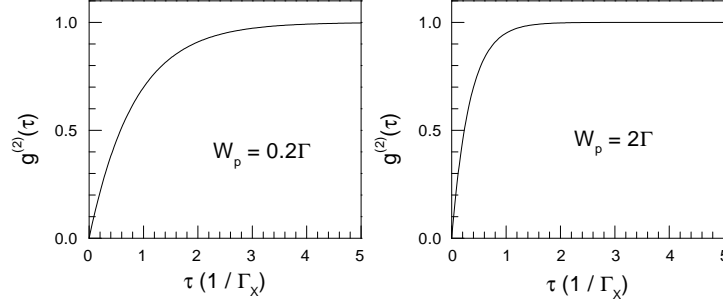


Figure 3.2: Photon antibunching in resonance fluorescence of a strongly damped two-level emitter

dot indirectly through fast relaxing upper energy levels. For non-resonant pumping, these higher energy states are the wetting layer or substrate energy levels that are known to have fast relaxation times (< 35 ps, [18]). As we demonstrate in this section, provided that the relaxation rates of these states are much larger than the other rates (pumping rates, other relaxation rates) in the consideration, these states can be ignored for the purposes of the rate equation analysis.

As it was demonstrated in Figure 2.5(a), under nonresonant excitation conditions the number of excitons in our single InAs quantum dots increase in a ladder structure, first s-shell is filled then p-shell etc... Hence, for low excitation experiments, consideration of only s-shell is enough for modelling a single quantum dot. This was the case for all of our experiments. Under these low excitation conditions, a level diagram as in Figure 3.3(a) can be drawn for a single quantum dot. In Figure 3.3(a) levels $|0\rangle$, $|X\rangle$, and $|XX\rangle$ correspond to zero, single, and two excitonic energy levels, while $|1\rangle$, and $|2\rangle$ correspond to fast relaxing pumping levels that pump levels $|X\rangle$, and $|XX\rangle$ respectively. We have placed a stimulated emission term between levels $|1\rangle$, and $|0\rangle$ for completeness. As it will be seen in the following analysis this term does not have a significance under the assumption $\Gamma_{pX} \gg W_{pX}$. There is no stimulated emission term between levels $|2\rangle$, and $|X\rangle$ as there is not a second

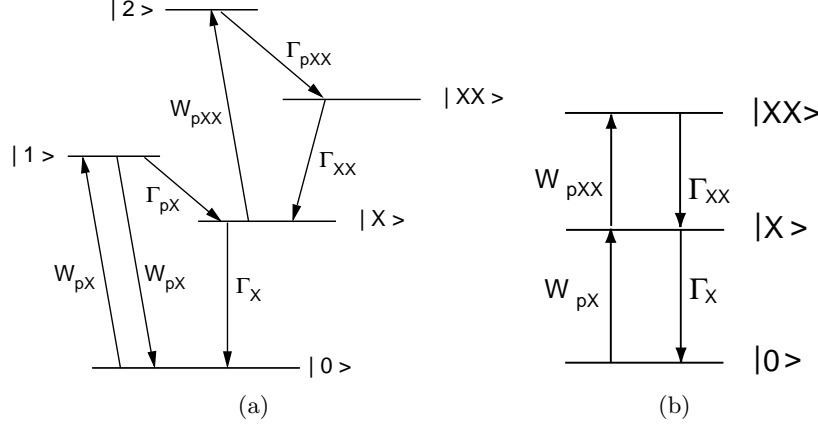


Figure 3.3: (a) A realistic rate equation model of a single quantum dot under low nonresonant excitation conditions. (b) Reduced equivalent three-level model.

laser field that is actually causing the pumping from level $|X\rangle$ to $|2\rangle$. We also did not include the spontaneous recombination between levels $|1\rangle$ and $|0\rangle$ assuming that this a slower process than Γ_{pX} . Using the pumping rates shown in the figure, the following rate equations can be written for levels $|1\rangle$, and $|2\rangle$:

$$\begin{aligned} \frac{d\langle\hat{\sigma}_2(t)\rangle}{dt} &= W_{pXX}\langle\hat{\sigma}_X(t)\rangle - \Gamma_{pXX}\langle\hat{\sigma}_2(t)\rangle \\ \frac{d\langle\hat{\sigma}_1(t)\rangle}{dt} &= W_{pX}\langle\hat{\sigma}_0(t)\rangle - (W_{pX} + \Gamma_{pX})\langle\hat{\sigma}_1(t)\rangle \end{aligned} \quad (3.3.1)$$

Under the fast relaxation condition:

$$\{\Gamma_{pX}, \Gamma_{pXX}\} \gg \{W_{pX}, W_{pXX}, \Gamma_X, \Gamma_{XX}\} \quad (3.3.2)$$

levels $|1\rangle$, and $|2\rangle$ reach their steady-states much faster than the other levels, hence $\langle\hat{\sigma}_1\rangle$, and $\langle\hat{\sigma}_2\rangle$ can be replaced by their steady state values in the time scales relevant to $\langle\hat{\sigma}_0\rangle$, $\langle\hat{\sigma}_X\rangle$, and $\langle\hat{\sigma}_{XX}\rangle$:

$$\begin{aligned} \frac{d\langle\hat{\sigma}_2(t)\rangle}{dt} \approx 0 &\Rightarrow \langle\hat{\sigma}_2(t)\rangle \approx \langle\hat{\sigma}_{2s,s}\rangle = \frac{W_{pXX}}{\Gamma_{pXX}}\langle\hat{\sigma}_X(t)\rangle \\ \frac{d\langle\hat{\sigma}_1(t)\rangle}{dt} \approx 0 &\Rightarrow \langle\hat{\sigma}_1(t)\rangle \approx \langle\hat{\sigma}_{1s,s}\rangle = \frac{W_{pX}}{W_{pX} + \Gamma_{pX}}\langle\hat{\sigma}_0(t)\rangle \end{aligned}$$

Revealing the following rate equations for levels $|0\rangle$, $|X\rangle$, and $|XX\rangle$:

$$\frac{d}{dt} \begin{bmatrix} \langle \hat{\sigma}_{XX}(t) \rangle \\ \langle \hat{\sigma}_X(t) \rangle \\ \langle \hat{\sigma}_0(t) \rangle \end{bmatrix} = \begin{bmatrix} -\Gamma_{XX} & W_{pXX} & 0 \\ \Gamma_{XX} & -(\Gamma_X + W_{pXX}) & \frac{W_{pX}\Gamma_{pX}}{W_{pX} + \Gamma_{pX}} \\ 0 & \Gamma_X & -W_{pX} \left(1 - \frac{W_{pX}}{W_{pX} + \Gamma_{pX}}\right) \end{bmatrix} \begin{bmatrix} \langle \hat{\sigma}_{XX}(t) \rangle \\ \langle \hat{\sigma}_X(t) \rangle \\ \langle \hat{\sigma}_0(t) \rangle \end{bmatrix}$$

Using the assumption in 3.3.2, the above set of equations reduces to:

$$\frac{d}{dt} \begin{bmatrix} \langle \hat{\sigma}_{XX}(t) \rangle \\ \langle \hat{\sigma}_X(t) \rangle \\ \langle \hat{\sigma}_0(t) \rangle \end{bmatrix} = \begin{bmatrix} -\Gamma_{XX} & W_{pXX} & 0 \\ \Gamma_{XX} & -(\Gamma_X + W_{pXX}) & W_{pX} \\ 0 & \Gamma_X & -W_{pX} \end{bmatrix} \begin{bmatrix} \langle \hat{\sigma}_{XX}(t) \rangle \\ \langle \hat{\sigma}_X(t) \rangle \\ \langle \hat{\sigma}_0(t) \rangle \end{bmatrix} \quad (3.3.3)$$

Note that Equation 3.3.3 is the rate equation describing the system depicted in Figure 3.3(b). Hence, under low nonresonant excitation conditions, in the rate equation limit where all lines are assumed to be highly dephased, the fast relaxing pumping levels can be ignored, and the quantum dot can be modelled as a three-level system.

3.4 Analysis of Photon Antibunching in a Single Quantum Dot

In this section quantum dot antibunching properties are investigated using the three-level model (Figure 3.3(b)) in the rate equation limit. As it was explained in the previous sections the reason to use this model for a single quantum dot is three-fold: (i) firstly, all of our experiments are done in the low pumping regime where average number of excitons in the quantum dot is less than two, (ii) secondly, the nonresonantly excited states used in our experiments (wetting layer states, and GaAs substrate states) have large relaxation rates (< 35 ps, [18]) enabling us to ignore the effect of these higher energy levels in the analysis, and (iii) thirdly, as it will be shown in Chapter 7, under nonresonant excitation conditions, dephasing processes in a quantum dot are much faster than the relevant excitation Rabi frequencies validating the rate equation treatment. Under these assumptions, following the steps in Section 3.2, starting from the three-level rate equations, and using the quantum regression theorem, the following equations are obtained for two-time correlation

functions:

$$\frac{d}{d\tau} \begin{bmatrix} G_{XX,XX}^{(2)}(\tau) \\ G_{X,X}^{(2)}(\tau) \\ G_{0,0}^{(2)}(\tau) \end{bmatrix} = \begin{bmatrix} 0 & W_{pXX} & -\Gamma_{XX} \\ W_{pX} & -(W_{pXX} + \Gamma_X) & \Gamma_{XX} \\ -W_{pX} & \Gamma_X & 0 \end{bmatrix} \begin{bmatrix} G_{XX,XX}^{(2)}(\tau) \\ G_{X,X}^{(2)}(\tau) \\ G_{0,0}^{(2)}(\tau) \end{bmatrix} \quad (3.4.1)$$

for the initial conditions:

$$\begin{aligned} G_{XX}^{(2)}(\tau = 0) &= 0 \\ G_X^{(2)}(\tau = 0) &= 0 \\ G_0^{(2)}(\tau = 0) &= \langle \hat{\sigma}_{X,X}(t') \rangle \end{aligned}$$

where

$$\begin{aligned} G_{0,0}^{(2)}(\tau) &= \langle \hat{\sigma}_{X,0}(t') \hat{\sigma}_{0,0}(t' + \tau) \hat{\sigma}_{0,X}(t') \rangle \\ G_{X,X}^{(2)}(\tau) &= \langle \hat{\sigma}_{X,0}(t') \hat{\sigma}_{X,X}(t' + \tau) \hat{\sigma}_{0,X}(t') \rangle \\ G_{XX,XX}^{(2)}(\tau) &= \langle \hat{\sigma}_{X,0}(t') \hat{\sigma}_{XX,XX}(t' + \tau) \hat{\sigma}_{0,X}(t') \rangle \end{aligned}$$

$G_{X,X}^{(2)}(\tau)$ corresponds to the unnormalized second order photon correlation function $G^{(2)}(\tau)$.

Exemplary solutions of $G_{X,X}^{(2)}(\tau)$ for four different pumping intensities are shown in Figure 3.4. In these calculations $\Gamma_{XX} = 2\Gamma_X$, and $W_{pXX} = 2W_{pX}$ are assumed. These are approximately relevant ratios as it becomes clear later in this chapter, and Chapter 6. There are several points to note in Figure 3.4. The decay time observed in $g^{(2)}(\tau)$ is in general determined by W_{pX} , W_{pXX} , Γ_X , and Γ_{XX} in a nontrivial manner preserving a tendency similar to a two-level system at low-excitation regime. Hence, in low-excitation regime ($\{W_{pX}, W_{pXX}\} \ll \{\Gamma_X, \Gamma_{XX}\}$) the decay time is approximately equal to the spontaneous emission time ($1/\Gamma_X$), while at higher excitation powers when the two-excitonic level is still not populated, it is determined by $1/(\Gamma_X + W_{pX})$.

At high excitation regime, the second order photon correlation function starts showing a bump near $\tau = 0$ ($W_p = 3\Gamma_X$ in Figure 3.4). This is a behavior

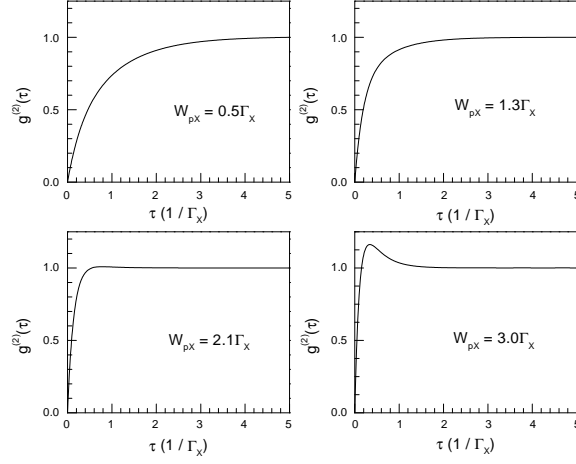


Figure 3.4: Calculated $g^{(2)}(\tau)$ for the three-level model at different pump powers, assuming $\Gamma_{XX} = 2\Gamma_X$, and $W_{pXX} = 2W_{pX}$.

special to a three-level system that does not apply to a two-level system [30]. When the system is highly excited, the average probability of photon emission from the single excitonic to ground state is very low, photon emission events are mostly occurring between the two excitonic and single excitonic states. Whereas at $\tau = 0$, in the second order correlation function, it is known that the system is in the ground state. During the recovery process, first the single excitonic state is filled making the photon emission probability between the single excitonic and ground states higher than its steady state value, causing the bump in $g^{(2)}(\tau)$.

3.5 Experiments

3.5.1 Hanbury Brown and Twiss Setup

Measurement of the second order photon correlation function requires coincidence detection where photon pairs with a certain time delay between them are

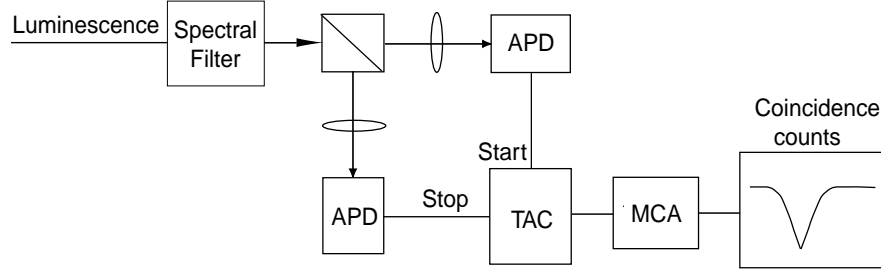


Figure 3.5: Hanbury Brown and Twiss Setup

detected. Coincidence detection is in principle possible with a single ideal detector that can perform one photon as well as two photon detections at all times; such a detector is technologically not available. Instead, two detectors and a 50%/50% beam splitter, i.e. *Hanbury Brown and Twiss setup* [31], can be used in coincidence detection. This measurement method is currently the only method used in second order photon correlation experiments. As we will see in this section, it is a very convenient measurement technique because it is not effected by the optical losses between the emitter and detector.

In the second order photon correlation experiments we filter specific transitions in the single quantum dot photoluminescence (single exciton emission, biexciton emission) and send them to our Hanbury Brown and Twiss (HBT) setup. Spectrometer or interference filters (1 nm or 0.5 nm FWHM, custom manufactured by Omega Optical Inc., Brattleboro, VT) combined with color filters are used in spectral filtering. The Hanbury Brown and Twiss setup (Figure 3.5) consists of a 50%/50% beam splitter and two single-photon-counting avalanche photodiodes (APD, Perkin Elmer model SPCM-AQR-14, timing resolution: 300 ps). The APDs are connected to the start and stop inputs of a time to amplitude converter (TAC, ORTEC Model 567) whose output is sent to a multichannel analyzer (MCA, ORTEC MicroACE). An electronic delay (ORTEC Model 425A) is introduced into the stop channel. The TAC detects coincidences corresponding to photon detection events in both APDs,

and converts the time delay between the two detection events into a voltage. Coincidence events with a time separation smaller than a certain maximum value (50 *ns* or 100 *ns* in our experiments) are only considered. Each output pulse of the TAC is then used to increment the value stored in one channel of the MCA, the MCA is selected to contain 512 channels in our experiments. By this way, after detection of sufficient number of coincidences, the MCA reveals the distribution of the number of coincidences $n(\tau)$ with respect to arrival time separation $\tau = t_{start} - t_{stop}$. The electronic delay introduced into the stop channel is used to check the symmetry around $\tau = 0$.

The measured distribution $n(\tau)$ is equivalent to the unnormalized correlation function $G^{(2)}(\tau)$ in the limit where the reciprocal of the average counting rate is much larger than the measured time separation (τ) between photon pairs. This requirement can be explained by calculating the coincidence detection probability in our HBT setup. Consider the total collection and detection efficiency of the start and stop APDs to be equal to η_{start} , and η_{stop} respectively. The total number of detected coincidences during a counting time T ($G_T^{(2)}(\tau)$) is given as:

$$G_T^{(2)}(\tau) = (1 - \eta_{stop}\Gamma_X\Delta\tau)^{\tau/\Delta\tau} \eta_{stop}\Gamma_X\Delta\tau \int_0^T \eta_{start}\Gamma_X dt \langle \hat{\sigma}_{X0}(t) \hat{\sigma}_{XX}(t + \tau) \hat{\sigma}_{0X}(t) \rangle$$

Since $\Delta\tau \ll \eta_{stop}\Gamma_X$ ($\Delta\tau = 100 - 200$ ps, $\eta_{stop}\Gamma_X \sim 10 - 100\mu s$) for our case, the equality:

$$\lim_{\Delta\tau \rightarrow 0} (1 - \eta_{stop}\Gamma_X\Delta\tau)^{\tau/\Delta\tau} = e^{-\eta_{stop}\Gamma_X\tau} \quad (3.5.1)$$

can be written. Using the above equality and Equation 3.2.3, the number of detected coincidences in channel τ after a total integration time of T can be written as:

$$G_T^{(2)}(\tau) = \int_0^T dt \eta_{start}\eta_{stop}\Gamma_X^2\Delta\tau e^{-\eta_{stop}\Gamma_X\tau} \langle \hat{\sigma}_{XX}(t) \rangle^2 g^{(2)}(\tau) \quad (3.5.2)$$

Thus, $G_T^{(2)}(\tau)$ found in Equation 3.5.2 corresponds to the unnormalized second order

photon correlation function $G^{(2)}(\tau)$ under the condition:

$$\eta_{stop}\Gamma_X\tau \ll 1 \quad (3.5.3)$$

This condition was always satisfied in our measurements ($\eta_{stop}\Gamma_X \sim 10 - 100 \mu s$, and $\tau < 50 ns$ or $\tau < 100 ns$).

The total detection efficiency of our HBT setup, including the extraction efficiency from the material, the collection efficiency of the microscope objective, the transmission of optics and spectral filters, and the quantum efficiency of the APDs, is estimated to be 5×10^{-5} when the spectrometer is used as the spectral filter and 0.1% when interference filters are used. We note that the requirement $\eta_{stop}\Gamma_X\tau \ll 1$ is not inherent in the HBT experiments, it is caused by our choice of using a TAC combined with a MCA in coincidence detection. This requirement can be easily removed by recording the photon streams in both APDs for large amount of times using proper electronics.

Finally, the time resolution of our HBT setup is 420 ps. Considering each APD's photon detection time is determined by a random process having Gaussian distribution, the probability distribution of joint detection of two photons at each APD will be given by the convolution of the two Gaussians. As each APD features a timing resolution of 300 ps, the resulting joint detection probability distribution has a FWHM of $\sqrt{2} \cdot 300 ps = 420 ps$.

3.5.2 Photon Antibunching in Single InAs Quantum Dots

In this section we present our experimental results on photon antibunching from single excitonic transitions of three different quantum dots. The first quantum dot is located in a bulk sample whose layer diagram is illustrated in Figure 2.3(a), the second quantum dot is located in a microdisk cavity of a microdisk sample (Figure 2.3(b)), and the third quantum dot is located in the bulk region of a microdisk sample (Figure 2.3(b)).

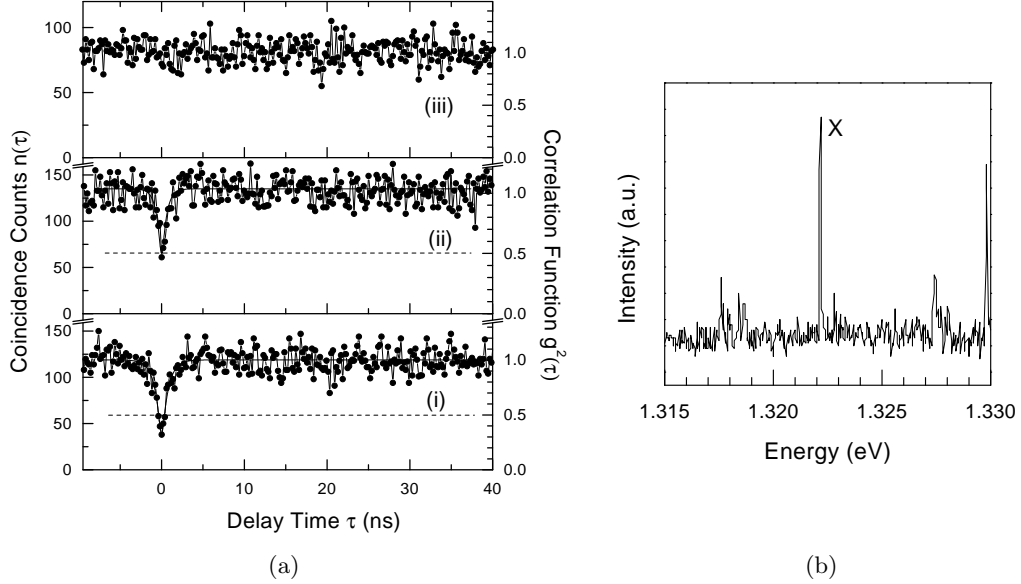


Figure 3.6: (a) Measured distribution of coincidence counts $n(\tau)$ and fit of the correlation function $g^{(2)}(\tau)$ (solid line) for a single bulk quantum dot, obtained at two different pump intensities: 66 Wcm^{-2} (Trace (i)) and 252 Wcm^{-2} (Trace (ii)). Trace (iii) shows the coincidence counts for many quantum dots in a high density region of the same sample. Single APD count rates are: $N_i=13000$ Hz, $N_{ii}=14500$ Hz, and $N_{iii}=15000$ Hz for traces (i), (ii) and (iii) respectively. (b) Photoluminescence spectrum of the bulk quantum dot quantum for a pump intensity of 66 Wcm^{-2} .

Figure 3.6(a) traces (i) and (ii) show the measured photon count distribution $n(\tau)$ for the single excitonic (X) transition of the single quantum dot in the bulk sample for two different pump intensities. These intensities correspond to an excitation of the quantum dot well below saturation (Trace (i)) and at the onset of saturation (Trace (ii)). Saturation is defined here as the pump intensity at which the X line reaches its maximum intensity [32]. Photoluminescence spectrum of the X line well below saturation (same pump intensity as Figure 3.6(a) trace (i)) is depicted in Figure 3.6(b). In Figure 3.6(a) traces (i) and (ii) exhibit clear dips in the correlation counts for a time delay $\tau=0$, indicating a strong photon antibunching.

The values of the normalized count distribution $\bar{n}(0)$ are 0.32 and 0.46 for traces (i) and (ii), respectively. These values are limited by the time resolution of our photon counting setup. In order to correct for the time resolution, the normalized count distribution $\bar{n}(\tau)$ is fit with the correlation function $g^{(2)}(\tau) = 1 - ae^{-|\tau|/t_m}$ convolved with a gaussian time distribution with 420 ps FWHM. For $g^{(2)}(\tau)$ a simple exponential time dependence is assumed. The parameter a accounts for the background present in the measurements. The resulting fitted $g^{(2)}(\tau)$ is shown as solid line in Fig. 3.6(a). The values of $1 - a = g^{(2)}(0)$ obtained from the fit are 0.23 and 0.34 for traces (i) and (ii). The fact that $g^{(2)}(0) < 0.5$ in both traces unambiguously indicates that the measured photon antibunching from the X transition stems from a single, anharmonic quantum emitter.

The measured correlation function $g^{(2)}(0)$ does not reach its theoretical minimum of zero because of the presence of background straylight. The correlation function $g_b^{(2)}(\tau)$ expected in the presence of a background radiation is $g_b^{(2)}(\tau) = 1 + \rho^2(g^{(2)}(\tau) - 1)$ where $\rho = S/(S+B)$ is the ratio of signal S to background B counts [25]. From optical emission spectra of the single quantum dot we can determine ρ for the X transition for the two pump intensities to be 0.9 and 0.83, respectively. The resulting values of $g_b^{(2)}(0)$ are 0.18 and 0.30, which are in good agreement with $g^{(2)}(0)$ values determined by the fits. The antibunching time constants t_m obtained from the fit of $g^{(2)}(\tau)$ are 750 ps and 450 ps for traces (i) and (ii). For comparison, trace (iii) of Fig. 3.6(a) shows the correlation for multiple emission lines of many quantum dots in a high-density region of the same sample. This correlation is flat over the complete measurement time and its normalized value of 1 corresponds to a Poissonian photon statistics. Here, many independent quantum dots contribute to the measured correlation and any possible signature of antibunching from a single dot is washed out.

Figure 3.7(a) shows the measured photon count distribution $n(\tau)$ for the X transition of a single quantum dot located in a microdisk cavity for two different pump intensities. The pump intensities correspond to an excitation of the quan-

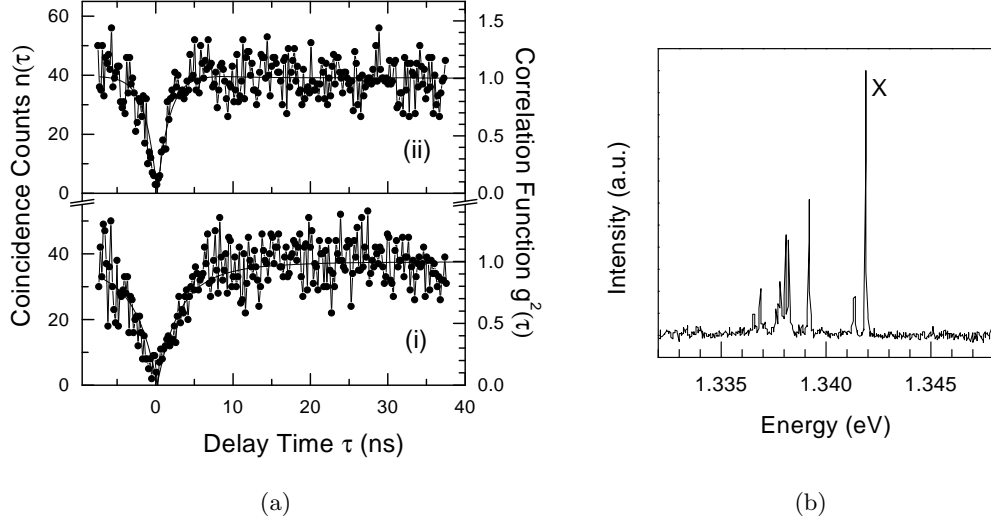


Figure 3.7: (a) Measured distribution of coincidence counts $n(\tau)$ and fit of the correlation function $g^{(2)}(\tau)$ (solid line) for a single quantum dot located in a microdisk cavity, obtained at three different pump intensities: 17 Wcm^{-2} (Trace (i)), and 56 Wcm^{-2} (Trace (ii)). Single APD count rates are: $N_i=6000 \text{ Hz}$, and $N_{ii}=7000 \text{ Hz}$ for traces (i), and (ii) respectively. (b) Photoluminescence spectrum of the quantum dot under a pump intensity of 55 Wcm^{-2} .

tum dot well below saturation (Trace (i)), and at the onset of saturation (Trace (ii)). We verified that the quantum dot did not couple to a mode of the microdisk resonator: the quantum dot X transition exhibits a resolution limited linewidth of $70 \mu\text{eV}$ (Figure 3.7(b)) whereas the nearest cavity mode (with linewidth $150 \mu\text{eV}$) is approximately 3 meV apart. In addition, at the pump intensities used in the correlation measurements no mode is apparent in the optical spectrum. Only at high pump intensities, when the single quantum dot ground state transition is highly saturated and broadens spectrally, cavity modes start to increase in intensity, thereby allowing for their identification. As the background radiation is weak for the quantum dot located in the microdisk, the correlation measurements of Figure 3.7(a) show very strong antibunching. The values of the normalized count distribution $\bar{n}(0)$ are

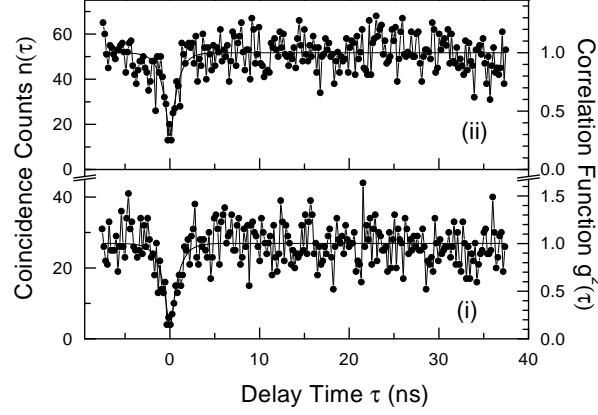


Figure 3.8: (a) Measured distribution of coincidence counts $n(\tau)$ and fit of the correlation function $g^{(2)}(\tau)$ (solid line) for a reference quantum dot in the bulk region of the microdisk sample, obtained at two different pump intensities: 60 Wcm^{-2} (Trace (i)) and 80 Wcm^{-2} (Trace (ii)).

0.05, and 0.08 for traces (i), and (ii) respectively. The fit of $g^{(2)}(\tau)$, yields values of $1 - a = g^{(2)}(0)$ of 0.02, and 0.00. The signal to background ratio for these measurements is determined to be $\rho = 0.98$, and 0.98 respectively. The values of $g_b^{(2)}(0)$ expected in the presence of background thus are 0.04, and 0.04; these values agree very well with the fitted values of $g^{(2)}(0)$. Hence, the data in Figure 3.7(a) correspond to a perfect antibunching in the radiation from a single quantum dot. The time constants for the exponential decay of the antibunching are determined from the fit to be 3.60 ns, and 1.41 ns for the two pump intensities. A reference measurement for a single quantum dot in an unprocessed part of the same microdisk sample also shows strong antibunching with time constants of 870 ps and 812 ps for pump intensities of 60 Wcm^{-2} and 80 Wcm^{-2} , respectively (Figure 3.8).

From the pump intensity dependent time constants measured in the experiments described above, the lifetime of a single exciton ground-state transition can be determined by using the three-level model discussed in Section 3.4. By comparing

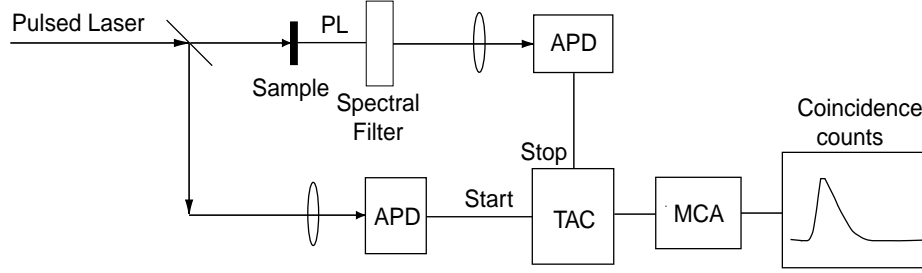


Figure 3.9: Time correlated single photon counting setup

the predictions of the model with the measured lifetime data the lifetime for the single exciton transition $t_X = 1/\Gamma_X$ in the limit of a vanishing pump rate is estimated to be 900 ± 100 ps (bulk sample), 1.10 ± 0.05 ns (microdisk sample, reference quantum dot in the unprocessed part) and 3.9 ± 0.5 ns (microdisk sample, quantum dot in a microdisk). The uncertainties in the lifetime values are mainly due to fluctuations of the pump intensity during the experiment (slight shifts of the translation stage positions cause a change of the effective pump rate) and the uncertainty in relating the measured pump intensities to pump rates in the theoretical model.

Even though the estimated lifetimes for the bulk quantum dots correspond well to values in the literature [33], the exciton lifetime of the quantum dot located in a microdisk cavity is considerably larger than the values previously reported. In our microdisk sample the quantum dots located in microdisk structures consistently exhibit lifetimes ranging from 2 to 4 ns. The difference in lifetimes could be explained by the different photonic environments quantum dots are located in. This point is discussed in Chapter 5.

3.5.3 Time-Correlated Single Photon Counting Experiments

As a further confirmation of the lifetime values determined by the second order photon correlation measurements, conventional lifetime measurements using time correlated single photon counting (TCPC) are performed [34]. Time correlated

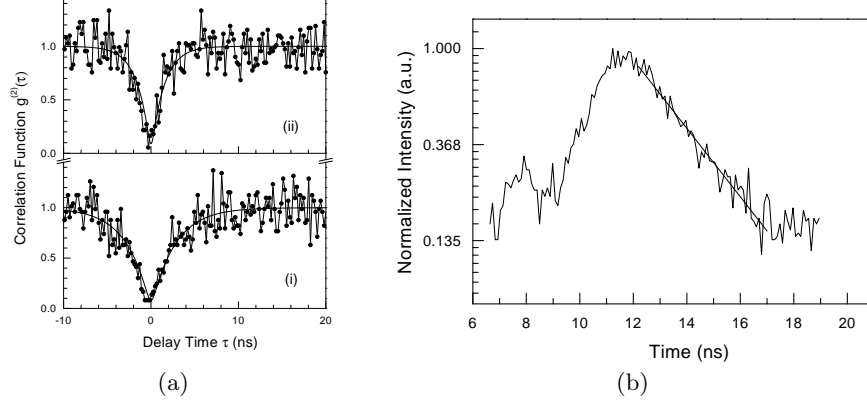


Figure 3.10: (a) Distribution of coincidence counts $n(\tau)$ and fit of the correlation function $g^{(2)}(\tau)$ (solid line) for a single quantum dot located in a microdisk cavity, obtained at pump intensities: 35 Wcm^{-2} (Trace (i)), and 90 Wcm^{-2} (Trace (ii)). (b) Result of TCPC measurement, the solid line corresponds to a decay time of 2.9 ns.

single photon counting experiments rely on excitation of the single quantum dot by a pulsed laser and monitoring the decay of the level populations after the trigger from the pulse. The setup is very similar to the Hanbury Brown and Twiss setup, in that TAC and MCA are still used to perform coincidence measurements, this time the pulsed laser is used to trigger the start APD and the stop APD is triggered by the photoluminescence from the quantum dot (Figure 3.9).

A comparison of the lifetime measurements performed by both TCPC and second order photon correlation experiments on a specific quantum dot is shown in Figure 3.10. Second order photon correlation experiments reveal decay times of 1.5 ns and 2.7 ns at pump power intensities of 90 Wcm^{-2} and 35 Wcm^{-2} that correspond to excitation below saturation and at the onset of saturation respectively (Figure 3.10(a)). From the three-level model, lifetime of this quantum dot is inferred to be $3.5 \pm 0.5 \text{ ns}$. TCPC measurement done on this quantum dot single exciton transition is shown in Figure 3.10(b). Since TCPC measurements give the decay of the population, in low excitation regime, the decay time in TCPC measurement gives the

population lifetime. Hence from Figure 3.10(b), the lifetime of this quantum dot is deduced to be $2.8\text{ns} \pm 0.5\text{ ns}$, provided this measurement is done in the low excitation regime which is also evident from the absence of a plateau. In Figure 3.10(b) the rise time is determined by the carrier capture time ($< 35\text{ ps}$, [18]), and limited by the time resolution of the coincidence detection using APDs (420 ps).

Chapter 4

Triggered Single Photon Emission

Conventional light sources such as light emitting diodes and lasers, generate radiation that can be fully described using classical Maxwell's equations. On the other hand, several applications in the emerging field of quantum information science require weak optical sources with strong quantum correlations between single photons [35]. A single photon turnstile device [36] which relies on triggered emission of individual photons is such a source that achieves the ultimate control in the photon generation process at the single photon level.

Quantum cryptography emerges as a potential area of application for a single photon turnstile device. An essential element of secure key distribution in quantum cryptography is an optical source emitting a train of pulses that contain one-and-only-one photon [37]. Since measurements unavoidably modify the state of a single quantum system, an eavesdropper cannot gather information about the secret key without being noticed, provided that the pulses used in transmission do not contain two or more photons. For applications in quantum cryptography, specific properties of single-photon pulses, such as precise photon energy, pulse duration and

bandwidth are not of primary importance.

Recently, it has also been shown that availability of a single-photon source enables implementation of efficient quantum computation using only linear optical elements and efficient photo-detectors [7]. This proposal relies heavily on two-photon interference on a beam-splitter for realization of probabilistic quantum gates and state preparation. It is therefore crucial to have a source that generates identical transform-limited single-photon pulses with vanishing time-jitter (Chapter 7).

Since its first proposal in 1994 [36], realization of a single photon turnstile device has been one of the holy grails of quantum electronics research. An extension of the first proposal was demonstrated in 1999 [38] where single as well as multiple photon emission events with a repetition rate of 10 MHz at 50 mK were reported. This device utilizes Coulomb blockade of tunneling for electrons and holes in a mesoscopic p-n diode structure to regulate the photon generation process. In this scheme, single electron and hole charging energies must be large compared to the thermal background energy to ensure single photon emission. Therefore, this device can only be operated at ultra-low temperatures ($T \leq 1$ K).

A triggered single-photon source based on π -pulse excitation of a single *Oxazine 720* molecule was proposed and demonstrated in 1996 [39], followed by other demonstrations on single *dibenzanthanthrene* (DBATT) molecules in 1999 [40] and single *terrylene* molecules in 2000 [41]. In contrast to the π -pulse excitation scheme, the latter two single photon sources rely on pulsed excitation of a strongly damped two-level system [42]. In the 1999 and 2000 demonstrations, using photon correlation measurements, it was concluded that approximately 74% and 73% of the pulses give rise to single photon emission or zero photon emission events at 1.8 K and room temperature with repetition rates of 3 MHz and 6.25 MHz respectively. Triggered single photon source based on adiabatic transfer in a single atom strongly coupled to a cavity mode was also proposed [43, 44, 45]. The demonstration of such a light source has been recently done, where each atom emitted up to seven photons [4] during its interaction with the cavity mode.

First unambiguous proofs of a triggered single photon source were demonstrated using single InAs quantum dots (2000 [6], 2001 [46, 47, 27]). These demonstrations revealed almost no probability of two or more than two photon emission events per pulse: 100% [6] and 89% [46] of the pulses gave rise to single or zero photon emission at 4 K and 5 K with repetition rates of 82 MHz and 76 MHz respectively. As explained in this chapter, triggered single-photon generation in single InAs quantum dots is achieved using a scheme similar to the one proposed for single molecules, i.e. pulsed laser excitation of a strongly damped single two-level emitter [48]. Recently, an electrically pumped single photon turnstile device [49] and single photon turnstile device based on N vacancies in diamond have also been demonstrated [50].

4.1 Generation of Single Photons From a Single Two-Level Emitter

Evidenced by the photon antibunching phenomenon, a two-level emitter cannot emit two photons at the same time. This special property of an antibunched light source can be explored to obtain a triggered single photon source where photon emission events are regulated by pulsed excitation. Consider a strongly damped two-level emitter [42] excited by a pulsed laser, under high excitation conditions each pulse brings the system to the excited state causing the emission of a single photon by spontaneous emission, and after the photon emission, the system is in the ground state waiting for the next pulse. Hence, each pulse triggers one and only one photon emission provided that the pulse width $\delta T \ll 1/\Gamma_{\text{spont}}$ to eliminate second photon generation, and pulse separation $T \gg 1/\Gamma_{\text{spont}}$ to ensure the recombination event (Figure 4.1(a)). For a radiatively damped two-level emitter [39], triggered single photon generation can be achieved using this same idea, by only making sure that the laser intensity is such that it provides a π – *pulse* that brings the system to the excited level at the end of each pulse. In this section triggered single photon generation based on a strongly damped two-level emitter will be analyzed only as

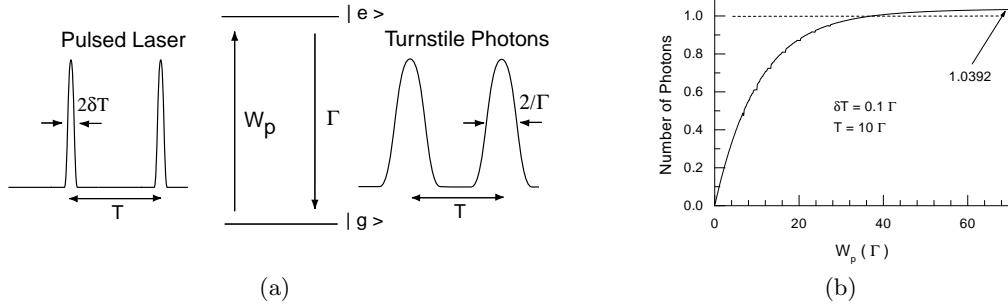


Figure 4.1: (a) Single photon generation from a two-level emitter (b) Average number of photons emitted per pulse

it is used in the treatment of the single InAs quantum dot single photon turnstile device under nonresonant excitation conditions.

4.1.1 A Strongly Damped Two-Level Emitter

The rate equations for the strongly damped two-level emitter are:

$$\frac{d}{dt} \begin{bmatrix} \langle \hat{\sigma}_{ee}(t) \rangle \\ \langle \hat{\sigma}_{gg}(t) \rangle \end{bmatrix} = \begin{bmatrix} W_p(t) & -\Gamma_{spon} \\ -W_p(t) & \Gamma_{spon} \end{bmatrix} \begin{bmatrix} \langle \hat{\sigma}_{ee}(t) \rangle \\ \langle \hat{\sigma}_{gg}(t) \rangle \end{bmatrix} \quad (4.1.1)$$

In Equation 4.1.1 the pulse shape is incorporated as the time dependent function $W_p(t)$. The average number of photons emitted per pulse is then given as [42]:

$$N = \int_0^T \Gamma \langle \hat{\sigma}_{ee}(t) \rangle dt$$

An example solution for this equation considering a square shaped pulse with a pulse width of $\delta T = 0.1\Gamma$ and pulse separation of $T = 10\Gamma$ is shown in Figure 4.1(b). In this Figure it is clear that after a certain pumping intensity each pulse triggers one and only one photon emission. The probability of exactly one photon emission per pulse is given by [42]:

$$P_1 = \left(\frac{W_p}{W_p - \Gamma} \right)^2 (e^{-\Gamma \delta T} - e^{-W_p \delta T}) - \frac{\Gamma W_p \delta T}{r - \Gamma} e^{-W_p \delta T}$$

At the high excitation regime $W_p = 50\Gamma$, $P_1 = 93.4\%$ of the pulses lead to single photon emission. This ratio would drastically increase for smaller excitation pulse width δT .

4.1.2 Monte Carlo Simulations

Second order photon correlation of the triggered single photon source presented in Section 4.1.1 can be analyzed using Monte Carlo techniques. Considering equation 4.1.1 together with the equation for second order correlation functions:

$$\frac{d}{d\tau} \begin{bmatrix} G_{ee}^{(2)}(\tau) \\ G_{gg}^{(2)}(\tau) \end{bmatrix} = \begin{bmatrix} W_p(t) & -\Gamma_{spon} \\ -W_p(t) & \Gamma_{spon} \end{bmatrix} \begin{bmatrix} G_{ee}^{(2)}(\tau) \\ G_{gg}^{(2)}(\tau) \end{bmatrix} \quad (4.1.2)$$

where $\tau = t - t'$, and $G_{ee}(\tau)$ represents the second order photon correlation function. The following Monte Carlo algorithm can be used in calculating the second order photon correlation function:

For each $t' \in [0, T]$:

- Pick a random number ϵ , $0 \leq \epsilon \leq 1$
- If $\epsilon < \langle \hat{\sigma}_{ee}(t') \rangle \Gamma \Delta t$ then decide that a valid start pulse is detected, calculate $G_{ee}^{(2)}(\tau)$ using Equation 4.1.2 with the initial conditions $G_{ee}^{(2)}(0) = 0$, $G_{gg}^{(2)}(0) = \langle \hat{\sigma}_{ee}(t') \rangle$
- If $\epsilon > \langle \hat{\sigma}_{ee}(t') \rangle \Gamma \Delta t$ then a valid start pulse is not detected, discard $G_{ee}^{(2)}(\tau)$
- $t' = t' + \Delta t'$

After many such iterations, the unnormalized second order photon correlation function $G^{(2)}(\tau)$ can be determined as: $G_{exp}^{(2)}(\tau) = G_{exp,ee}^{(2)}(\tau) = \frac{1}{N} \sum_{i=1}^N G_{ee}^{(2)}(\tau)$. An example simulation of this algorithm is shown in Figure 4.2. In this Figure the signature of the triggered single photon source operation is the absence of the peak around $\tau = 0$. For a pulsed periodic coherent source which emits Poissonian light,

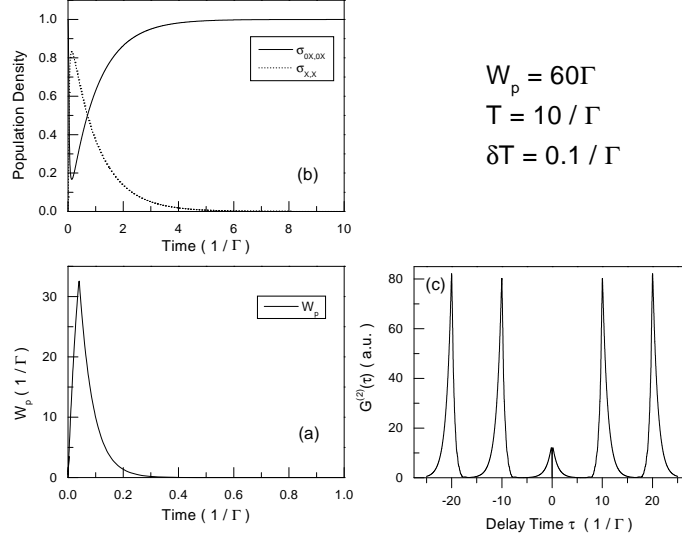


Figure 4.2: Monte Carlo analysis of a strongly damped two-level emitter.

the peak at $\tau = 0$ would be identical to the peaks at integer multiples of the repetition rate T , for all values of the mean photon number. In contrast, for an ideal turnstile device, the peak at $\tau = 0$ is absent [51] indicating sub-Poissonian photon statistics. In Figure 4.2(c) the small peak that appears around $\tau = 0$ is due to secondary photon emission events from the two-level emitter. For smaller pulse widths, as the quality of the turnstile operation improves, this peak around $\tau = 0$ would disappear.

4.2 Single InAs Quantum Dot Single Photon Turnstile Device

Using single quantum dots, regulation of photon emission process can be achieved under pulsed excitation due to a combination of the anharmonic multi-

exciton spectrum and slow relaxation of highly-excited quantum dots leading to vanishing re-excitation probability following the photon emission event at the single exciton transition [48]. Under high intensity nonresonant excitation conditions, two or more electron-hole pairs are captured by the quantum dot during each excitation pulse. Since the total recombination time of the multiexciton quantum dot state (1 - 4 ns [26, 33]) is longer than the recombination time of the free electron-hole pairs (~ 300 ps [52]), each excitation pulse can lead to at most one photon emission event at the single excitonic transition. Provided that the quantum dot single excitonic recombination is predominantly radiative at liquid Helium temperatures [26], and the single excitonic recombination is not spectrally shifted by the existence of neighboring trapped charges, every excitation pulse from the mode-locked laser will generate an ideal single photon pulse emitted at the single excitonic recombination energy.

Figure 4.3 shows power dependent photoluminescence characteristics of a single quantum dot under nonresonant pulsed excitation. Power dependence of the single excitonic emission intensity shows the first signs of single photon source operation (Figure 4.3 inset). The single excitonic emission saturates at a certain pump power that corresponds to the pump power at which the average number of excitons in the s-Shell is 1. For larger pumping intensities, the emission level stays constant indicating that the increase in the average number of excitons in the quantum dot has no effect on the number of photons emitted from the single excitonic transition. This is the first signature of a single photon turnstile device. The unequivocal proof of the single photon operation is provided by the second order photon correlation experiments as discussed in the following sections.

4.2.1 Analysis of a Three-Level Emitter

The analysis of the second order photon correlation function of the single quantum dot can be done by assuming the quantum dot as a three-level system and

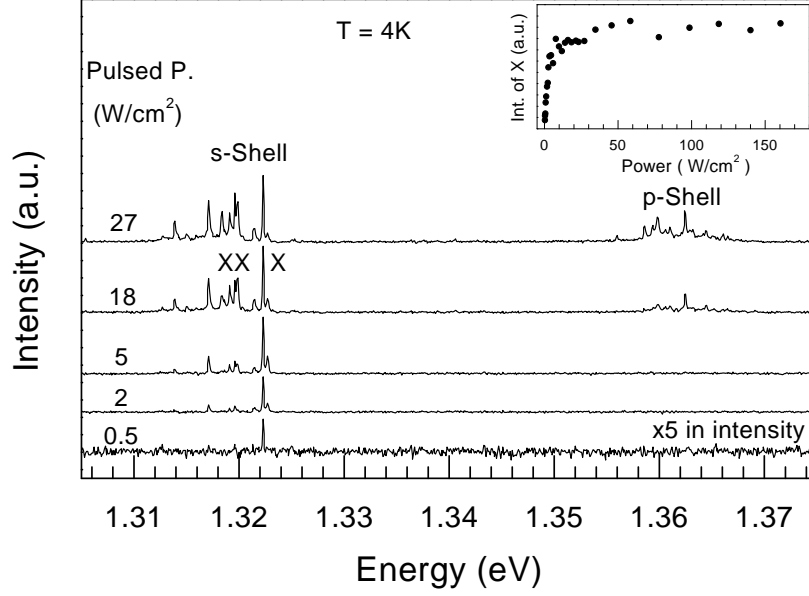


Figure 4.3: Power dependent photoluminescence spectra of a quantum dot located in a microdisk under nonresonant pulsed excitation. Saturation of single excitonic emission is visible in the inset.

incorporating the effect of the free-carriers in the excitation pulse width. Figure 4.4 shows the result of such an analysis in which $\tau_X = 1.5 \text{ ns}$, $\tau_{XX} = 0.75 \text{ ns}$ were assumed together with $\tau_{pulse} = 300 \text{ ps}$, considering free-carrier lifetime of 300 ps. The absence of a peak around $\tau = 0$ is the signature of the triggered single photon source.

This simulation indeed corresponds to the worst case scenario because lifetime of the free carriers generated in the wetting layer can be 300 ps or larger however those generated in the substrate have much smaller lifetimes. We do not know which of these free carriers are more efficiently captured by our quantum dots. Moreover the quantum dots located in microdisk cavities have lifetimes longer than 2 ns due

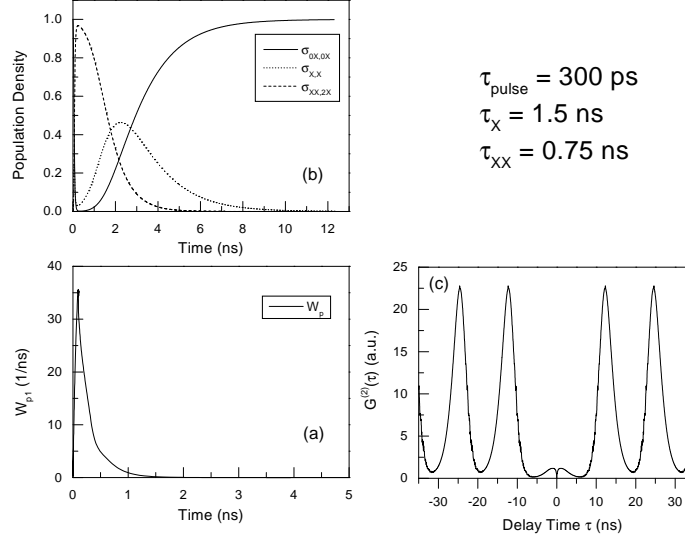


Figure 4.4: Monte Carlo analysis of the strongly damped three-level model. Considering $\tau_{\text{pulse}} = 300 \text{ ps}$, $\tau_X = 1.5 \text{ ns}$, $\tau_{XX} = 0.75 \text{ ns}$, and $W_{pXX} = 2W_{pX}$ in average 1.0735 photons are emitted per pulse.

to the effect of the photonic environment as discussed in Chapter 3, and biexcitonic emission lifetime is longer than half of the single excitonic emission lifetime for our quantum dots (Chapter 6).

4.2.2 Experimental Results

In this section we demonstrate our experimental results on single photon operation obtained from two separate quantum dots. Results from one quantum dot are depicted in Figures 4.5, and 4.6 while results from the other quantum dot are shown in Figure 4.7. Both of these quantum dots are embedded in $5 \mu\text{m}$ microdisks.

Figure 4.5(a) shows the photoluminescence spectrum of the first single quantum dot investigated in this section, taken under continuous wave excitation. The resolution limited photoluminescence peak at 1.3406 eV (shown by the arrow in the

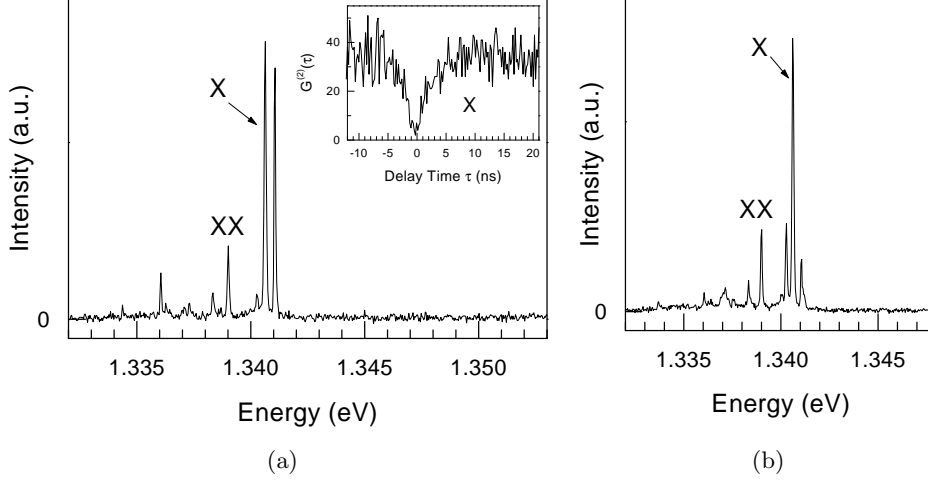


Figure 4.5: Photoluminescence spectrum of a single InAs quantum dot embedded in a $5\ \mu\text{m}$ diameter taken microdisk under nonresonant continuous wave (a) and pulsed excitation (b) conditions. Contributions from the excitonic ground state transition (X), and higher excited states (e.g. biexciton (XX)) are visible. Inset in figure (a): Measured unnormalized correlation function $G^{(2)}(\tau)$ of the single quantum dot X transition under continuous wave excitation.

figure) is identified as due to the single excitonic (X) recombination while the peak at 1.3410 eV is probably due to a charged excitonic recombination (Chapter 6). The photon correlation experiment shown in the inset of Figure 4.5(a) was performed for the X peak shown in Figure 4.5(a); we were able to filter only the X transition by using the spectrometer. The feature at 1.339 eV shows a superlinear increase with excitation intensity and originates from a biexciton decay (XX). The inset shows the measured unnormalized continuous wave correlation function $G^{(2)}(\tau)$ for the same X transition at a pump power much smaller than the onset of saturation. Saturation is defined here as the pump intensity where the X line reaches its maximum intensity [32]. The dip at $\tau = 0$ arises from photon antibunching and the fact that $g^{(2)}(\tau) < 0.5$ proves that the light from the X transition stems from a single quantum dot.

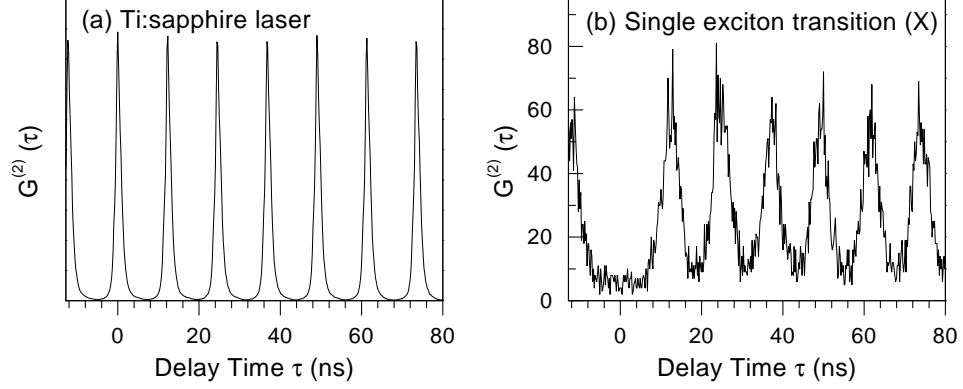


Figure 4.6: Measured unnormalized correlation function $G^{(2)}(\tau)$ of (a) a mode-locked Ti:Sa laser (FWHM = 250 fs), and (b) a single quantum dot single excitonic ground state (X) emission under pulsed excitation conditions (82 MHz). The quantum dot X transition was out of resonance with the microdisk modes.

For the quantum dot mentioned in the previous paragraph, we obtained the photoluminescence spectrum depicted in Figure 4.5(b) under nonresonant pulsed excitation conditions. We note that due to different excitation conditions (continuous wave (Figure 4.5(a)) and pulsed (Figure 4.5(b))) the relative intensity of emission peaks from the same quantum dot are different in Figure 4.5(a) (continuous wave excitation), and Figure 4.5(b) (pulsed excitation). This is due to the charged exciton phenomenon, from Figures 4.5(a), and 4.5(b) we can conclude that for this specific quantum dot, charged excitonic emission is more favored under nonresonant continuous wave excitation than it is under nonresonant pulsed excitation. This point is further addressed at the end of this chapter, and in Chapter 6.

Figure 4.6 shows the measured unnormalized correlation function $G^{(2)}(\tau)$ for (a) the pulsed Ti:Sa laser, and (b) the X transition depicted in Figure 4.5(b). At 4 K, the emission of this quantum dot is far detuned from all microdisk whispering gallery modes. The experiment shown in Figure 4.6(b) is performed at a pump

intensity corresponding to an excitation level well larger than the saturation power of the X emission. As expected, the measured $G^{(2)}(\tau)$ of the pulsed Ti:Sa laser exhibits peaks at integer multiples of pulse separation, $T = 12.27$ ns, with negligible signal in between the peaks. The measured $G^{(2)}(\tau)$ of the X emission at $T = 4$ K (Figure 4.6(b)) also shows peaks at integer multiples of T , indicating the locking of the photon emission to the pulsed excitation. However, in contrast to the photon correlation function of the mode-locked laser, the peak at $\tau = 0$ is no longer present, i.e., the probability of finding a second photon following the detection of the first photon at $\tau = 0$ vanishes. Absence of the peak at $\tau = 0$ provides strong evidence for an ideal single photon turnstile operation.

The lifetime of the single excitonic transition (X) was determined from continuous wave antibunching experiments to be 2.2 ns (Figure 4.5(a) inset), which is the shortest possible time it takes before a single excitonic recombination event for this quantum dot. As the recombination time in the GaAs barrier and the wetting layer is considerably faster (~ 300 ps [52]), following the excitation by each pulse, no free carriers are available to re-excite the quantum dot after the X recombination process. This is also evident in the simulation results shown in Figure 4.4. Therefore at most one X recombination process per pulse can occur under these conditions. To ensure that a single photon is indeed emitted for each excitation pulse, the pump power of the excitation laser should be adjusted so that the probability of having no injected electron-hole pair in the quantum dot is negligible. The fact that the photon correlation measurement depicted in Fig. 4.6b was obtained well in the saturation regime ensures that the quantum dot is multiply-excited in our experiments, implying one and only one X recombination event per pulse. Furthermore, for our samples the dominant recombination mechanism is radiative, at liquid He temperatures (quantum efficiency, $\eta \sim 1$). This is due to the fact that the lifetimes of our quantum dots are prolonged (inhibited spontaneous emission (Chapter 5)) when they are located in microdisk cavities due to the change in the available optical mode density, and zero point field fluctuations. If the dominant recombination mechanism were nonradiative,

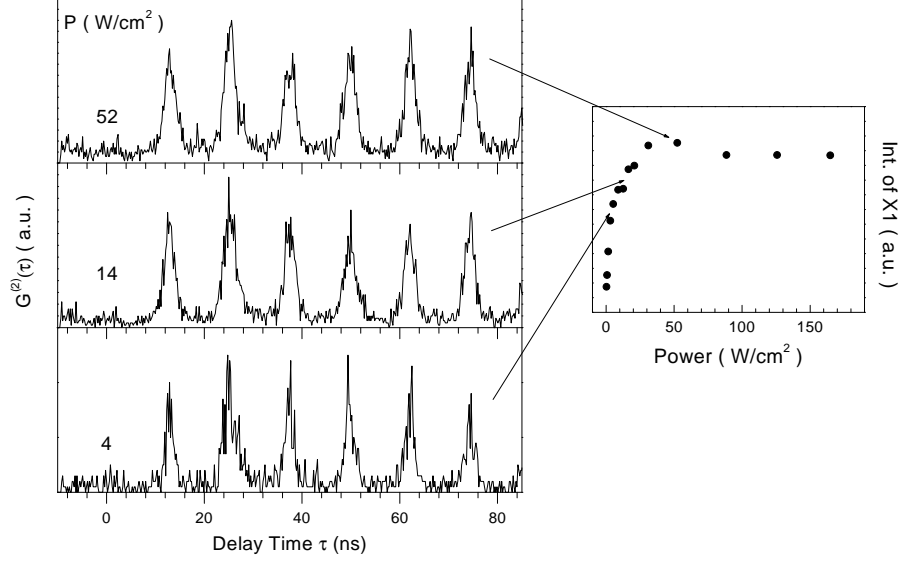


Figure 4.7: Measured unnormalized correlation function $G^{(2)}(\tau)$ of a single quantum dot single excitonic ground state (X) emission under pulsed excitation conditions (82 MHz) at power levels below and above saturation.

different photonic environment of the microdisk cavities would not have such an effect, the only possible change in the lifetime could be a decrease due to the increased number of surface states. These facts allow us to conclude that the generated light at the excitonic ground-state transition energy X is a stream of single photons with a repetition rate of 82 MHz.

Pump power dependent measurements of $G^{(2)}(\tau)$ of another quantum dot whose single excitonic emission is not coupled to any microdisk whispering gallery modes are depicted in Figure 4.7. This figure shows that $G^{(2)}(0)$ is essentially independent of excitation pulse power. These results indicate that probability of two photon emission (per pulse) is negligible even when the X transition is well below saturation. In Figure 4.7 it is also apparent that the FWHM of the peaks increases

with pumping power. This is due to the increase in the time-jitter of single photon emission events caused by larger multi-excitonic decay times at higher pump powers.

Even though the sub-Poissonian photon statistics persists in a single photon turnstile device at all collection efficiencies, for such a source to become widely practical, high collection efficiency is strongly required. From that respect, InAs quantum dot turnstile device has a clear advantage over single molecule based single photon sources: it can be incorporated in the III-V semiconductor microcavity structures. A single InAs quantum dot can be resonantly coupled to a microcavity (e.g. micropillar) mode ensuring a high collection efficiency provided that the cavity structure has a directional output [48, 53, 54]. Furthermore, when a high-Q, low volume microcavity is used, the Purcell effect can significantly reduce the jitter in the single photon emission time. We have indeed demonstrated that coupling a single quantum dot to a microdisk whispering gallery mode significantly reduces the photon emission time jitter [6, 55]. This demonstration together with other points related to cavity - quantum dot coupling are explained in Chapter 5.

Despite these facts, a limitation in obtaining a high collection efficiency from the single quantum dot single photon source is the existence of charged excitons (Chapter 6). Under nonresonant excitation conditions, InAs quantum dots capture carriers individually as well as in pairs; hence in proper excitation intensities single excitonic recombination in the presence of a single charge in the quantum dot is probable. This would prevent the true single photon operation as each photon is not emitted via a neutral excitonic (X) recombination. A nearby acceptor or donor impurity atom would also increase the relative intensity of charged excitonic emission causing imperfect single-photon operation. Charged excitonic recombination due to impurity atoms can be avoided by minimizing the chamber contamination during the MBE growth, while p-shell excitation can be used to avoid charged excitonic emission due to single carrier capture events, as explained in Chapter 7.

We envision that using cavity-enhanced collection efficiency and cavity-enhanced radiative recombination, our single photon turnstile device could generate

single photon pulses at a repetition rate up to $> 100\text{ MHz}$. The operating temperature of the InAs quantum dot single photon source can be easily extended to $T=77\text{ K}$, which would be very significant for practical applications. Furthermore our single photon source has the potential to emit transform limited single photons at temperatures smaller than 10 K as we discuss in Chapter 7. This is a crucial property for its application in linear optics quantum computation [7].

Chapter 5

Cavity-QED Using Single Quantum Dots

The elementary system in cavity-quantum electrodynamics (QED) is a two-level emitter interacting resonantly with a single cavity mode. Basic properties of the two-level emitter can be dramatically modified if the photon lifetime, determined by the cavity quality (Q) factor, is long, and the electric field per photon (E_{vac}) inside the cavity, determined by the square root of the reciprocal cavity volume (V_{cav}), is large. Depending on the coupling strength between the two-level emitter and the cavity mode, spontaneous emission can be enhanced (weak coupling regime) or becomes *reversible* (strong coupling regime) [56]. Since the 1980s, several experiments have demonstrated that radiative decay rate can be significantly modified by placing atoms inside a cavity structure in the weak coupling cavity-QED regime [57]. Experiments based on a single atom injected into a high-Q cavity have achieved the strong-coupling regime of cavity-QED, which in turn enabled the demonstration of conditional quantum dynamics [58], decoherence of mesoscopic superposition of quantum states, and creation of entanglement between three distinguishable quantum systems [59].

Two-level nature of the single excitonic transition of single quantum dots, that was unequivocally demonstrated in the previous chapters, together with the advanced semiconductor microcavity processing capabilities, makes cavity-QED research in InAs quantum dots highly rated. This field of research promises applications such as high speed light sources [48] and quantum information processing [60]. Since quantum dot location inside the cavity is fixed by the growth, this system is free of the stringent trapping requirements that limit its atomic counterpart. The maximum time a single atom could have been trapped so far has been a few seconds [61], in contrast, single quantum dots are naturally trapped for years.

The first results on cavity-QED using quantum dots dates to 1998 [62] where enhanced spontaneous emission in the weak coupling cavity-QED regime has been observed from an ensemble of quantum dots embedded in *micropillar* cavities. Since then, weak coupling cavity-QED regime has been reached by using ensemble of quantum dots embedded in *microdisk* cavities (1999 [48], 2002 [63]), and single quantum dots embedded both in *microdisk* (2001 [55]) and *micropillar* cavities (2001 [54]). Strong coupling regime using quantum dots is still a rather difficult experimental challenge to be met [64]. Improvements in microcavities towards larger Q values, and smaller mode volumes are necessary for that purpose.

In this chapter, first the basic theoretical treatment for cavity-QED is given, then microdisk whispering gallery modes are presented, followed by the experimental results showing weak coupling cavity-QED regime. We will also discuss our observation of inhibited spontaneous emission from quantum dots located in microdisk cavities.

5.1 Analysis of Cavity-Single Quantum Dot Interaction

The general treatment of cavity-QED can be done using the Jaynes-Cummings Hamiltonian, from which the Rabi oscillations and normal mode splitting can be deduced. Such a treatment where an ideal dipole and cavity are considered is done

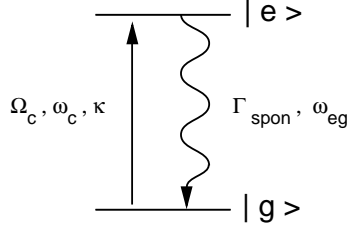


Figure 5.1: Two-level emitter coupled to a cavity mode

in Appendix B. In this section however, a realistic scenario of single quantum dot - microcavity coupling is investigated considering spontaneous emission and cavity decay rate.

For a two-level system depicted in Figure 5.1, resonantly coupled to a microcavity mode, considering broadenings in the dipole (γ) due to spontaneous emission and cavity mode (κ) due to coupling to an outside reservoir, a master equation can be written as [56]:

$$\begin{aligned} \frac{d}{dt}\hat{\rho} = \frac{1}{i\hbar}[\hat{H}', \hat{\rho}] + \gamma(2\hat{\sigma}_{ge}\hat{\rho}\hat{\sigma}_{eg} - \hat{\sigma}_{ee}\hat{\rho} - \hat{\rho}\hat{\sigma}_{ee}) \\ + \kappa(2\hat{a}\hat{\rho}\hat{a}^\dagger - \hat{a}^\dagger\hat{a}\hat{\rho} - \hat{\rho}\hat{a}^\dagger\hat{a}) \end{aligned} \quad (5.1.1)$$

In the low excitation limit, where the cavity is assumed to host in average not more than one photon, equation 5.1.1 can be solved considering only the vectors $|g, 0\rangle$, $|e, 0\rangle$, and $|g, 1\rangle$, revealing the following equations for the mean values of \hat{a} , and $\hat{\sigma}_{eg}$:

$$\frac{d}{dt} \begin{bmatrix} \langle \hat{a}(t) \rangle \\ \langle \hat{\sigma}_{eg}(t) \rangle \end{bmatrix} = \begin{bmatrix} i\omega_0 - \kappa & \Omega_C \\ -\Omega_C & i\omega_0 - \gamma \end{bmatrix} \begin{bmatrix} \langle \hat{a}(t) \rangle \\ \langle \hat{\sigma}_{eg}(t) \rangle \end{bmatrix} \quad (5.1.2)$$

The eigenvalues of this equation are:

$$\lambda = i\omega_0 - \left(\frac{\kappa + \gamma}{2}\right) \pm \sqrt{\left(\frac{\kappa - \gamma}{2}\right)^2 - \Omega_C^2}$$

(i) In strong coupling regime ($\Omega_C > \frac{|\kappa - \gamma|}{2}$):

$$\lambda = i\omega_0 - \left(\frac{\kappa + \gamma}{2}\right) \pm i\sqrt{\Omega_C^2 - \left(\frac{\kappa - \gamma}{2}\right)^2} \quad (5.1.3)$$

the system exhibits Rabi oscillations with angular frequency $\sqrt{\Omega_C^2 - (\frac{\kappa-\gamma}{2})^2}$ as well as a coherence decay rate of $\frac{\kappa+\gamma}{2}$.

(ii) In weak coupling regime ($\Omega_C < \frac{|\kappa-\gamma|}{2}$), considering $\kappa \gg \gamma$:

$$\begin{aligned}\lambda_A &= i\omega_0 - \gamma(1 + \frac{\Omega_C^2}{\kappa\gamma}) \\ \lambda_C &= i\omega_0 - \kappa(1 - \frac{\Omega_C^2}{\kappa^2})\end{aligned}\tag{5.1.4}$$

λ_A is the dipole-like solution while λ_C is the cavity-like solution. The dipole-like solution decays with an enhanced rate of $\gamma(1 + \frac{\Omega_C^2}{\kappa\gamma})$, the enhancement factor, $\frac{\Omega_C^2}{\kappa\gamma}$, is the Purcell factor [65, 64]. From λ_C in the above solutions, it is also seen that the decay of the cavity-like solution is inhibited, however the inhibition factor, $\frac{\Omega_C^2}{\kappa^2}$, is negligibly small in the assumed weak coupling regime ($\kappa \gg \gamma$).

The solution studied in case (ii) is the relevant situation for the experimental results that we are going to demonstrate. This Purcell regime assumes a broad cavity mode (κ) and a relatively small dipole-cavity mode coupling strength (Ω_C). This regime can also be investigated by using the Fermi Golden rule. Spontaneous emission rate is given by the following formula when the dipole is assumed to be coupled to a large number of optical modes available:

$$\frac{1}{\tau} = \frac{2\pi}{\hbar^2} \rho(\omega_{eg}) E_{max}^2 \langle |\langle \mu_{eg} \cdot \epsilon \rangle|^2 \rangle \tag{5.1.5}$$

where $\hat{\rho}(\omega_{eg})$, E_{max} , μ_{eg} , and ϵ denote the available optical mode density, maximum field per photon, dipole matrix element, and the field polarization respectively. For a constant refractive index environment, the optical mode density is $\hat{\rho}_{uni}(\omega_{eg}) = \frac{\omega_{eg}^2 V n^3}{\pi^2 c^3}$, $E_{max,vac} = \sqrt{\frac{\hbar \omega_{eg}}{2\epsilon_0 n^2 V_{eff}}}$, and $\langle |\langle \mu_{eg} \cdot \epsilon \rangle|^2 \rangle = \frac{1}{3} |\mu_{eg}|^2$ considering the random polarization of the vacuum modes. The uniform index material spontaneous emission is then given as:

$$\frac{1}{\tau_{uni}} = \frac{\omega_{eg}^3 n}{3\pi \epsilon_0 \hbar c^3} |\mu_{eg}|^2 \tag{5.1.6}$$

When the dipole is coupled to a specific broad cavity mode however, the optical mode density becomes $\hat{\rho}_{uni}(\omega_{eg}) = \frac{2Q}{\pi \omega_{eg}}$, revealing the spontaneous emission

rate:

$$\frac{1}{\tau_{cav}} = \frac{2Q}{\hbar\epsilon_0 n^2 V_{eff}} \langle |\langle \mu_{eg} \cdot \epsilon \rangle|^2 \rangle \quad (5.1.7)$$

Hence the Purcell enhancement in the spontaneous emission rate is:

$$F_P = \frac{1/\tau_{cav}}{1/\tau_{uni}} = \frac{3}{4\pi^2} \frac{Q(\lambda_{eg}/n)^3}{V_{eff}} \frac{\langle |\langle \mu_{eg} \cdot \epsilon \rangle|^2 \rangle}{|\mu_{eg}|^2} \quad (5.1.8)$$

This equality of the Purcell factor can also be driven from the Equation 5.1.4 where an enhancement in spontaneous emission by $\frac{\Omega_C^2}{\kappa\gamma}$ was found. Substituting the equations for Ω_C , κ , and γ :

$$\begin{aligned} \Omega_C &= \frac{2|\mu_{eg} \cdot \epsilon| E_{max}}{\hbar}, \quad \kappa = \frac{Q}{\omega_{eg}}, \quad \gamma = \frac{\omega_{eg}^3 n}{3\pi\epsilon_0 \hbar c^3} |\mu_{eg}|^2 \\ \Rightarrow F_P &= \frac{\Omega_C^2}{\kappa\gamma} = \frac{3}{4\pi^2} \frac{Q(\lambda_{eg}/n)^3}{V_{eff}} \frac{\langle |\langle \mu_{eg} \cdot \epsilon \rangle|^2 \rangle}{|\mu_{eg}|^2} \end{aligned}$$

5.2 Microdisk Whispering Gallery Modes

5.2.1 Analysis of Whispering Gallery Modes

Microdisk cavities are easy-to-process microcavities that provide highly confined optical resonances named whispering gallery modes [66]. These modes can have high Q values for relatively small mode volumes ($Q = 12000$ for a $2 \mu m$ microdisk, $V_{cav} \approx 50(\lambda/2n)^3$ [19]) due to the strong photonic confinement, making them suitable for cavity-QED studies despite the fact that they do not provide directional emission. These resonances that are confined by total internal reflection, circulate around the disk circumference. They are characterized by azimuthal (M) and radial (N) mode numbers, where M determines the azimuthal dependence $\exp(iM\phi)$ and N-1 denotes the number of nodes in the radial direction (Figure 5.2). They exhibit a two-fold degeneracy due to the azimuthal dependence (M, and -M). The whispering gallery modes with N=1 are contained within a ring width of $\lambda/2n$ [66]. For our microdisk structures only low radial number modes (N = 1, 2, 3) are observable since the post provides large optical losses for high radial number modes.

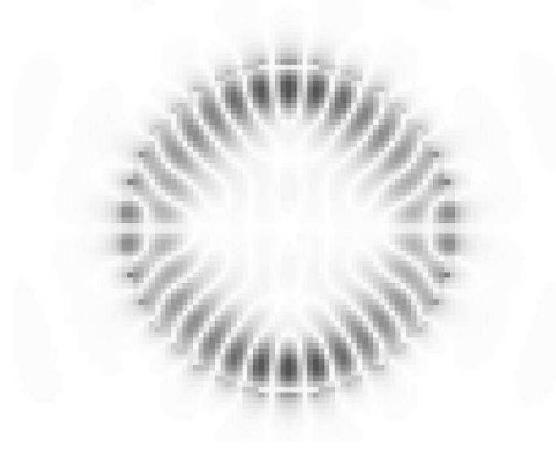


Figure 5.2: Finite difference time domain simulation of a whispering gallery mode characterized by $M=17$, and $N=11$. Asymmetry in the mode shape is due to the finite mesh size.

In order to solve for the whispering gallery modes, a disk standing freely in the air can be considered. Since the whispering gallery modes of interest are not considerably coupled to the post region, this assumption is justified. Then considering the microdisk as a slab, the three dimensional problem can be approximately reduced to two dimensions by using an effective refractive index [67] (Figure 5.3). For disk thickness $d < \lambda/2n$ only the lowest order transverse electric (TE) mode is dominant over the slab's thickness. For this radially oriented electric field (direction \mathbf{r} in Figure 5.3(b)) the following boundary conditions can be written:

$$\begin{aligned} A \cos(k_z \frac{d}{2}) &= B e^{-\alpha \frac{d}{2}} \\ A k_z \sin(k_z \frac{d}{2}) &= B \alpha e^{-\alpha \frac{d}{2}} \Rightarrow k_z \tan(k_z \frac{d}{2}) = \alpha \end{aligned}$$

where k_z and α are defined as: $k_z^2 = k_0^2(n_0^2 - n_{xy}^2)$ and $\alpha^2 = k_0^2(n_{xy}^2 - 1)$, and n_{xy} denotes the effective index of the two dimensional problem. Using these relationships k_z can be solved from:

$$k_z \tan(k_z \frac{d}{2}) = \sqrt{k_0^2(n_0^2 - 1) - k_z^2}$$

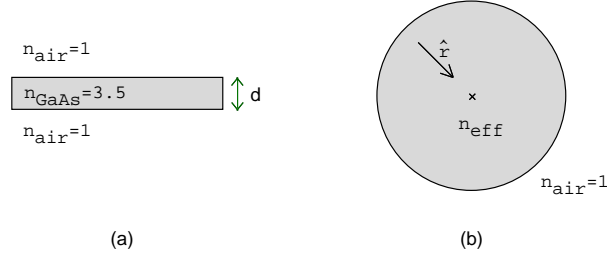


Figure 5.3: Effective index approximation

The effective index can then be calculated as: $n_{xy}^2 = \frac{k_0^2 n_0^2 - k_z^2}{k_0^2}$

The whispering gallery resonances are then given by the solution of the two dimensional Helmholtz equation:

$$\nabla^2 \psi + n_{xy}^2 k_0^2 \psi = 0$$

The above equation has eigensolutions in the form $\psi = e^{im\phi} J_m(n_{xy} k_0 \rho)$ where J_m corresponds to the m^{th} order Bessel function. Due to strong in-plane confinement of the whispering gallery resonances, perfect conductor boundary conditions in the microdisk plane can be imposed to a good approximation revealing the relationship $n_{xy}^2 k_0^2 = \frac{x_{mq}^2}{R^2}$ where R denotes the radius of the microdisk, and x_{mq} denotes the q^{th} root of m^{th} order Bessel function. This solution is referred to as $TE_{M,N}$, M and N correspond to azimuthal and radial mode numbers respectively. In summary the relevant highly confined $TE_{M,N}$ whispering gallery resonances can be approximately solved by the below set of equations:

$$k_z \tan(k_z \frac{d}{2}) = \sqrt{k_0^2 (n_0^2 - 1) - k_z^2} \quad (5.2.1)$$

$$n_{xy}^2 k_0^2 = \frac{x_{mq}^2}{R^2} \quad (5.2.2)$$

Solution of Equations 5.2.1, and 5.2.2 for radial numbers $N=1$, and 2 is depicted in Figure 5.4.

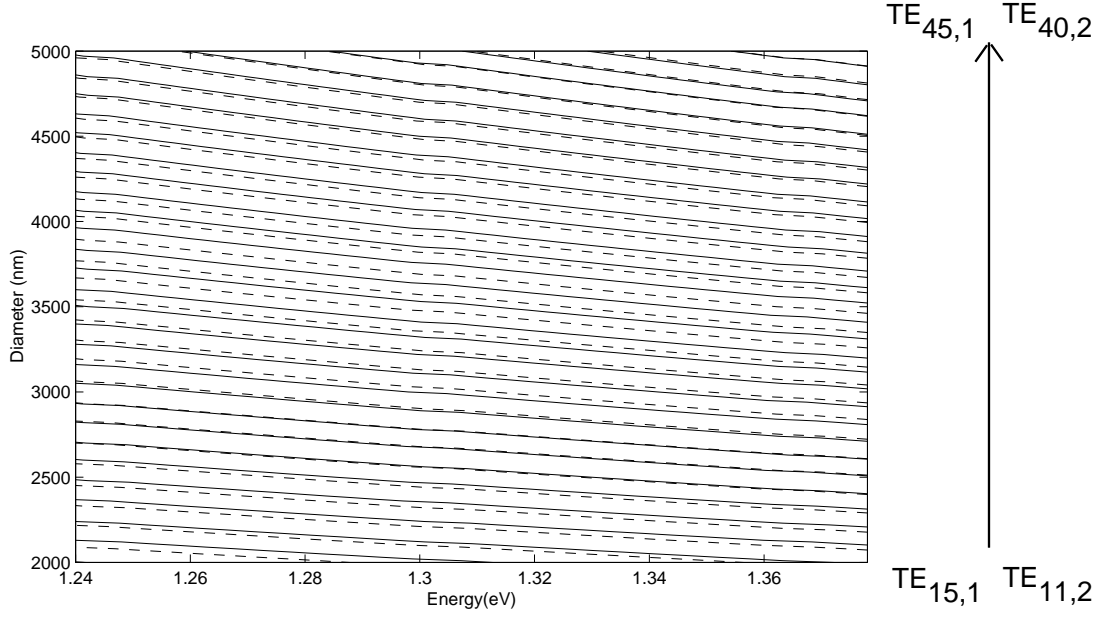


Figure 5.4: Calculated microdisk whispering gallery modes for different disk diameters. Solid lines correspond to $TE_{x,1}$ modes for $x=15, 45$, dashed lines correspond to $TE_{x,2}$ modes for $x=11, 40$

5.2.2 Experimental Analysis of Whispering Gallery Modes

We determined the whispering gallery modes by performing regular photoluminescence experiments on microdisks having quantum dots embedded in their center planes. Using the coupling between the quantum dots and whispering gallery modes we were able to indirectly couple to whispering gallery modes by exciting the quantum dots. Quantum dot emission that was coupled to whispering gallery modes were then readily observable in the photoluminescence spectrum. This measurement is an efficient way of determining the whispering gallery modes, we do not need to couple to the modes in special manners to observe their emission.

Figures 5.5, and 5.6 show photoluminescence spectra obtained from $4.5 \mu m$, and $2 \mu m$ diameter microdisks having high density quantum dots embedded in their

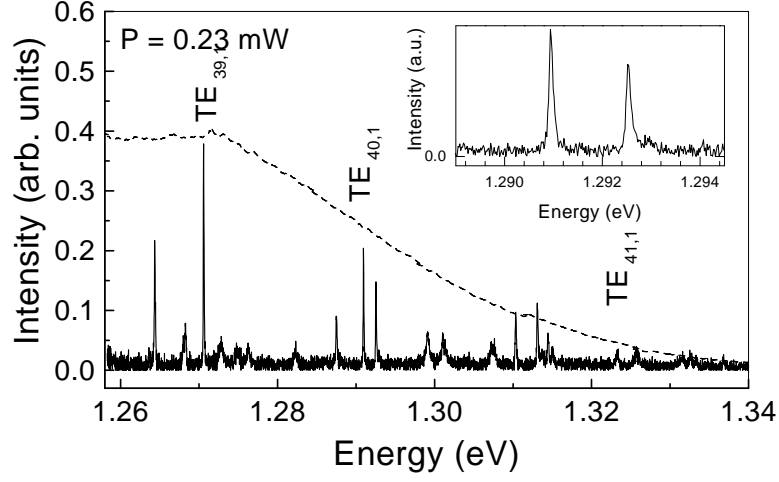


Figure 5.5: Photoluminescence spectrum of a $4.5 \mu\text{m}$ diameter microdisk having high density quantum dots embedded in the center plane. For comparison the PL spectrum of an unprocessed part of the wafer is also shown under similar excitation conditions. Inset: High resolution spectra of two WGMs.

center planes. By comparing these spectra to the photoluminescence spectrum of bulk region we can identify the whispering gallery modes. The change of mode separation with microdisk diameter is apparent from these figures. Our experiments revealed whispering gallery modes whose Q values were limited to our resolution of 18000 from $4.5 \mu\text{m}$ microdisks (Figure 5.5), while Q values as high as 9000 have been observed from $2 \mu\text{m}$ diameter microdisks (Figure 5.6). Laser operation was also observed for these high quality modes at 6 K [20].

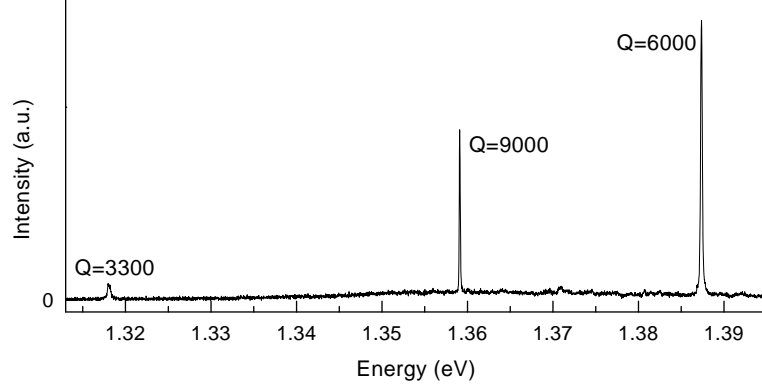


Figure 5.6: Photoluminescence spectrum of a $2\ \mu\text{m}$ diameter microdisk having high density quantum dots embedded in the center plane. High quality whispering gallery modes are visible.

5.3 Experimental Results

5.3.1 Demonstration of the Purcell Effect by Photon Correlation Experiments

Coupling between a single quantum dot single exciton transition and a microdisk whispering gallery mode is demonstrated in this section by both photoluminescence and second order photon correlation measurements. Indications of the Purcell effect as a result of the weak coupling cavity-QED regime will also be discussed. The specific quantum dot we chose for this analysis has the power dependent ($T = 4\ \text{K}$) photoluminescence spectra shown in Figure 5.7. As we will discuss later in the text, the small red detuning of the WGM emission from the single excitonic emission of the quantum dot is very convenient for this analysis. In the lowest excitation power, only one peak with resolution limited linewidth ($70\ \mu\text{eV}$) appears at an energy of $1.3219\ \text{eV}$. We identify that peak as the single excitonic transition of the quantum dot, this peak will be referred to as the X transition in the remaining

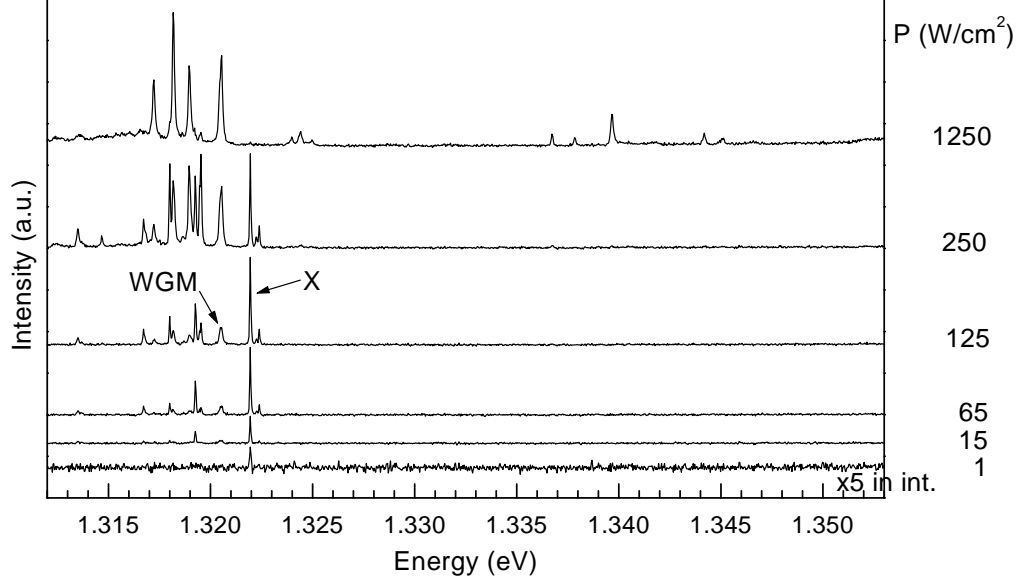


Figure 5.7: Power dependent photoluminescence spectra of a single quantum dot in microdisk cavity taken at 4 K under continuous wave excitation. Luminescence of the quantum dot single-exciton (X) transition, the whispering gallery mode (WGM), higher exciton lines and contributions of other WGMs are visible.

of this section. This identification is further supported by the results of the photon correlation measurements shown in Figure 5.9 that will be discussed later in the text. The peak at 1.3207 eV is identified as a whispering gallery mode (will be abbreviated as WGM) by its relatively large linewidth of $200 \mu\text{eV}$. The linewidth of the WGM corresponds to a Q value of 6500. The source of the WGM radiation at 4 K is not clearly identified, it might be caused by the residual emission from the GaAs disk, or by the emission from the quantum dot. There is an indication supporting the latter: In microdisk cavities that do not contain any quantum dots, we have not observed WGM emission in the quantum dot emission energies (1.25 eV-1.35 eV) even though we observed mode emission on the wetting layer luminescence (1.44 eV). The spec-

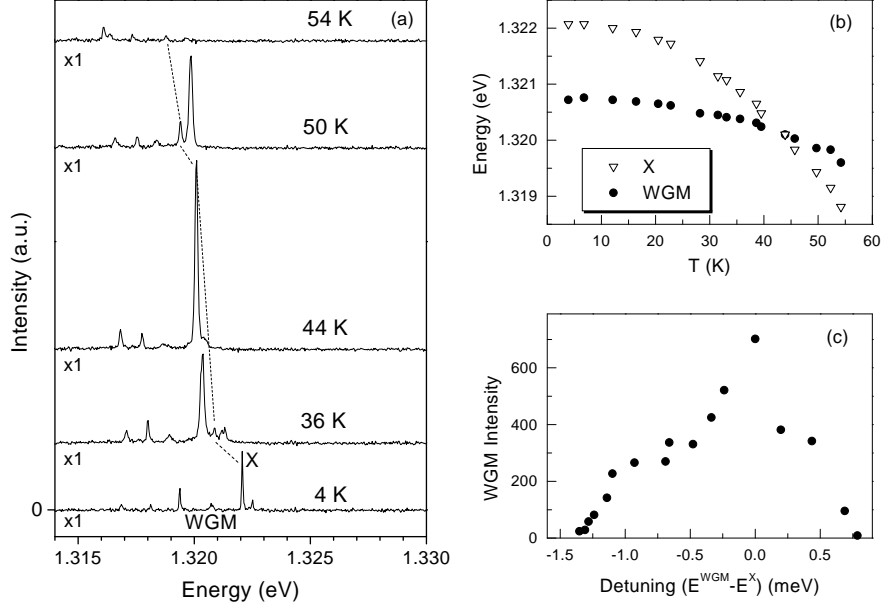


Figure 5.8: (a) Temperature dependent photoluminescence spectra taken under continuous wave excitation. X lines at various temperatures are connected as a guide for eye. (b) Change of the WGM and the X transition emission energy with temperature (excitation power = 15 W/cm²). (c) Change in the intensity of the WGM luminescence with X-WGM detuning (excitation power = 15 W/cm²).

trum with highest incident power in Figure 5.7 also helps the identification of WGMs. At that large pumping intensities we are able to saturate all the quantum dot transitions, and quantum dot lines become very broad (> 5 meV) making the WGMs visible. Temperature dependent characteristics plotted in Figure 5.8 together with the observed Purcell effect that is discussed later in this section provide additional evidence for the identification of the WGM.

The crossing between the X and WGM resonances is demonstrated in Figure 5.8. The WGM appears at an energy of 1.3207 eV at 4 K and shifts only slightly to an energy of 1.3196 eV at 54 K while the X transition shifts by over 3 meV within

50 K temperature difference (Figure 5.8(b)). The different energy shifts of the X transition and the WGM with temperature give rise to a crossing of the two resonances. The temperature dependence of the energy of the WGM can be attributed to the change in the refractive index of GaAs with temperature. On the other hand, the temperature dependence of the energy of the X transition is caused by the changes in the bandgaps of InAs and GaAs with temperature. Figure 5.8(c) shows the change in the intensity of the WGM emission as a function of the X-WGM detuning under the same excitation conditions. At a temperature of 44 K (zero detuning) the intensity of the WGM luminescence increases by a factor of 29 compared to its value at 4 K, strongly indicating a resonance between the X transition and the WGM. In resonance residual emission in the WGM is thus negligible (3%) compared to the emission due to the X transition.

As described in the previous sections, in the weak coupling cavity-QED regime, enhancement of the spontaneous emission rate of the quantum dot X transition due to the Purcell effect is expected. For our specific WGM Q is 6500, and effective mode volume is $V_{eff} = 30(\lambda/n)^3$ considering an effective mode area of $0.86\lambda^2(R/\lambda)^{3/2}$ (R denoting the radius of the microdisk) and thickness of $\sim 0.6(\lambda/n)$ [48]. Assuming an ideal spatial and polarization match between the WGM and X resonances, an ideal Purcell factor of $F_P = 16$ can be calculated using Equation 5.1.8. Considering the dipole orientation of the quantum dot being random in plane, together with the twofold degeneracy of the WGM, the total effective enhancement in the X transition's recombination rate becomes: $F_E = \frac{2}{2}F_P + 1 = 17$, while spatial mismatch between the quantum dot and WGM would result in a smaller value. In our case, the precise location of the quantum dot within the disk is not known, preventing us from determining the expected Purcell effect.

To quantify the magnitude of the Purcell effect we carried out pump power dependent photon correlation measurements under continuous wave excitation. As discussed in Chapter 3 this method is an alternative to standard time-resolved measurements for determining recombination times [26]. Figure 5.9(a) shows photon

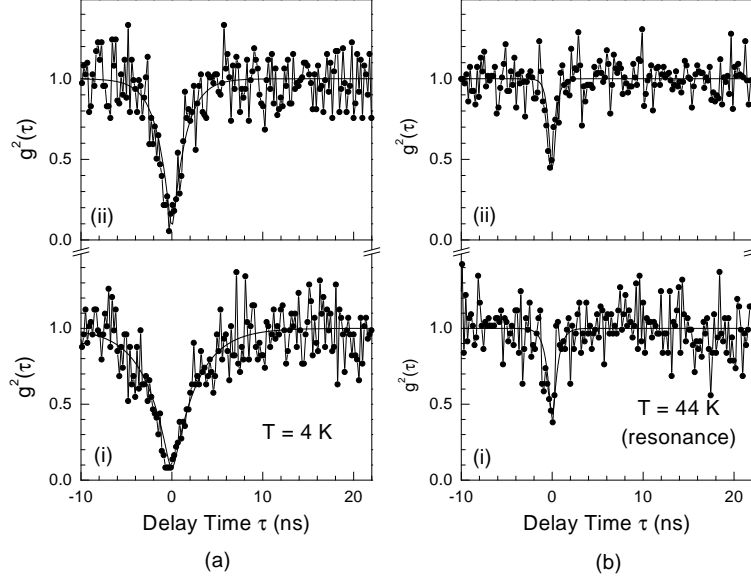


Figure 5.9: Measured photon correlation function of the X transition: (a) out of resonance with the WGM, at 4 K, under excitation powers of 35 W/cm² (trace (i)), and 90 W/cm² (trace (ii)); (b) in resonance with the WGM, at 44 K, under excitation powers of 5 W/cm² (trace (i)), and 45 W/cm² (trace (ii)).

correlation measurements at 4 K (out of resonance) at two different excitation intensities (traces (i) and (ii)), while photon correlation measurements performed at 44 K (in resonance) at two different excitation intensities are plotted in Figure 5.9(b) (traces (i) and (ii)). After normalization, the measured correlation functions show clear dips at zero time delay ($g^{(2)}(0) = 0.08$ in Figure 5.9(a) trace (i), $g^{(2)}(0) = 0.38$ in Figure 5.9(b) trace (i)) indicating strong photon antibunching. Since $g^{(2)}(0) < 0.5$ in our measurements, we can state that the observed emission lines are primarily due to the X transition of a single quantum dot [26]. Hence, in resonance, the X transition is the main emission feeding the WGM luminescence. We explain the value of $g^{(2)}(0)$ in Figure 2(b) being 0.38 instead of the ideal value of 0 by the short decay time (560 ps) which is comparable to the time resolution of the Hanbury Brown and

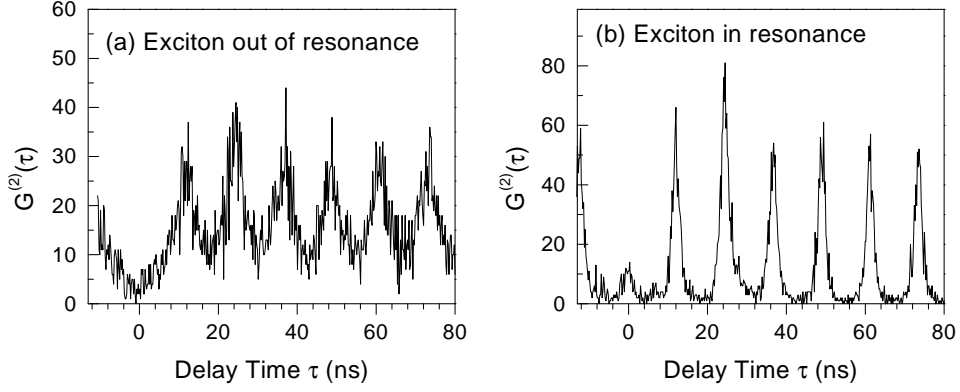


Figure 5.10: Measured unnormalized correlation function $G^{(2)}(\tau)$ of the X transition (a) out of resonance, and (b) in resonance with the WGM, under pulsed excitation conditions (82 MHz). The average pump intensity in both cases was $\sim 22 \text{ W/cm}^2$.

Twiss setup (420 ps).

From photon correlation measurements at 4 K decay times of 2.7 ns and 1.5 ns were observed at excitation levels below saturation (35 W/cm^2 , Figure 5.9(a) trace (i)) and at the onset of saturation (90 W/cm^2 , Figure 5.9(a) trace (ii)) of the X transition, respectively. Using the three-level rate-equation model discussed in Chapter 3, a lifetime of 3.4 ns is determined for the X transition at 4 K. This value is larger than previously reported lifetimes for the X transition of single InAs QDs ($\sim 1 \text{ ns}$). This lifetime difference is explained by the different photonic environment created by the microdisk that partially inhibits spontaneous emission, this phenomenon will be further explained in Section 5.5.

Our photon correlation measurements in resonance, 44 K, revealed decay times of 560 ps and 370 ps at pump powers of 5 W/cm^2 (Figure 5.9 (b) trace (i)), and 45 W/cm^2 (Figure 5.9 (b) trace (ii)) respectively, corresponding to excitation levels below the saturation of the X transition. By using the pump power dependent method, a lifetime of 590 ps is determined for the X transition at 44 K. Comparing

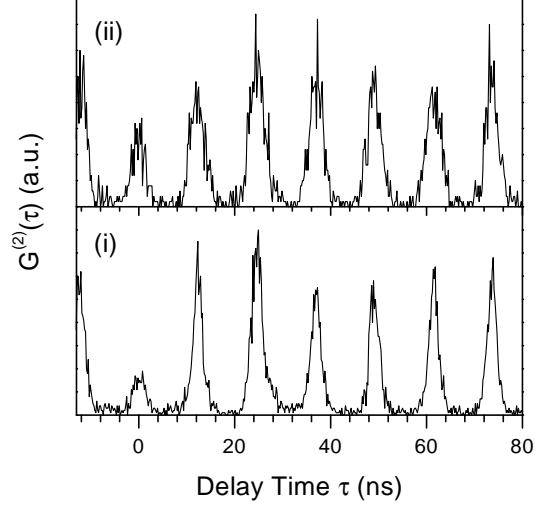


Figure 5.11: Measured unnormalized correlation function $G^{(2)}(\tau)$ of the X transition in resonance with the WGM, under pulsed excitation conditions (82 MHz) with average excitation intensities of 55 W/cm^2 (trace (i)), and 300 W/cm^2 (trace (ii))

the lifetimes in and out of resonance, and by assuming the effects of the nonradiative recombination to be negligible in both measurements, we deduce an enhancement in the spontaneous emission rate of the X transition by a factor of 6.

This value of 6 is also in agreement with the results of photon correlation measurements performed under pulsed excitation on this same quantum dot. These measurements are depicted in Figure 5.10. Under pulsed excitation the FWHM of the peaks is given by the total relaxation time of the quantum dot from the multi-excitonic state to the ground state. Hence the difference in the FWHM of the peaks in Figure 5.10 is due to the Purcell effect, and the ratio of the FWHMs at two temperatures provides a lower limit for Purcell effect which is 3.4 for our case [6].

A small peak at $\tau = 0$ is observed in the resonant case (see Figure 5.10(b)). The intensity ratio of this peak to the peaks at iT_{rep} is directly related to the fraction of pulses having two or more photons [40]. An experimental ratio $R = 0.29$ is

deduced from Figure 5.10(b). The fact that R is larger than the ideal value of zero could be due to the Purcell effect, which increases the probability of capturing a second electron-hole pair from the wetting layer after the X recombination process has occurred. Another possible explanation is the contribution from the background light generated by the residual emission from the GaAs disk and the wetting layer. Using higher average pump powers P in the resonant case increases R ($R = 0.36$ (0.55) for $P = 56$ (303) W/cm^2 , Figure 5.11), this observation is in agreement with both explanations.

5.3.2 Direct Proof of the Purcell Effect by TCPC Experiments

In this section we show the direct demonstration of the Purcell effect for a single quantum dot located in a microdisk cavity using the conventional time correlated single photon counting (will be denoted as TCPC) experiments. These experiments demonstrate an enhancement in the radiative recombination rate of a quantum dot due to weak coupling cavity-QED regime as well as proving that temperature tuning has no effect on the lifetime of the quantum dot X transition between 4 - 50 K.

Figure 5.12 shows the results of TCPC experiments performed on a single quantum dot X transition at 4 K and 50 K. The quantum dot used in these measurements is located in a $5 \mu\text{m}$ diameter microdisk cavity and the X transition is not coupled to any WGMs. These measurements were all performed in the low excitation regime where the decay time corresponds to the lifetime of the X transition [68]. Measured similar decay times of 1.7 ns at 4 K and 1.9 ns at 50 K show that when the X transition is not coupled to any WGMs its lifetime shows almost no dependence on temperature between 4 - 50 K. Hence, nonradiative recombination does not significantly affect the dynamics of the X transition within this temperature range. This result is in agreement with the temperature dependent lifetime measurements using high density quantum dot samples [69, 70, 71].

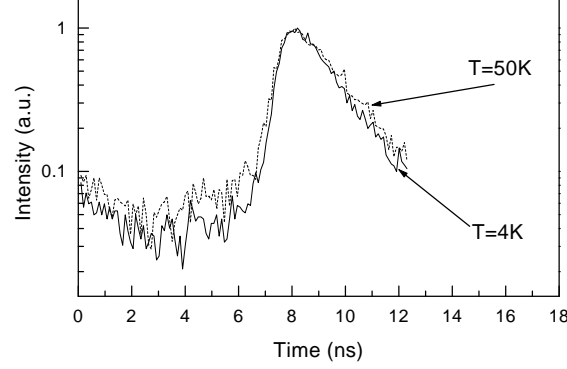


Figure 5.12: (a) Time correlated single photon counting measurements on the single-exciton (X) transition of a quantum dot at 4 K and 50 K, out of resonance with any WGMs.

In order to directly observe the Purcell effect, we performed TCPC experiments on the same quantum dot discussed in Section 5.3.1. The obtained photoluminescence spectrum and TCPC measurements are shown in Figure 5.13. We should note here that these TCPC measurements were performed about six months after the initial experiments reported in Section 5.3.1, and in the mean time we have observed changes both in quantum dot and mode properties. These changes will be explained in Section 5.4.

Figure 5.13(a) shows the photoluminescence spectrum of the quantum dot under pulsed excitation at 790 nm. At $T = 4$ K the resolution limited ($70 \mu\text{eV}$) peak at 1.3221 eV is identified as the single exciton recombination (X) line, whereas the emission at 1.3218 eV (WGM) is due to background emission that is coupled to a WGM. The linewidth of the WGM, $160 \mu\text{eV}$, corresponds to a Q value of 8300. We note that the source of the WGM radiation at 4 K might be caused by the emission from the quantum dot, or the residual emission from the GaAs. We achieved to tune the X and WGM emissions in resonance with each other by changing the sample

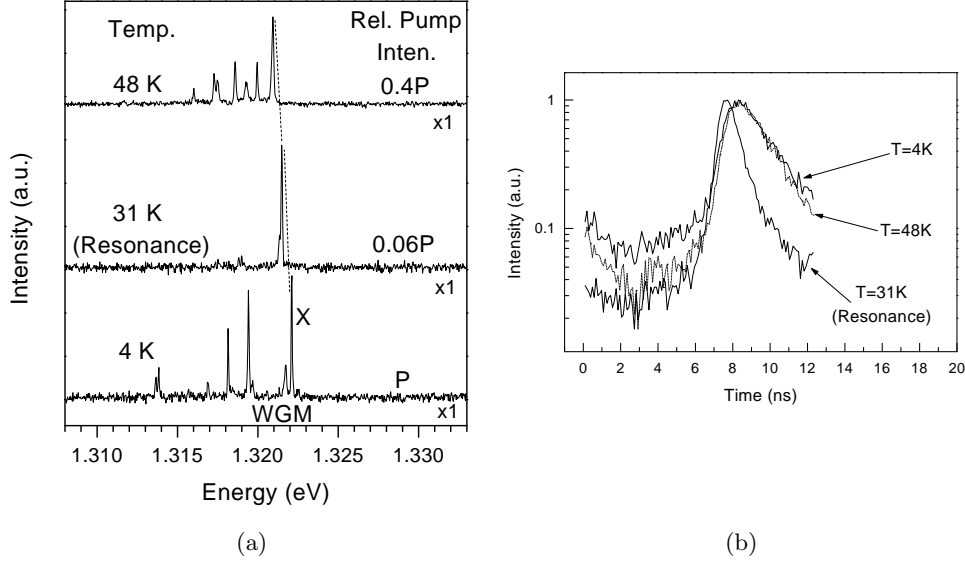


Figure 5.13: (a) Photoluminescence spectrum of a single InAs quantum dot, embedded in a $5\ \mu\text{m}$ diameter microdisk, taken under nonresonant pulsed excitation at 4 K, 31 K, and 48 K. Resonance between the excitonic ground state transition (X), and a whispering gallery mode (WGM) is visible at 31 K. (b) Time correlated single photon counting measurements on the single-exciton (X) emission: out of resonance with the WGM (4 K, 48 K), in resonance with the WGM (31 K). Relative pump intensities were P, 0.06P, and 0.4P at 4 K, 31 K, and 48 K respectively.

temperature to 31 K. Photoluminescence spectra taken at 31 K, and 48 K are also shown in Figure 5.13(a). Since those spectra were taken under nonresonant pulsed excitation conditions, at 31 K the resonant enhancement in the spontaneous emission rate does not increase the WGM intensity.

Figure 5.13(b) demonstrates TCPC experiments at three different temperatures taken under low excitation conditions where the biexciton emission or emission from the higher excited states were not observed. These measurements revealed identical decay times of 1.8 ns at 4 K and 48 K showing that when the X transition is not coupled to any WGMs its lifetime has no dependence on temperature between 4 - 48 K. Hence, nonradiative recombination does not significantly effect the dynamics

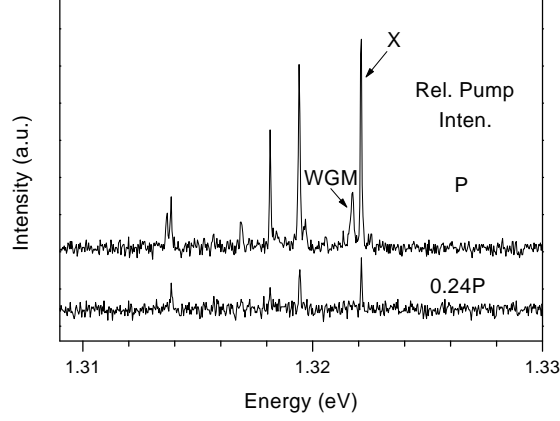


Figure 5.14: Photoluminescence spectra taken under nonresonant pulsed excitation for relative pump intensities 0.24P, and P at 4 K. The decrease in the background coupling to the WGM is apparent.

of the X transition within this temperature range. When the X emission is in resonance with the WGM at 31 K, the decay time is reduced to 850 ps, leading to the observation of a Purcell factor of at least 2. The measurement at 31 K was performed under low-excitation conditions (0.06P, Figure 5.13(a)) where the background had negligible coupling to the WGM. The negligible coupling of background to the WGM radiation is also observable in Figure 5.14 where we plot the photoluminescence spectra for two different pump power intensities at 4 K.

We note here that the electron-hole pairs in the wetting layer have average recombination times of ~ 300 ps [52] or larger depending on the existence and nature of trap states. For our low density quantum dot samples, we measured lifetimes as long as 800 ps - 1 ns on the low energy side of the wetting layer luminescence using the TCPC technique. Hence, the measured decay time in our case may be limited by the lifetime of the wetting layer states that pump the quantum dot. For our specific WGM ($Q=8300$, $V_{Eff} = 30(\lambda/n)^3$), an ideal Purcell effect of $F_P = 22$ is estimated

assuming an ideal spatial match between the quantum dot and WGM.

5.4 Spectral Changes in the Quantum Dot and WGM Emissions

Despite the fact that data displayed in Figures 5.9, and 5.13 are taken from the same quantum, there are differences in the deduced lifetimes and Purcell effects from these measurements. When the single excitonic transition is out of resonance with any WGMs, single exciton lifetimes of 3.4 ns and 1.8 ns are deduced from the measurements in Figures 5.9 and 5.13 respectively. Similarly, measurements in Figures 5.9 and 5.13 reveal Purcell effects of 6 and 2 respectively. Hence between these two set of measurements there is a substantial drift in quantum dot properties and in the coupling between the WGM and the quantum dot. In this section we discuss the changes in the quantum dot and mode properties during the six months time interval between the two set of measurements shown in Figures 5.9 and 5.13 in order to explain our results.

The change in the spectrum of this quantum dot with time and excitation conditions is demonstrated by the emission spectra in Figure 5.15(a) measured under very low excitation conditions wher biexcitonic emission is not observed. In trace (ii), the existence of a second peak suggests a charged excitonic emission from this quantum dot. It is probable that by highly exciting this quantum dot we have activated a trap state that caused the charged excitonic emission. The number of charged excitonic emission lines also changed with the excitation energy as seen in trace (iii). Under 760 nm and 785 nm continuous wave excitation, 1 and 2 additional charged excitonic emission lines are observed respectively. Such dependencies of the emission spectrum to nonresonant excitation energy are known for our samples [72]. This phenomenon can provide an explanation to why we observed a factor of ~ 2 (3.4 ns observed in Section 5.3.1 vs. 1.8 ns in Section 5.3.2) difference in the lifetime of the X transition located at 1.3221 eV between the two set of measurements. For

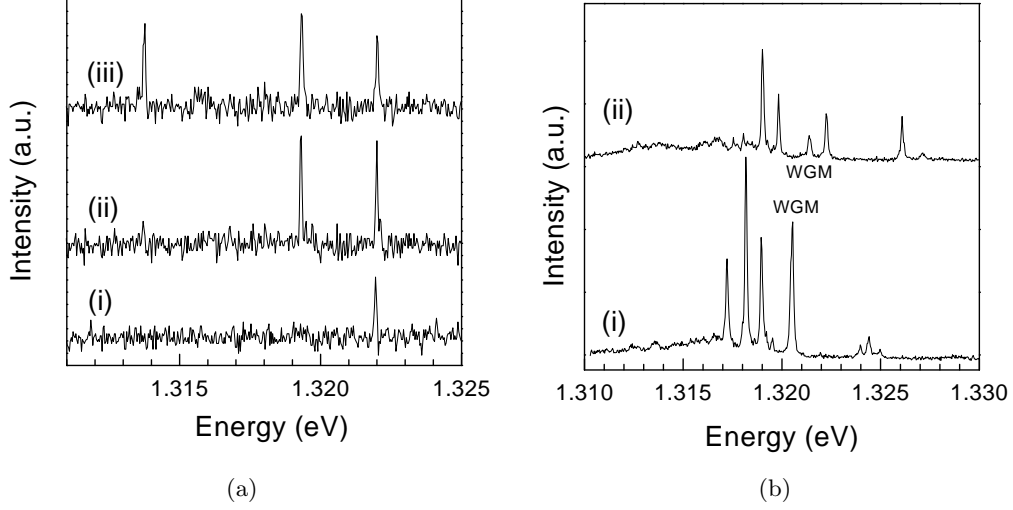


Figure 5.15: (a) Photoluminescence spectra obtained from the same quantum dot in summer 2000 under cw excitation at 750 nm (trace (i)), in summer 2001 under cw excitation at 760 nm (trace(ii)) and 785 nm (trace(iii)) (b) Drift of mode emission properties between summer 2000 (trace (i)) and january 2001 (trace(ii)), the whispering gallery modes coupled to single exciton emission is denoted by WGM in both cases.

the experiment reported in Section 5.3.2 (corresponding to Figure 5.15(a) trace(ii)), the additional charge, which is probably an additional hole for this quantum dot (this is discussed in Chapter 6, and [73]), may increase the overlap integral between the other electron and hole in the ground state, causing an enhancement in spontaneous emission rate. In contrast, the experiment reported in Section 5.3.1 (corresponding to Figure 5.15(a) trace(i)) is performed in the absence of an additional charge in the quantum dot.

Even though the change in the quantum dot emission spectrum explains the change in the observed lifetime values, it does not explain the change in the observed Purcell effect between the two set of experiments. This discrepancy can be explained by the drift in the WGM properties as depicted in Figure 5.15(b). Degradation in the

cavity properties, oxidation in the surface, dust particles would effect the resonance emission wavelengths by small amounts that are enough to considerably drift the mode properties. In Figure 5.15(b) two photoluminescence spectra are plotted at very high excitation regime. At this regime, the quantum dot emission becomes very broad and all the WGMs coupled to that quantum dot through a broad emission spectrum become visible. From that figure it can be seen that the mode at 1.3207 eV at trace (ii) is not necessarily the same mode as the one in 1.3218 eV in trace (i), hence different observed Purcell effects in both situations are expected.

5.5 Inhibited Spontaneous Emission due to Microdisk Cavities

As presented in Chapters 3 - 5, we have consistently observed single excitonic transition lifetimes in the range of 2 - 4 ns from single InAs quantum dots located in microdisk cavities. In contrast, we measured lifetimes of 900 ps for single quantum dots located in bulk samples in agreement with the literature [33]. In this section we intend to bring an explanation to this observation by the inhibited spontaneous emission phenomenon.

5.5.1 Inhibited Spontaneous Emission Phenomenon

Together with the cavity induced enhancement in spontaneous emission due to the Purcell effect, inhibited spontaneous emission (first suggested in 1981 [74]) complements the topic of modified spontaneous emission. In the Fermi-Golden rule regime where the cavity broadening is much larger than the dipole broadening, spontaneous emission rate is given by:

$$\frac{1}{\tau} = \frac{2\pi}{\hbar^2} \rho(\omega) E_{max}^2 \langle |\mu_{eg} \cdot \epsilon|^2 \rangle \quad (5.5.1)$$

In this equation the available optical mode density ($\rho(\omega)$), and zero point field fluctuations (E_{max}) together with the field polarization vector (ϵ) constitute the *photonic*

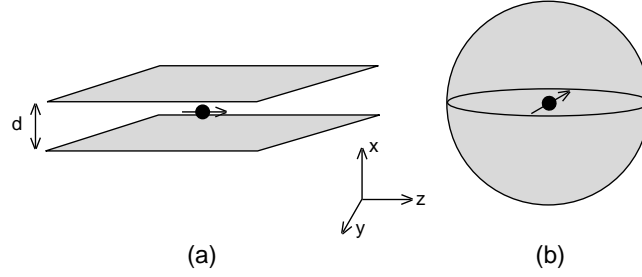


Figure 5.16: (a) Dipole located in the center of two perfect conductor plates (b) Dielectric sphere

environment, and they can be modified independently from the specific dipole emitter. As we analyzed in Section 5.1, resonant coupling of a dipole to a high Q, low volume cavity mode results in the enhancement of its spontaneous emission rate. Similarly the photonic environment $(\rho(\omega), E_{max}, \epsilon)$ can be modified to achieve inhibition in spontaneous emission. This effect can be obtained in various ways, and can be very powerful both for atoms and solid-state devices [75]. Let us first introduce two textbook cases to emphasize how drastic inhibitions can be achieved in spontaneous emission rates. Thereafter we will discuss the spontaneous emission of a single quantum dot located in a microdisk cavity.

i. *Dipole Between Two Conducting Planes:*

For a dipole placed to the middle of two parallel conductors (Figure 5.16(a)), imposing the perfect conductor boundary conditions, the mode density for the electric field parallel to the surface of the conducting plates (z-direction in Figure 5.16(a)) can be found to be zero for $k < \frac{\pi}{d}, \lambda > \frac{d}{2}$. Hence it is possible to make the available optical mode density zero by having plates separation $d < \frac{\lambda}{2}$ for a z-oriented dipole. In that case no spontaneous emission is allowed. Such experiments have been achieved using atoms [76, 77], giving inhibitions in spontaneous emission rates by factors ~ 20 .

ii. *Dielectric Sphere:*

The general solution of this problem can be found in Ref. [78]. For disk radius much smaller than the wavelength ($r \ll \lambda$) the value of inhibition in the spontaneous emission can be estimated by assuming the static limit having the electrostatic boundary conditions [79]:

$$\mathbf{E}_{in} = \frac{3}{\left(\frac{n_{in}}{n_{out}}\right)^2 + 2} \mathbf{E}_{out}$$

Due to the spherical symmetry of the problem, for an arbitrary dipole orientation μ_{eg} Equation 5.5.1 becomes:

$$\begin{aligned} \frac{1}{\tau_{sphere}} &= \frac{2\pi}{\hbar^2} \rho(\omega) \left(\frac{3}{\left(\frac{n_{in}}{n_{out}}\right)^2 + 2} E_{out} \right)^2 \langle |\langle \mu_{eg} \cdot \epsilon \rangle|^2 \rangle \\ \rho(\omega) = \rho_{vac}(\omega) &= \frac{\omega^2 V_{eff} n_{out}^3}{\pi^2 c^3}, E_{out} = \sqrt{\frac{\hbar \omega}{2\epsilon_0 n_{out}^2 V_{eff}}} \\ \Rightarrow \frac{1}{\tau_{sphere}} &= \left(\frac{3}{\left(\frac{n_{in}}{n_{out}}\right)^2 + 2} \right)^2 \frac{\omega^3 n_{out}}{3\pi\epsilon_0 \hbar c^3} |\mu_{eg}|^2 \end{aligned}$$

Comparing this value with the spontaneous emission rate in a uniform dielectric with refractive index n_{in} :

$$\frac{1}{\tau_{uni}} = \frac{\omega^3 n_{in}}{3\pi\epsilon_0 \hbar c^3} |\mu_{eg}|^2$$

an inhibition in spontaneous emission is deduced by a factor [75]:

$$F_I = \frac{1/\tau_{uni}}{1/\tau_{sphere}} = \left(\frac{\left(\frac{n_{in}}{n_{out}}\right)^2 + 2}{3} \right)^2 \frac{n_{in}}{n_{out}}$$

For the case of a GaAs ($n_{GaAs} = 3.5$) sphere in the air, this ratio is $F_I = 79$ which indicates that large inhibitions in spontaneous emission can be achieved in solid-state systems [75].

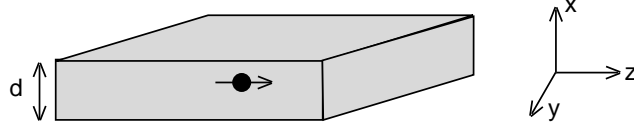


Figure 5.17: Slab waveguide

5.5.2 Analysis of Inhibited Spontaneous Emission in a Microdisk Cavity

Unfortunately inhibited spontaneous emission in microdisk cavities is not a problem which can be solved analytically as the problems in the previous section. Exact solution of this problem requires numerical methods. However it is possible to discuss some general intuitive reasons which give an order of magnitude approximation to the actual value of inhibition of the spontaneous emission rate.

The 200 nm thickness of our microdisk cavities is smaller than the material wavelength (925 nm/3.4=264 nm). Intuitively, because of this small thickness alone, inhibited spontaneous emission is expected similar to two conducting plates problem. Considering a slab waveguide as in Figure 5.17, when the thickness $d < \frac{\lambda}{2n}$ a z-oriented dipole is not coupled to any of the guided modes of the slab waveguide, only radiative tunnelling modes can be considered. Assuming dipole orientation to be in plane (z direction in Figure 5.17) only z-component of the vacuum field is used for the spontaneous emission rate calculation. Again making the static approximation as in the case of the dielectric sphere, in the electrostatic boundary conditions $E_{z,in} = E_{z,out}$ which implies that the spontaneous emission of the dipole is:

$$\frac{1}{\tau_{slab}} = \frac{\omega^3 n_{out}}{3\pi\epsilon_0 \hbar c^3} |\mu_{eg}|^2$$

Instead of:

$$\frac{1}{\tau_{uni}} = \frac{\omega^3 n_{in}}{3\pi\epsilon_0 \hbar c^3} |\mu_{eg}|^2$$

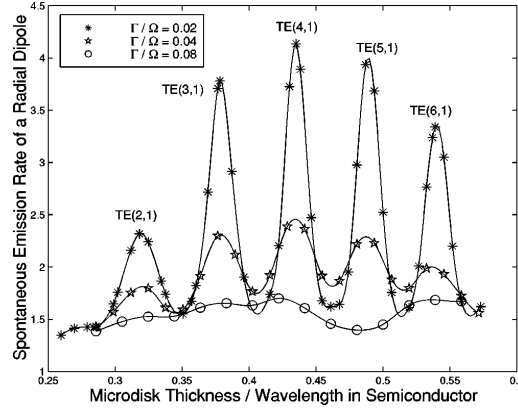


Figure 5.18: Finite Difference Time Domain calculations done on a microdisk, considering a radial dipole (taken with permission from Phys. Rev. A, **61**, 033808 (2000)).

Hence spontaneous emission is inhibited by a factor $F_I = \frac{n_{in}}{n_{out}}$ [80]. This factor is 3.5 for a GaAs slab waveguide located in the air. This factor does not exactly apply to our microdisk cavity problem because our microdisks' thickness (200 nm) is larger than half wavelength ($\frac{\lambda}{2n} = 132 \text{ nm}$), and microdisk cavity has whispering gallery modes instead of the guided modes of a slab waveguide. However the order of magnitude for the inhibition in the spontaneous emission can be intuitively expected to be similar to 3.5.

Whispering gallery modes of a microdisk cavity also contribute to inhibited spontaneous emission. In contrast to the enhancement of spontaneous emission rate of a dipole resonantly coupled to a whispering gallery mode, when the dipole is not in resonance with any whispering gallery modes, the available optical mode density ($\rho(\omega)$) is reduced resulting in the inhibition of spontaneous emission rate of the dipole. Such an effect has been observed using atoms placed in Fabry-Perot cavities [81, 82]. Inhibition factors of 0.5 %, and ~ 5 % were reported in those results when the cavity resonance was detuned from the two-level transition.

As we noted in the beginning of this subsection, the exact amount of inhibi-

tion in spontaneous emission rate of a dipole located in a microdisk cavity can be calculated using numerical techniques [83, 84]. Finite-difference time-domain (FDTD) analysis is done for such an exact solution. Figure 4 in Ref. [83] demonstrates an example of enhancement and inhibition of spontaneous emission rate depending on whether the quantum dot is in and out of resonance with whispering gallery modes (Figure 5.18). Inhibition of spontaneous emission due to the whispering gallery modes can also be seen in Figure 6 in Ref. [84]. In this plot spontaneous emission of a dipole placed in a slab waveguide and microdisk cavity of same thicknesses are plotted. For thicknesses when the dipole is out of resonance with whispering gallery modes, the spontaneous emission rate in the microdisk cavity is smaller than the spontaneous emission of the dipole in the slab waveguide due to the cavity-caused inhibition in spontaneous emission.

We would like to emphasize that the variety of inhibition values we observed in spontaneous emission rate of single quantum dots located in microdisk cavities (2 - 4 ns) is probably due to different locations of quantum dots in those cavities. Depending on whether a quantum dot is close to the edge of the microdisk or not, inhibition of spontaneous emission rate becomes larger or smaller respectively. Finally we note that inhibited spontaneous emission similar to our results have been observed in single Nitrogen-vacancy color centers [85]. When placed in a solution of polymer as nanocrystals ($n \approx 1$), their spontaneous emission has been found to be ~ 2.5 times smaller than the bulk diamond ($n = 2.4$) case.

Chapter 6

Photon Correlation Spectroscopy

Even though the coherence properties of quantum dot single exciton emission closely follow those of atoms, the overall spectral features of single quantum dots are significantly more complicated. Since the size of quantum dots is roughly two-orders of magnitude larger than those of atoms, multi-particle excitations give rise to emission peaks with energies comparable to that of a single exciton. Of primary importance in quantum dot spectroscopy is the biexciton state, which corresponds to a doubly-excited quantum dot with completely filled lowest electron and hole energy levels. When the biexciton state decays by radiative recombination, the final-state is a single exciton state and the generated photon is shifted as compared to the single exciton emission due to Coulomb interaction between the carriers. Biexciton emission in quantum dot spectroscopy has been traditionally identified using the (quadratic) pump-power dependence of the corresponding peak.

In this chapter, we demonstrate that photon correlation measurements provide a powerful tool for characterizing the multiexciton spectral features of quantum dots. Our measurements provide a strong support for the identification of a biexciton

emission peak, by demonstrating its strong correlations with the subsequent single exciton emission [86]. We observe that biexciton intensity autocorrelation exhibits bunching together with antibunching or only antibunching under continuous-wave excitation depending on the excitation level. In contrast, we find strong antibunching under pulsed excitation. The large difference between the levels of antibunching under continuous-wave and pulsed excitations points out to the importance of excitation mechanism and the role of free carriers in quantum dot physics. The lack of polarization correlation between biexciton and single exciton emissions indicates that spin dephasing is likely to play a key role under non-resonant excitation. We also observe that a third emission peak in quantum dot spectra exhibits strong correlations with both exciton and biexciton fluorescence: we argue that these correlation signatures suggest the identification of this additional line as a charged-exciton emission.

6.1 Analysis of a Three-Level System for Cross-Correlation Measurements

In Chapter 3.2 auto-correlation properties of the single exciton emission of a quantum dot were analyzed using a *cascaded* three-level model revealing the photon antibunching phenomenon. It is also possible to analyze all other possible correlations in such a cascaded three-level system. In this section we make this analysis using rate equations in the large dephasing limit. This is aimed to be the analytical introduction to the experimental results discussed in the remainder of the chapter. Such an analysis considering different three-level system configurations including the cascaded configuration is done in Ref. [87].

For a cascaded three-level system as in Figure 6.1, apart from the single excitonic auto-correlation function calculated in Section 3.4, there are three other correlation functions to be calculated. In their unnormalized forms these second order photon correlation functions are:

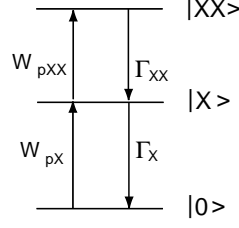


Figure 6.1: Three-level system

i. Biexciton auto-correlation function:

$$\begin{aligned}
 G_{XX,XX}^{(2)}(\tau) &= \langle \sigma_{XX,X}(t') \sigma_{XX,X}(t' + \tau) \sigma_{XX,X}(t' + \tau) \sigma_{XX,X}(t') \rangle \\
 &= \langle \sigma_{XX,X}(t') \sigma_{XX,XX}(t' + \tau) \sigma_{XX,X}(t') \rangle
 \end{aligned}$$

ii. Biexciton-Exciton cross-correlation function:

$$\begin{aligned}
 G_{XX,0X}^{(2)}(\tau) &= \langle \sigma_{XX,X}(t') \sigma_{X,0X}(t' + \tau) \sigma_{0X,X}(t' + \tau) \sigma_{XX,X}(t') \rangle \\
 &= \langle \sigma_{XX,X}(t') \sigma_{X,X}(t' + \tau) \sigma_{XX,X}(t') \rangle
 \end{aligned}$$

iii. Exciton-Biexciton cross-correlation function:

$$\begin{aligned}
 G_{0X,XX}^{(2)}(\tau) &= \langle \sigma_{X,0X}(t') \sigma_{XX,X}(t' + \tau) \sigma_{XX,X}(t' + \tau) \sigma_{0X,X}(t') \rangle \\
 &= \langle \sigma_{X,0X}(t') \sigma_{XX,XX}(t' + \tau) \sigma_{0X,X}(t') \rangle
 \end{aligned}$$

Following exactly the same steps as in Section 3.4, in the large dephasing limit, these second-order correlation functions can be calculated by using the rate equations, and the quantum regression theorem. Specifically, the following rate equations and initial conditions are used for the solution of the three cases:

i.

$$\frac{d}{d\tau} \begin{bmatrix} G_{XX,XX}^{(2)}(\tau) \\ F_i(\tau) \\ H_i(\tau) \end{bmatrix} = \begin{bmatrix} 0 & W_{pXX} & -\Gamma_{XX} \\ W_{pX} & -(W_{pXX} + \Gamma_X) & \Gamma_{XX} \\ -W_{pX} & \Gamma_X & 0 \end{bmatrix} \begin{bmatrix} F_i(\tau) \\ G_{XX,X}^{(2)}(\tau) \\ H_i(\tau) \end{bmatrix}$$

$$\begin{aligned}
G_{XX,XX}^{(2)}(\tau=0) &= 0 \\
F_i(\tau=0) &= \langle \sigma_{XX,XX}(t') \rangle \\
H_i(\tau=0) &= 0
\end{aligned}$$

ii.

$$\frac{d}{d\tau} \begin{bmatrix} F_{ii}(\tau) \\ G_{XX,0X}^{(2)}(\tau) \\ H_{ii}(\tau) \end{bmatrix} = \begin{bmatrix} 0 & W_{pXX} & -\Gamma_{XX} \\ W_{pX} & -(W_{pXX} + \Gamma_X) & \Gamma_{XX} \\ -W_{pX} & \Gamma_X & 0 \end{bmatrix} \begin{bmatrix} F_{ii}(\tau) \\ G_{XX,0X}^{(2)}(\tau) \\ H_{ii}(\tau) \end{bmatrix}$$

$$\begin{aligned}
F_{ii}(\tau=0) &= 0 \\
G_{XX,0X}^{(2)}(\tau=0) &= \langle \sigma_{XX,XX}(t') \rangle \\
H_{ii}(\tau=0) &= 0
\end{aligned}$$

iii.

$$\frac{d}{d\tau} \begin{bmatrix} G_{0X,XX}^{(2)}(\tau) \\ F_{iii}(\tau) \\ H_{iii}(\tau) \end{bmatrix} = \begin{bmatrix} 0 & W_{pXX} & -\Gamma_{XX} \\ W_{pX} & -(W_{pXX} + \Gamma_X) & \Gamma_{XX} \\ -W_{pX} & \Gamma_X & 0 \end{bmatrix} \begin{bmatrix} G_{0X,XX}^{(2)}(\tau) \\ F_{iii}(\tau) \\ H_{iii}(\tau) \end{bmatrix}$$

$$\begin{aligned}
G_{0X,XX}^{(2)}(\tau=0) &= 0 \\
F_{iii}(\tau=0) &= 0 \\
H_{iii}(\tau=0) &= \langle \sigma_{X,X}(t') \rangle
\end{aligned}$$

Solutions for all three cases are depicted in Figure 6.2 for two separate power levels, assuming $\Gamma_{XX} = 2\Gamma_X$, and $W_{pXX} = 2W_{pX}$. Photon antibunching together with bunching signatures are visible in those figures. Intuitive explanations can be readily made for those results. In Figure 6.2(a) antibunching is observed because detection of a biexcitonic photon necessarily projects the system to the single excitonic level hence prevents the immediate detection of another biexcitonic photon. Furthermore, at lower power levels the information that the system is at the single excitonic level enhances the probability of detection of a consecutive biexcitonic photon, resulting in the bunching behavior in Figure 6.2(a) trace (i). Similarly, in Figure 6.2(b) detection of a biexcitonic photon projects the system to the single excitonic level,

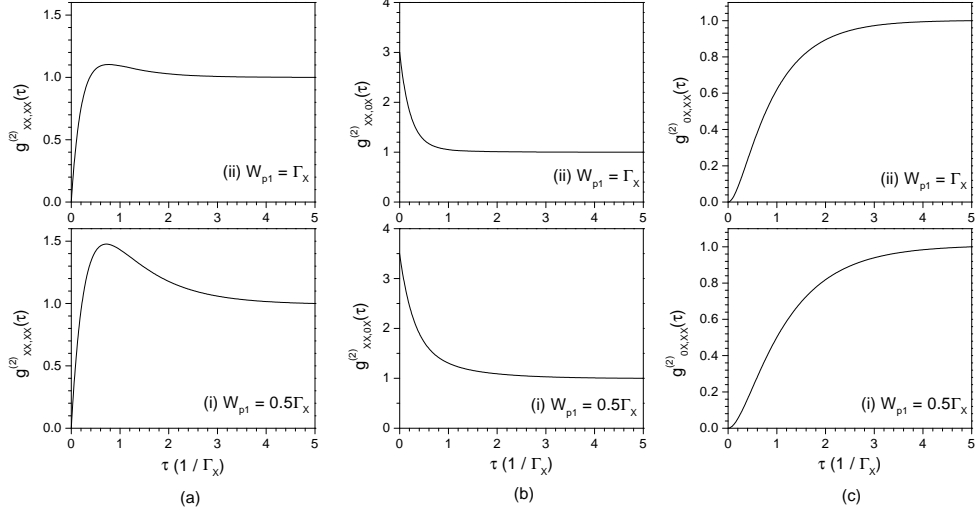


Figure 6.2: Solution of the three second order photon correlation functions ((a) $g_{XX,XX}^{(2)}(\tau)$, (b) $g_{XX,0X}^{(2)}(\tau)$, (c) $g_{0X,XX}^{(2)}(\tau)$) in a cascaded three-level system for pump powers $W_{p1} = 0.5\Gamma_X, \Gamma_X$, assuming $\Gamma_{XX} = 2\Gamma_X$, and $W_{pXX} = 2W_{pX}$.

enhancing the probability of a consecutive single excitonic photon emission, hence bunching is observed. Furthermore, as the pumping power is lowered, the bunching effect is increased because while the average number of excitons in the quantum dot decreases with decreasing pumping power, the detection of a biexcitonic photon always necessarily projects the system to the single excitonic level. Figure 6.2(c) depicts the probability of detection of a biexcitonic photon at time τ given that a single excitonic photon has been detected at $\tau = 0$. Antibunching is observed in this case because at $\tau = 0$ the system is necessarily at the ground level. An average time that is equal to the average recovery time of the system from the ground level to the two-excitonic level has to elapse until a consecutive biexcitonic photon emission, thus resulting in photon antibunching.

6.2 Photon Correlation Spectroscopy Experiments using single Quantum Dots

In this section experimental results proving the cascaded biexciton and single exciton emissions of a single quantum dot are presented. As well as providing a striking agreement with the analysis in Section 6.1, these results are used to identify several transitions in the emission spectrum of a single quantum dot as a spectroscopic tool. Before starting with the discussion of our experimental results, we note that coincidence detection measurements similar to our experiments have been performed using cascaded transitions in atoms where many atoms were used as the emission source. We will discuss those experiments and compare them with our experimental results in Section 6.3.

Figure 6.3(a) shows the power dependent photoluminescence spectra of the single quantum dot that we analyze. At low pump powers, the single excitonic emission peak (X1) dominates the spectrum. At higher pump powers, we observe that two other peaks become dominant: among these, the lower energy one (XX) has an energy (red) shift of 3.5 meV from X1 and its intensity has a quadratic dependence on pump power; these are typical signatures for biexciton emission in self-assembled InAs quantum dots. The third peak (X2) is red-shifted from the single excitonic peak by about 500 μeV . All three emission peaks are resolution limited at 70 μeV , and none of them is polarized. To ensure that X1 originates from a single quantum dot exciton emission, we have carried out photon auto-correlation measurements where both APDs were illuminated by X1: under continuous wave and pulsed excitation, X1 emission was found to exhibit perfect antibunching (Figure 6.3(b)) and single-photon source operation (Figure 6.3(c)). We have also performed time correlated single photon counting experiments on X1, X2, and XX emissions to measure their lifetimes. Those measurements were performed in the very low excitation regime where the decay times of the resulting spectra were determined by the lifetimes of the corresponding emissions (Chapter 3.2, [88]). From the measured spectra we deduced

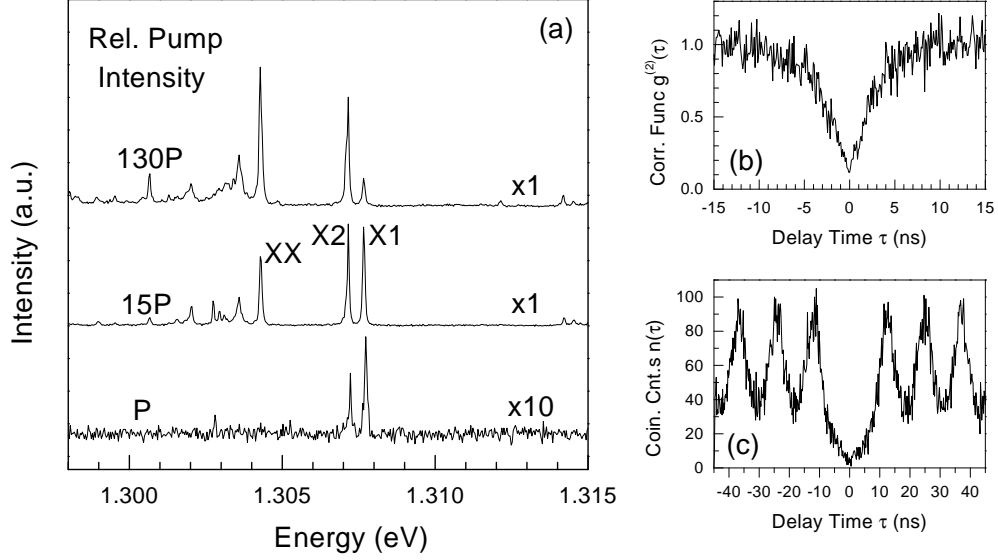


Figure 6.3: (a) PL spectra for the quantum dot studied in this letter for various powers of the continuous wave diode laser at 785 nm. Indicated are the three peaks that we focus on. With increasing powers, the dominant line is successively X1, then X2, then XX. All lines saturate and then decrease with increasing power. Photon correlation measurements carried out using the X1 emission, under continuous wave (b) and pulsed (c) excitations.

lifetimes of 3.6 ns, 3.7 ns and 2.6 ns for the X1, X2, and XX emissions respectively (Figure 6.4). The resultant ratio of $\tau_{X1}/\tau_{XX} = 1.4$ is consistent with exciton and biexciton lifetime measurements performed on CdSe/ZnSe quantum dots [68]. We also note that, due to the different photonic environment created by the microdisk, the single exciton lifetime we observe (3.6 ns) is larger than typical lifetimes measured (~ 1 ns) in bulk quantum dot samples (Chapter 5).

Figures 6.5(a) and 6.5(b) show $g^{(2)}(\tau)$ for the XX emission under continuous wave excitation, at pump powers corresponding to X1 emission intensities that are 0.7 and 1.0 of the (exciton) saturation level, respectively. Both curves, obtained using a

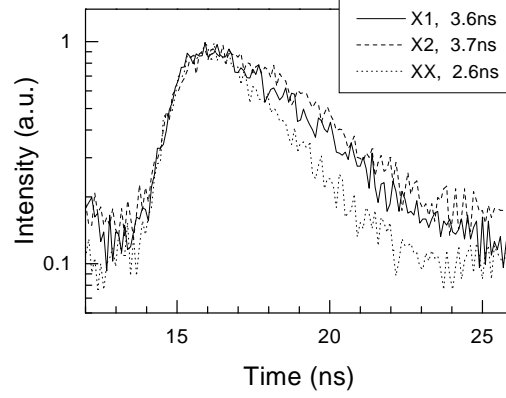


Figure 6.4: Time-correlated-single-photon-counting measurements on X1, X2, and XX emission lines

0.5 nm interference filter, exhibit antibunching ($g^{(2)}(0) = 0.95$ in Figure 6.5(a) trace (i), $g^{(2)}(0) = 0.6$ in Figure 6.5(a) trace (ii)) with similar decay times of 1 ns. The curve in Figure 6.5(a) trace (i) also exhibits bunching ($g^{(2)} = 1.4$) that decays with a decay time of 3.5 ns. Bunching here originates from the fact that the detection of a photon at the biexciton transition results in the projection of the quantum dot wave-function onto the single exciton state X1. When the average occupancy of X1 in steady-state is lower than unity, post-measurement-state has higher occupancy in the single exciton state than pre-measurement-state, and is more likely to result in re-excitation of the biexciton state. The analysis of the quantum dot dynamics using three-level rate equations (Section 6.1) indicates that $g^{(2)}(\tau)$ should indeed exhibit bunching that decays in a timescale determined by the single exciton lifetime of 3.6 ns which is in agreement with the experimental result (Figure 6.5(a)). This analysis also predicts that antibunching at $\tau = 0$ should turn into bunching in a timescale determined by the biexciton lifetime in the low excitation regime.

When we replace the 0.5 nm interference filter by a 1 nm filter, we cannot observe antibunching in biexciton auto-correlation measurements, even though strong

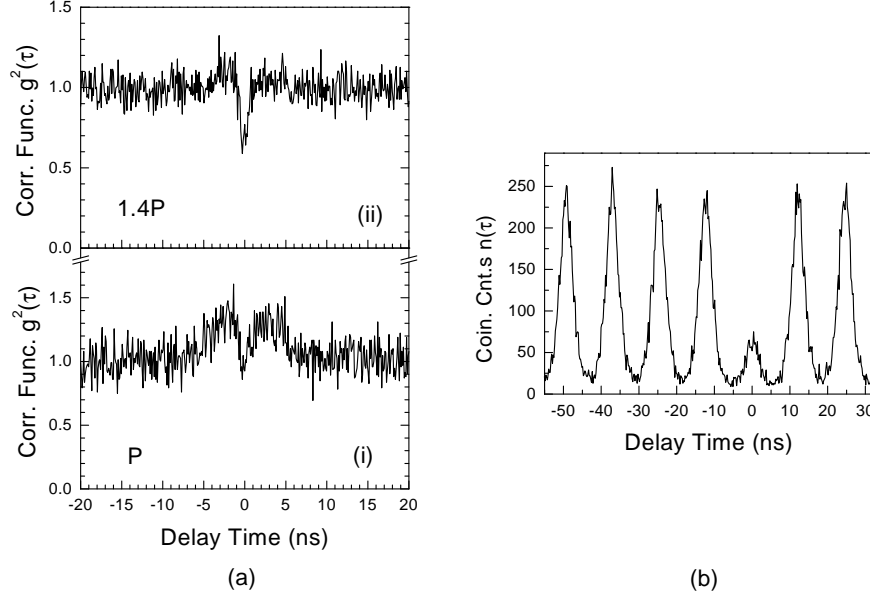


Figure 6.5: Photon correlation measurements carried out using the XX emission, under cw (a) (Pump power P (trace (i)), and $1.4 P$ (trace (ii))) and pulsed (b) excitations.

bunching feature around $\tau = 0$ persists. This finding highlights the importance of broadband background radiation at biexciton energy. The fact that we continue to observe strong bunching indicates that this background is correlated with exciton emission, much like the biexciton emission itself. The strength of biexciton antibunching depends on the pump laser wavelength but not on its intensity, provided that the quantum dot is not well above saturation. This result is inconsistent with our expectation that biexciton antibunching will be strongly influenced by free carrier density. On the other hand, the significantly stronger biexciton antibunching that we observe under pulsed excitation (Figure 6.5(b)) suggests that the free carriers may still be playing a role: we remark that under pulsed excitation, free-carriers recombine in a time-scale that is much faster than the biexciton radiative recom-

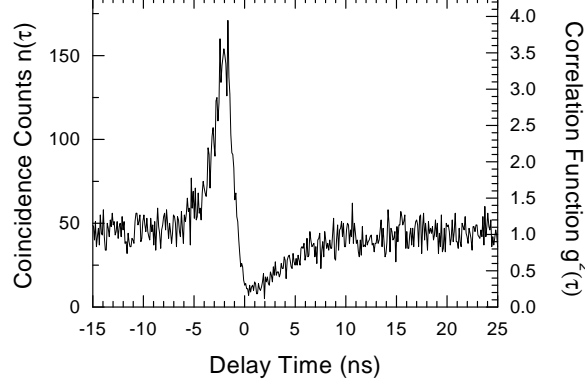


Figure 6.6: Cross correlation function between X1 and XX emissions under continuous wave diode laser excitation at 785 nm. For the chosen pump intensity, X1 line is well below saturation. The signal from X1, filtered by a 0.5 nm interference filter, is sent to the start APD, while the XX line, filtered by a 1 nm filter, is sent to the stop APD. The positive correlation ($g^{(2)} = 3.4$) for $\tau < 0$ followed by the negative correlation ($g^{(2)} = 0.2$) for $\tau > 0$ is an evidence for the cascaded emission of photons.

bination time [52], and therefore their influence on biexciton dynamics is expected to be minimal. We note here that photon antibunching in the biexciton emission of a single InAs quantum dot under pulsed excitation has been reported by another research group [89] as well.

Cross-correlation measurements complement the identification of the biexciton emission: since X1 population is enhanced as a result of the detection of an XX photon, strong correlations between the X1 and XX emissions can be expected. Figure 6.6 shows such a photon cross-correlation measurement, obtained by illuminating the start APD by the X1 emission and stop APD by the XX emission. The depicted quantity here is $\tilde{g}^{(2)}(\tau) = \langle : I_{XX}(t + \tau) I_{X1}(t) : \rangle / (\langle I_{X1}(t) \rangle \langle I_{XX}(t) \rangle)$, where $I_{X1}(t)$ and $I_{XX}(t)$ are the intensities of the X1 and XX emissions, respectively. Remarkable features of this cross-correlation include strong antibunching for $\tau > 0$ and strong bunching for $\tau < 0$ with a close to resolution-limited transition between the

two regimes. For $\tau > 0$, suppression of a joint X1 and XX event arises from the fact that following the detection of an X1 photon, which projects the quantum dot onto its ground-state, detection of an XX photon is very unlikely. Strong bunching for $\tau < 0$ follows from the fact that detection of an XX photon projects the quantum dot onto the X1 state, as discussed earlier. Asymmetry in X1 and XX cross-correlation measurements have been recently reported [90, 91]. The signature depicted in Figure 6.6 proves that the XX emission arises from the decay of the biexciton state into the single exciton state. The strong antibunching in cross-correlation is yet another indication that the additional broadband radiation is correlated with the X1 emission. Figure 6.7 shows power dependent second order photon correlation functions for when XX emission is sent to start and X1 emission to stop APD, under continuous wave (Figure 6.7(a)) and pulsed excitation (Figure 6.7(b)). The increase in the bunching level together with other power-dependent changes in decay times are visible in this Figure.

Having identified the two principal lines in quantum dot spectrum, the next natural question is whether photon correlation spectroscopy can tell us anything about the origin of the X2 emission. The cross-correlation between the X2 and XX emissions only shows antibunching (Figure 6.8(a)), indicating that while those emissions arise from the same quantum dot, the radiative decay of the biexciton state does not populate the X2 state. From the pump power dependent photoluminescence spectra (Figure 6.3(a)), it can be seen that the X2 emission has a stronger pump power dependence than X1 but saturates earlier than the XX line. This may already suggest an identification of X2 as a charged-exciton (trion) line despite the fact that X2-X1 energy difference is smaller than typical reported values. To provide further evidence, we have carried out cross-correlation measurements between the X2 and X1 emissions ($\bar{g}^{(2)}(\tau)$) where the start and stop APDs were illuminated by the X2 and X1 lines, respectively. The resulting X2-X1 cross-correlation function (Figure 6.8(b)) clearly shows asymmetric antibunching with $\bar{g}^{(2)}(0) = 0.3$, which proves once again that the two lines originate from the same quantum dot. The asymmetry with

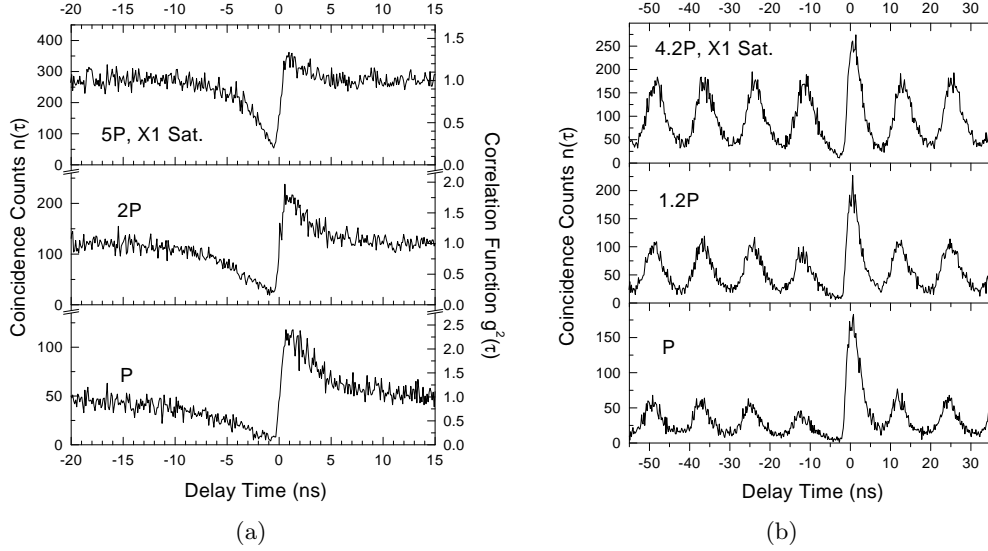


Figure 6.7: Power dependent cross correlation function between X1 and XX emissions under (a) continuous wave and (b) pulsed excitations. XX emission is sent to start APD while X1 emission is sent to stop APD.

fast recovery for $\tau > 0$ is expected if X2 arises from a charged-exciton: the post-measurement state of charged-exciton emission is a singly-charged quantum dot. We would expect single-charge injection into the quantum dot to be much faster than triple charge injection, which in turn determines the recovery-time for $\tau < 0$. Given that the X2 emission of this quantum dot is stronger than what we typically see in other quantum dots, we could envision the presence of an acceptor or donor impurity that increases the relative intensity of charged-exciton emission. Presence of carbon in these samples is well known [73]. We have carried out experiments on other quantum dots and observed identical asymmetric antibunching signatures in cross-correlation between the fundamental exciton line and a secondary line that appears on its red-shifted side (Figures 6.9, and 6.10). The X2-X1 line separation (~ 1 meV) for the quantum dot depicted in Figure 6.9 is similar to the quantum dot analyzed in the first part of this section (Figure 6.3), suggesting that both of these quantum

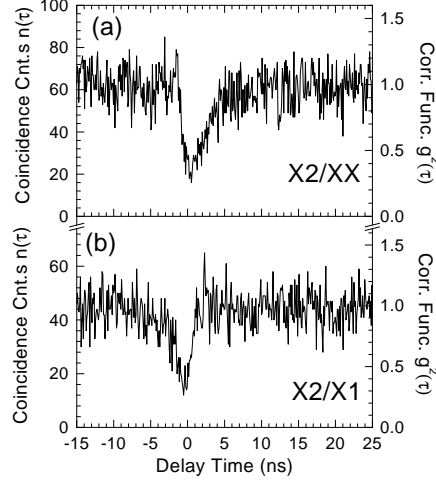


Figure 6.8: Cross-correlation measurements under continuous wave diode laser excitation at 785 nm. (a) The X2 fluorescence is sent to the start APD while XX is sent to the stop APD. The absence of bunching demonstrates that XX emission does not populate the X2 state. (b) The X2 emission is sent to the start APD and the X1 emission to the stop APD. The antibunching dip shows that both transitions stem from the same QD. The asymmetry in the dip indicates a faster recovery for the X1 state after a X2 detection.

dots have the same kind of doping which is probably an acceptor atom revealing the quantum dot positively charged [73]. In contrast, the quantum dot depicted in Figure 6.10 has X2-X1 line separation of 5.5 meV suggesting that this quantum dot is negatively charged.

Here we would like to point out to a difference that is revealed from the cross-correlation measurements we performed on three quantum dots. We observed similar tendencies in the asymmetries obtained from X1/XX, and X2/X1 cross-correlation measurements for all three quantum dots (Figures {6.6, 6.8(b)}, {6.9(a), 6.9(d)}, and {6.10(a), 6.10(d)}). However, X2/XX cross-correlation experiments revealed different asymmetries between the quantum dots that had small X2-X1 energy separation, corresponding to probably positive charging, and the quantum dot that

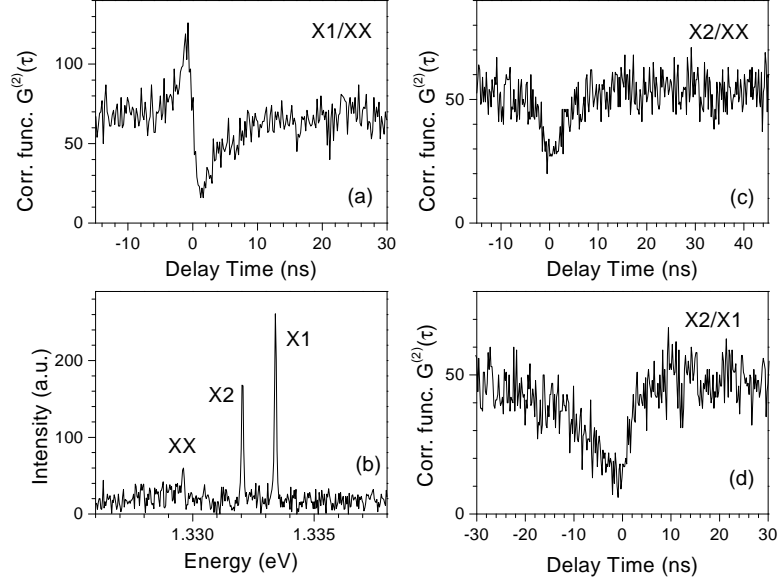


Figure 6.9: Photon correlation spectroscopy measurements done on another quantum dot. Photoluminescence spectrum (b), cross-correlation between (a) X1/XX, (c) X2/XX, and (d) X2/X1 are shown.

had large X2-X1 energy separation, corresponding to probably negative charging. Positively charged quantum dots showed smaller decay times for $\tau < 0$ while having larger decay times for $\tau > 0$ (Figures 6.8(a), and {6.9(c)}), whereas the negatively charged quantum dot showed a larger decay time for $\tau < 0$, and smaller decay time for $\tau > 0$ (Figure 6.10(c)). In X2/XX cross correlation measurements positively charged quantum dots need to capture 2e-1h for $\tau > 0$, and 1h for $\tau < 0$, hence we can conclude that the capture of 1h occurs within resolution limited time scales (< 300 ps) while the capture of 2e-1h occurs within larger time scales (~ 1 ns). In contrast, from X2/XX measurements on the negatively charged quantum dot it can be concluded that the capture of 2h-1e occurs within resolution limited time scales (< 300 ps) while the capture of 1e occurs at larger time scales. This picture is

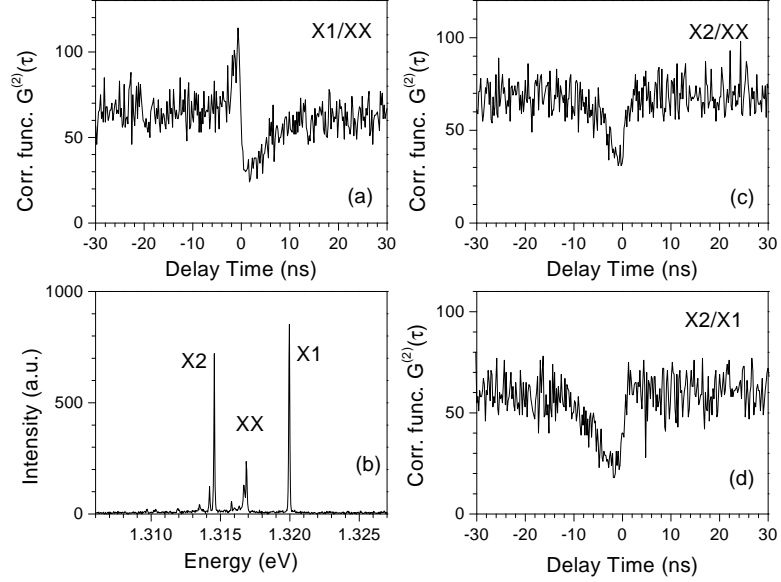


Figure 6.10: Photon correlation spectroscopy measurements done on another quantum dot. Photoluminescence spectrum (b), cross-correlation between (a) X1/XX, (c) X2/XX, and (d) X2/X1 are shown.

self-consistent with such an ordering in carrier capture efficiencies: 1e capture is less efficient than 1e-1h capture, and 1e-1h capture is less efficient than 1h capture. We would like to put however our reservations to this very intuitive result: A systematic study over many differently quantum dots needs to be done in order to reach such a conclusion.

In summary, we have used photon auto- and cross-correlation measurements to identify dominant spectral features of a single quantum dot, and characterize the recombination dynamics under various excitation conditions. Given the difficulty of accurate theoretical calculations and the richness of the quantum dot spectra which differs significantly from one quantum dot to another, we believe that the techniques described here will be invaluable in understanding individual quantum dots.

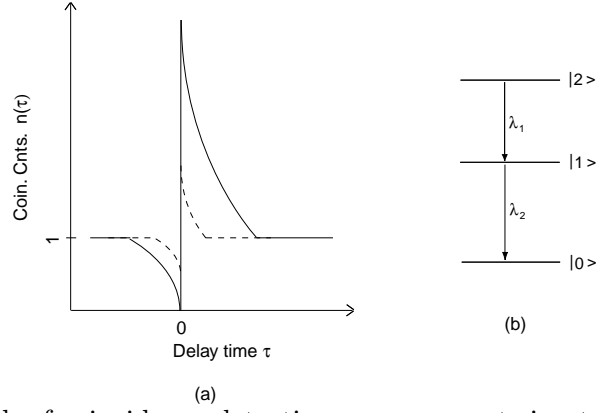


Figure 6.11: Sketch of coincidence detection measurements in atomic cascades Regular three-level cascade from (solid line) a single atom, (dashed line) many atoms.

6.3 Comparison of Cascade Emission Experiments using Atoms and Quantum Dots

So far there have been several experimental demonstrations of cascaded emission using atoms. Three-level cascades were demonstrated using ^{202}Hg [92], and ^{40}Ca [93] atoms, cascade in the emission of two sidebands of the resonance fluorescence was also demonstrated [94]. In this section we aim to compare the experiments performed on atomic three-level cascades with our measurements on the biexciton - single exciton cascade in single quantum dots.

Due to small single atom trapping times, three-level atomic cascade demonstrations were done using the luminescence coming from many atoms. In order to predict the results of those experiments, the analysis done in Section 6.1 can be modified for N identical atoms. Following steps very similar to the steps in derivation of Equation 3.1.21, for a cascade depicted in Figure 6.11(b), the cross-correlation functions in the collective emission of N atoms are given as:

$$g_{12}^{(2)}(\tau) = \frac{N - 1 + g_{12}^{(2)}(\tau)}{N}$$

$$g_{21}^{(2)}(\tau) = \frac{N - 1 + g_{21}^{(2)}(\tau)}{N}$$

Hence it is seen that as the number of excited atoms is increased, both antibunching and bunching signatures of the cascaded emission are reduced (Figure 6.11(a)). Antibunching signature is effected much more severely than the bunching signature because large single-atom bunching levels ($g_{12}^{(2)}(0)$) can be achieved making the bunching effect still observable for the case of many atoms. Consider $N = 100$, and $g_{12}^{(2)}(0) = 100$ then the antibunching level becomes $g_{21}^{(2)}(0) = 0.99$ while bunching level is $g_{12}^{(2)}(0) = 1.99$. This is the situation in cascaded emission experiments performed using many atoms where bunching signature is observed with the absence of antibunching [92, 93]. In contrast, single quantum dot experiments revealed both antibunching and bunching phenomena in cascaded emission, this was a novel experimental signature hitherto not observed in experiments using atoms [86, 90, 91].

6.4 Entangled State Generation Using the Three-Level Cascade in Quantum Dots

It has been predicted that the radiative decay of a single quantum dot biexciton state will result in polarization entangled state generation [53]. Specifically, the two-photon state of a quantum dot has the form of a maximally entangled (Bell) state:

$$|\psi\rangle = \frac{1}{\sqrt{2}}(|\sigma^+\rangle_1|\sigma^-\rangle_2 + |\sigma^-\rangle_1|\sigma^+\rangle_2)$$

where $|\sigma^\pm\rangle_i$ corresponds to single photon Fock states with polarizations (σ^\pm) orthogonal in any basis, $i = 1, 2$ corresponds to the i^{th} photon in the cascaded emission. Such Bell states that violate "*Local Hidden-Variable Theories*" have been successfully demonstrated using atomic cascades [95, 96, 97] analyzing cascaded emission coming from many atoms. The experiments in Ref.s [95, 96, 97] were also performed collecting the luminescence coming from many atoms.

To observe the entanglement in the emission of single quantum dots, we have measured the polarization dependence of the single exciton - biexciton cross-correlation. Under continuous wave excitation, we have seen no evidence for polarization correlations. We believe that spin-decoherence that has been observed to occur in nanosecond timescales for these quantum dots under non-resonant excitation is responsible for the lack of polarization-correlation [98]. Further experiments under different excitation conditions are needed to understand the polarization correlations and eventually for the generation of entangled-photon states. Recently other groups observed classical correlations between the polarizations of the biexcitonic and single excitonic emissions, with no indication for entanglement [99, 100]. These observations were due to asymmetric quantum dots that have polarized emission in a certain axis of asymmetry.

Chapter 7

Two-Photon Interference

Quantum information processing appears as a very fascinating application for single photon sources due to the recent proposal of linear optics quantum computation [7]. In their proposal, Knill and coworkers demonstrated that the availability of a single photon source enables the implementation of efficient quantum computation using only linear optical elements and efficient photo-detectors, relying heavily on two-photon interference on a beam-splitter for realization of probabilistic quantum gates and state preparation. In this chapter, we propose a scheme to obtain two-photon interference from single photons emitted by a single quantum dot as a first step towards the realization of linear optics quantum computation. We also present our initial experimental results.

So far two-photon interference experiments have always been performed using spontaneous parametric down conversion process in nonlinear crystals that give rise to signal and idler photons having a definite quantum correlation between them [101, 102, 103]. However, the application of this entangled photon source to more involved quantum teleportation experiments suffer from low count rates [104]. In such experiments, the laser intensity used in pumping the nonlinear crystal is critically low such that two-pair generation process is suppressed compared to single-pair generation probability, while keeping the rate of single-pair generation events

as large as possible, in order to efficiently perform the experiments. Number of generated photon pairs inherently obeys to Poissonian statistics. Typical single-pair generation rates of $< 10 \text{ KHz}$ are used in such experiments. In contrast, using single quantum dots photon count rates up to $> 100 \text{ MHz}$ can be generated with true sub-Poissonian statistics that ensures no two photon emission [6]. Currently photon count rates larger than 200 KHz are achieved in our laboratory with a total collection efficiency of $\sim 0.1 \%$. For practical applications this collection efficiency can be increased up to more than 50% . These facts showing the advantage of a single quantum dot single photon source over the single photon generation by parametric down conversion process motivates our proposal. In addition to linear optics quantum computation, our proposed high efficiency two-photon entangled state generator can find application in quantum lithography where using an N-photon entangled source, optical resolution in lithography can be reduced to $\lambda/(2N)$ in an N-photon absorbing medium [105].

7.1 Proposed Scheme

Currently demonstrated single photon sources using both single quantum dots and single molecules suffer from inhomogeneous broadening. It is not experimentally conceivable to obtain two separate such single photon sources emitting identical photons as a two photon entangled state generator. Instead the photon stream emitted from a single photon source can be modified to obtain two photon interference.

Our proposed scheme is depicted in Figure 7.1. It relies on separating the single photon stream in two paths by a beam splitter and combining the two paths at two inputs of another beam splitter after introducing an optical delay to one of the paths that is equal to pulse separation. In such a configuration, considering a deterministic single photon source, the two paths will meet at the input of the second beam splitter with a probability of $1/4$. If the photons have identical transform

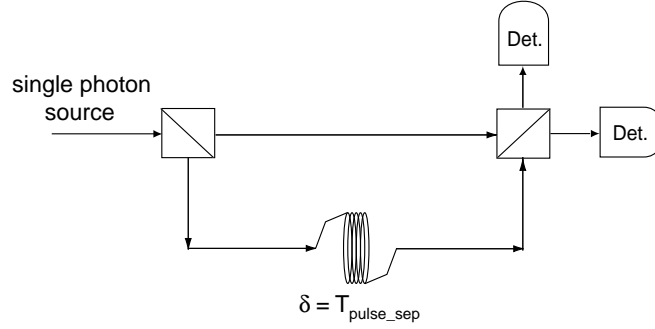


Figure 7.1: Scheme to obtain two-photon interference with a probability $1/4$

limited spectral distributions, the optical delay is made exactly equal to pulse separation, and mode-matching conditions are met, two-photon interference should be observed in the second beam splitter. Since photons emitted by single quantum dots have spontaneous emission lifetimes of several nanoseconds (2 - 4 ns), the length of the optical delay in the longer arm is only critical to millimeters. The experimental evidence of two-photon interference is the absence of coincidences between the two output channels of the second beam splitter, the photons tend to go to the same output channel due to their bosonic nature.

7.2 Analysis of Two-Photon Interference

In a realistic scenario, the quality of two-photon interference heavily depends on whether the emitted photons are transform limited or not. Considering the single quantum dot single photon source, time-jitter and decoherence phenomena are both very effective in causing the single photon wavefunction not to be transform limited. We will discuss the reasons of these phenomena in single quantum dots together with methods to prevent them in the following sections. In this section, we aim to give a general analysis of two-photon interference considering two independent single photon sources. We assume that the sources are identical, they are excited by

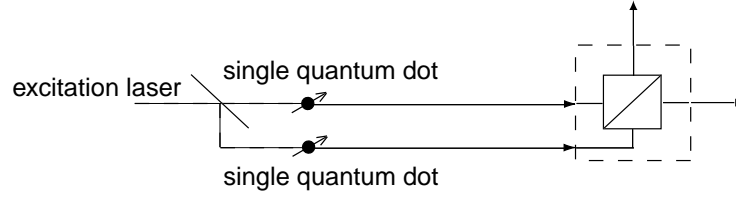


Figure 7.2: Configuration assumed in the analysis of two photon interference: Two independent identical single photon sources excited by the same laser field.

the same laser, and the distance between these sources and the beam splitter is the same (Figure 7.2). This is indeed the situation in our proposal when two photons meet in the input of the second beam splitter in Figure 7.1, under the assumption that $\delta = T_{pulse_sep}$ exactly.

7.2.1 Model of a Quantum Dot for Two-Photon Interference

The rate equation model used for a single quantum dot in the previous chapters is not convenient for this analysis, as we assume decoherence rate to be comparable to spontaneous emission rate. We use the model illustrated in Figure 7.3 for that purpose. We assume low excitation conditions where at most one exciton is generated inside the quantum dot. We also assume a high energy pumping level ($|p\rangle$) that has a large dephasing rate ($\gamma_{p_deph} \gg (\Gamma_p, \Gamma_e, \gamma_{e_deph}, \Omega_L)$) and a spontaneous emission rate (Γ_p) comparable to the other rates in the problem. This pumping level can be the wetting layer or GaAs substrate energy levels, or p-shell states depending on the excitation conditions. We assume a dephasing rate (γ_{e_deph}), and spontaneous emission rate (Γ_e) for the quantum dot dipole.

We start from the general Lindblad form master Equation [29] for the density operator of the three-level system, we will use the assumption of highly dephased pumping level that greatly simplifies the treatment. The master equation is given

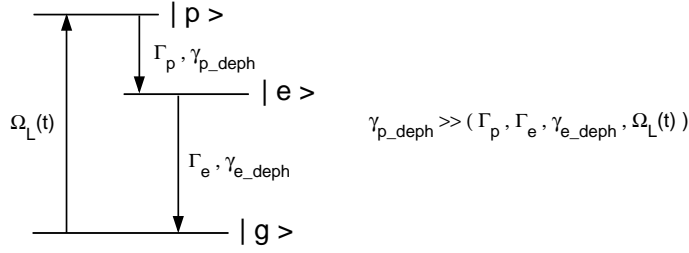


Figure 7.3: Model of a single quantum dot, considering finite dephasing rates.

as:

$$\begin{aligned} \frac{d}{dt}\hat{\rho} = \frac{1}{i\hbar}[\hat{H}, \hat{\rho}] + \frac{\Gamma_e}{2}(2\hat{\sigma}_{ge}\hat{\rho}\hat{\sigma}_{eg} - \hat{\sigma}_{ee}\hat{\rho} - \hat{\rho}\hat{\sigma}_{ee}) - \gamma_{e_deph}\hat{\sigma}_{ee} \\ + \frac{\Gamma_p}{2}(2\hat{\sigma}_{ep}\hat{\rho}\hat{\sigma}_{pe} - \hat{\sigma}_{pp}\hat{\rho} - \hat{\rho}\hat{\sigma}_{pp}) - \gamma_{p_deph}\hat{\sigma}_{pp} \end{aligned} \quad (7.2.1)$$

where \hat{H} is the three-level system Hamiltonian:

$$\hat{H} = \hbar\omega_{eg}\hat{\sigma}_{ee} + \hbar\omega_{pg}\hat{\sigma}_{ee} + \hbar\omega_L\hat{a}^\dagger\hat{a} + \hbar\frac{\Omega_L(t)}{2}(\hat{\sigma}_{pg}e^{-i\omega_{pg}t} + \hat{\sigma}_{gp}e^{i\omega_{pg}t}) \quad (7.2.2)$$

In Equation 7.2.2, we treat the laser field classically given by the Rabi frequency ($\Omega_L(t) = \frac{2|\mu_{eg} \cdot \epsilon||E_{max}(t)|}{\hbar}$). We further assume $\omega_{pg} = \omega_L$.

Now we derive the simplified optical Bloch equations for the three-level system using Equation 7.2.1 together with the equation for the average value of a general observable represented by the hermitian operator \hat{A} :

$$\langle \hat{A} \rangle = Tr\{\hat{\rho}\hat{A}\} \quad (7.2.3)$$

The following equation can be written for $\langle \tilde{\sigma}_{pe} \rangle$:

$$\frac{d}{dt}\langle \tilde{\sigma}_{pe}(t) \rangle = -\gamma_p\langle \tilde{\sigma}_{pe}(t) \rangle + i\frac{\Omega_L}{2}\langle \tilde{\sigma}_{ge}(t) \rangle$$

where $\gamma_p = \gamma_{e_deph} + \frac{\Gamma_e}{2}$ is the total dephasing rate of the level $|e\rangle$, $\tilde{\sigma}_{pe}(t) = e^{-i\omega_{pe}t}\hat{\sigma}_{pe}(t)$ and $\tilde{\sigma}_{ge}(t) = e^{i\omega_{eg}t}\hat{\sigma}_{ge}(t)$ represent the system operators in rotating

frame. Under the assumption $\gamma_p \gg (\Gamma_p, \Gamma_e, \gamma_{e_deph}, \Omega_L(t))$, $\langle \tilde{\sigma}_{pe} \rangle$ reaches its steady state for the time scales relevant to other operators:

$$\frac{d\langle \tilde{\sigma}_{pe}(t) \rangle}{dt} \approx 0 \Rightarrow \langle \tilde{\sigma}_{pe}(t) \rangle \approx \frac{i\Omega_L(t)/2}{\gamma_p + \frac{\Gamma_e}{2}} \langle \tilde{\sigma}_{ge}(t) \rangle$$

Substituting the above equation into the Bloch equation for $\langle \tilde{\sigma}_{eg}(t) \rangle = e^{-i\omega_{eg}t} \langle \hat{\sigma}_{eg}(t) \rangle$:

$$\begin{aligned} \frac{d}{dt} \langle \tilde{\sigma}_{eg}(t) \rangle &= -\gamma_e \langle \tilde{\sigma}_{eg}(t) \rangle - i \frac{\Omega_L(t)}{2} \langle \tilde{\sigma}_{ep}(t) \rangle \\ &= - \left(\gamma_e + \frac{\Omega_L^2/4}{\gamma_p + \frac{\Gamma_e}{2}} \right) \langle \tilde{\sigma}_{eg}(t) \rangle \end{aligned} \quad (7.2.4)$$

Under the highly dephased $|p\rangle$ level assumption $\gamma_e \gg \frac{\Omega_L(t)^2/4}{\gamma_p + \frac{\Gamma_e}{2}}$, Equation 7.2.4 reduces to:

$$\frac{d}{dt} \langle \tilde{\sigma}_{eg}(t) \rangle = -\gamma_e \langle \tilde{\sigma}_{eg}(t) \rangle \quad (7.2.5)$$

This is the first of the simplified Bloch equations obtained in this subsection. This Equation 7.2.5 is identical to the case of incoherent resonant excitation of a two-level system. Highly dephased level $|p\rangle$ has the effect of removing the coherence between the excitation laser and the level $|e\rangle$.

Using the master Equation 7.2.1 we can write the following optical Bloch equations for $\langle \hat{\sigma}_{pp}(t) \rangle$, $\langle \hat{\sigma}_{pg}(t) \rangle$, and $\langle \hat{\sigma}_{ee}(t) \rangle$:

$$\begin{aligned} \frac{d}{dt} \langle \hat{\sigma}_{pp}(t) \rangle &= -i \frac{\Omega_L(t)}{2} (\langle \tilde{\sigma}_{pg}(t) \rangle - \langle \tilde{\sigma}_{gp}(t) \rangle) - \Gamma_p \langle \hat{\sigma}_{pp}(t) \rangle \\ \frac{d}{dt} \langle \tilde{\sigma}_{pg}(t) \rangle &= \gamma_P \langle \tilde{\sigma}_{pg}(t) \rangle - i \frac{\Omega_L(t)}{2} (\langle \hat{\sigma}_{pp}(t) \rangle - \langle \hat{\sigma}_{gg}(t) \rangle) \\ \frac{d}{dt} \langle \hat{\sigma}_{ee}(t) \rangle &= \Gamma_P \langle \hat{\sigma}_{pp}(t) \rangle - \Gamma_e \langle \hat{\sigma}_{ee}(t) \rangle \end{aligned} \quad (7.2.6)$$

Once again we use the highly dephased $|p\rangle$ level assumption, $\gamma_p \gg (\Gamma_p, \Gamma_e, \gamma_{e_deph}, \Omega_L(t))$, to obtain:

$$\frac{d\langle \tilde{\sigma}_{pg}(t) \rangle}{dt} \approx 0 \Rightarrow \langle \tilde{\sigma}_{pg}(t) \rangle \approx \frac{-i\Omega_L(t)/2}{\gamma_p} (\langle \hat{\sigma}_{pp}(t) \rangle - \langle \hat{\sigma}_{gg}(t) \rangle) \quad (7.2.7)$$

Substituting Equation 7.2.7 into Equation 7.2.6, the following set of Optical Bloch equations can be obtained for $\langle\hat{\sigma}_{pp}(t)\rangle$, $\langle\hat{\sigma}_{ee}(t)\rangle$, and $\langle\hat{\sigma}_{gg}(t)\rangle$:

$$\begin{aligned}\frac{d}{dt}\langle\hat{\sigma}_{pp}(t)\rangle &= -(W_P(t) + \Gamma_P)\langle\tilde{\hat{\sigma}}_{gp}(t)\rangle + W_P(t)\Gamma_p\langle\hat{\sigma}_{gg}(t)\rangle \\ \frac{d}{dt}\langle\hat{\sigma}_{ee}(t)\rangle &= \Gamma_P\langle\hat{\sigma}_{pp}(t)\rangle - \Gamma_e\langle\hat{\sigma}_{ee}(t)\rangle \\ \frac{d}{dt}\langle\tilde{\hat{\sigma}}_{gg}(t)\rangle &= W_P(t)\langle\hat{\sigma}_{pp}(t)\rangle - \langle\hat{\sigma}_{gg}(t)\rangle + \Gamma_e\langle\hat{\sigma}_{ee}(t)\rangle\end{aligned}\quad (7.2.8)$$

Where we substituted $\frac{\Omega_L(t)^2/2}{\gamma_p}$ by $W_P(t)$, and used the equation:

$$\langle\hat{\sigma}_{pp}(t)\rangle + \langle\hat{\sigma}_{ee}(t)\rangle + \langle\hat{\sigma}_{gg}(t)\rangle = 1 \Rightarrow \frac{d}{dt}\langle\hat{\sigma}_{pp}(t)\rangle + \frac{d}{dt}\langle\hat{\sigma}_{ee}(t)\rangle + \frac{d}{dt}\langle\hat{\sigma}_{gg}(t)\rangle = 0$$

In summary we obtained the following set of optical Bloch equations for the model depicted in Figure 7.3:

$$\frac{d}{dt} \begin{bmatrix} \langle\hat{\sigma}_{pp}(t)\rangle \\ \langle\hat{\sigma}_{ee}(t)\rangle \\ \langle\hat{\sigma}_{gg}(t)\rangle \\ \langle\tilde{\hat{\sigma}}_{eg}(t)\rangle \end{bmatrix} = \begin{bmatrix} -(W_P(t) + \Gamma_p) & 0 & W_P(t) & 0 \\ \Gamma_p & -\Gamma_e & 0 & 0 \\ W_P(t) & \Gamma_e & -W_P(t) & 0 \\ 0 & 0 & 0 & -\gamma_e \end{bmatrix} \begin{bmatrix} \langle\hat{\sigma}_{pp}(t)\rangle \\ \langle\hat{\sigma}_{ee}(t)\rangle \\ \langle\hat{\sigma}_{gg}(t)\rangle \\ \langle\tilde{\hat{\sigma}}_{eg}(t)\rangle \end{bmatrix} \quad (7.2.9)$$

The above set of equations are still the rate equations for the population densities of levels $|p\rangle$, $|e\rangle$, and $|g\rangle$. In addition to those, we have the equation for $\langle\tilde{\hat{\sigma}}_{eg}(t)\rangle$ representing the decay of the coherence between levels $|e\rangle$, and $|g\rangle$. It is apparent that level $|p\rangle$ has no effect on the decoherence rate of $\langle\tilde{\hat{\sigma}}_{eg}(t)\rangle$ so long as $\gamma_e \gg \frac{\Omega_L(t)^2/4}{\gamma_p + \frac{\Gamma_e}{2}}$ is satisfied. Under this highly dephased assumption, level $|p\rangle$ only determines the time-jitter, as demonstrated in the next subsections.

7.2.2 Calculation of Coincidence Detection Rate

We now aim to write the relative coincidence detection probability at the output of the beam splitter depicted in Figure 7.2 by the help of the set of Equations 7.2.9. Consider the general beam splitter depicted in Figure 7.4 that has the general input-output relationship for single mode quadrature field components:

$$\begin{bmatrix} \hat{E}_{\mathbf{k}_3}^+(\omega_3) \\ \hat{E}_{\mathbf{k}_4}^+(\omega_4) \end{bmatrix} = \begin{bmatrix} t & r \\ r & t \end{bmatrix} \begin{bmatrix} \hat{E}_{\mathbf{k}_1}^+(\omega_1) \\ \hat{E}_{\mathbf{k}_2}^+(\omega_2) \end{bmatrix} \quad (7.2.10)$$

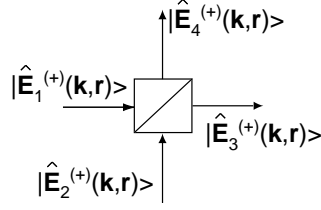


Figure 7.4: Beam splitter

having the energy and momentum conservation relationships given as:

$$\mathbf{k}_1 + \mathbf{k}_2 = \mathbf{k}_3 + \mathbf{k}_4, \quad \omega_1 = \omega_2 = \omega_3 = \omega_4$$

We assume the polarization vector to be the same for all field components. Taking the Fourier transform of both sides in Equation 7.2.10, reveals:

$$\begin{bmatrix} \hat{E}_3^+(t) \\ \hat{E}_4^+(t) \end{bmatrix} = \begin{bmatrix} t & r \\ r & t \end{bmatrix} \begin{bmatrix} \hat{E}_1^+(t) \\ \hat{E}_2^+(t) \end{bmatrix} \Rightarrow \begin{bmatrix} \hat{a}_3(t) \\ \hat{a}_4(t) \end{bmatrix} = \begin{bmatrix} t & r \\ r & t \end{bmatrix} \begin{bmatrix} \hat{a}_1(t) \\ \hat{a}_2(t) \end{bmatrix} \quad (7.2.11)$$

\hat{a}_1 , \hat{a}_2 , \hat{a}_3 , and \hat{a}_4 are the photon annihilation operators of the respective channels. We assumed r , and t to be independent from ω . Using Equation 7.2.11, the unnormalized second order coherence function between channels 3, and 4:

$$G_{34}^{(2)}(t, \tau) = \langle a_3^\dagger(t) a_4^\dagger(t + \tau) a_4(t + \tau) a_3(t) \rangle \quad (7.2.12)$$

can be written as:

$$\begin{aligned} G_{34}^{(2)}(t, \tau) &= |r|^4 \langle \hat{a}_2^\dagger(t) \hat{a}_1^\dagger(t + \tau) \hat{a}_1(t + \tau) \hat{a}_2(t) \rangle \\ &\quad + |t|^4 \langle \hat{a}_1^\dagger(t) \hat{a}_2^\dagger(t + \tau) \hat{a}_2(t + \tau) \hat{a}_1(t) \rangle \\ &\quad + r^2 (t^*)^2 \langle \hat{a}_1^\dagger(t) \hat{a}_2^\dagger(t + \tau) \hat{a}_1(t + \tau) \hat{a}_2(t) \rangle \\ &\quad + (r^*)^2 t^2 \langle \hat{a}_2^\dagger(t) \hat{a}_1^\dagger(t + \tau) \hat{a}_2(t + \tau) \hat{a}_1(t) \rangle \end{aligned} \quad (7.2.13)$$

All other terms in the expression of $G_{34}^{(2)}(\tau)$ are equal to zero due to the assumed input state $|\psi\rangle = |1_1, 1_2\rangle$. At this stage making use of the source-field expression in

Equation 3.2.2 we can write Equation 7.2.13 in terms of the quantum dot projection operators revealing the equation below:

$$\begin{aligned}
G_{34}^{(2)}(t, \tau) = & |r|^4 \langle \hat{\sigma}_{eg_2}(t) \hat{\sigma}_{ee_1}(t + \tau) \hat{\sigma}_{ge_2}(t) \rangle + |t|^4 \langle \hat{\sigma}_{eg_1}(t) \hat{\sigma}_{ee_2}(t + \tau) \hat{\sigma}_{ge_1}(t) \rangle \\
& + r^2 (t^*)^2 \langle \hat{\sigma}_{eg_1}(t) \hat{\sigma}_{eg_2}(t + \tau) \hat{\sigma}_{ge_1}(t + \tau) \hat{\sigma}_{ge_2}(t) \rangle \\
& + (r^*)^2 t^2 \langle \hat{\sigma}_{eg_2}(t) \hat{\sigma}_{eg_1}(t + \tau) \hat{\sigma}_{ge_2}(t + \tau) \hat{\sigma}_{ge_1}(t) \rangle
\end{aligned} \tag{7.2.14}$$

The subscripts 1, and 2 denote the two quantum dots. Since the quantum dots are assumed to be identical and independent Equation 7.2.14 can be further simplified to:

$$\begin{aligned}
G_{34}^{(2)}(t, \tau) = & (|r|^4 + |t|^4) \langle \hat{\sigma}_{ee}(t) \rangle \langle \hat{\sigma}_{ee}(t + \tau) \rangle \\
& + (r^2 (t^*)^2 + (r^*)^2 t^2) |G^{(1)}(t, \tau)|^2
\end{aligned} \tag{7.2.15}$$

where $G^{(1)}(t, \tau)$ represents the unnormalized first order coherence function:

$$G^{(1)}(t, \tau) = \left(G^{(1)}(t, -\tau) \right)^* = \langle \hat{\sigma}_{eg}(t + \tau) \hat{\sigma}_{ge}(t) \rangle \tag{7.2.16}$$

The first term in the Equation 7.2.15 corresponds to the classical coincidence counts for non-interfering photons, whereas the second term is due to the two-photon interference. The first order coherence function of individual photons determines the level of interference, e.g. the extreme case of the coherence length of each photon being 0 corresponds to no interference between the two photons.

7.2.3 Solution of Two-Photon Interference for Single Quantum Dots

In this subsection we analyze Equation 7.2.15 by solving the internal dynamics of a single quantum dot using the set of Equations 7.2.9. We assume a balanced beam splitter, $r = \frac{1}{\sqrt{2}}, t = \frac{i}{\sqrt{2}}$, revealing:

$$G_{34}^{(2)}(t, \tau) = \frac{1}{2} \left(\langle \hat{\sigma}_{ee}(t) \rangle \langle \hat{\sigma}_{ee}(t + \tau) \rangle - |G^{(1)}(t, \tau)|^2 \right) \tag{7.2.17}$$

We first consider the two-photon interference under continuous wave excitation conditions, followed by the pulsed excitation case.

(i) Continuous wave excitation:

For continuous wave excitation, in Equation 7.2.17 $\langle \hat{\sigma}_{ee}(t) \rangle$, and $\langle \hat{\sigma}_{ee}(t + \tau) \rangle$ can be substituted by the steady state value of the population density of level $|e\rangle$, $\langle \hat{\sigma}_{ee}(t) \rangle_{ss}$. $G^{(1)}(t, \tau)$ can then be calculated by multiplying Equation 7.2.9 with $\tilde{\sigma}_{ge}(t)$ from the right side, and using the quantum regression theorem to calculate the two-time averages as it was done in the calculations in the previous chapters. By this way, the equation and initial condition below can be obtained for $G^{(1)}(t, \tau)$:

$$\frac{dG^{(1)}(t, \tau)}{dt} = -\gamma_e G^{(1)}(t, \tau) \ , \ G^{(1)}(t, 0) = \langle \hat{\sigma}_{ee}(t) \rangle \quad (7.2.18)$$

The solution to Equation 7.2.18 is:

$$G^{(1)}(t, \tau) = \langle \hat{\sigma}_{ee}(t) \rangle e^{-\gamma_e \tau} \quad (7.2.19)$$

By substituting the solution to $G^{(1)}(t, \tau)$ into Equation 7.2.17, normalized $G_{34}^{(2)}(\tau)$ reads:

$$\begin{aligned} g_{34}^{(2)}(\tau) &= \frac{1}{2} \left(1 - \frac{|G^{(1)}(t, \tau)|^2}{\langle \hat{\sigma}_{ee}(t) \rangle \langle \hat{\sigma}_{ee}(t + \tau) \rangle} \right) \\ &= \frac{1}{2} (1 - e^{-2\gamma_e \tau}) \end{aligned} \quad (7.2.20)$$

Hence, for the continuous wave excitation case two-photon interference is solely determined by the total dephasing in the level $|e\rangle$, $\gamma_e = \gamma_{e_deph} + \frac{\Gamma_e}{2}$. The decay time of two-photon interference is: $\frac{1}{2\gamma_e}$, and time-jitter caused by the level $|p\rangle$ has no effect on the interference.

(ii) Pulsed excitation:

We now analyze two-photon interference considering a pulsed laser having small pulse width and large pulse separation such that single photon operation from the quantum dots is achieved (Chapter 4). In this case it is convenient to calculate the unnormalized second order photon correlation function that is only dependent on variable τ :

$$G_{34_avg}^{(2)}(\tau) = \int_0^\infty dt G_{34}^{(2)}(t, \tau) \quad (7.2.21)$$

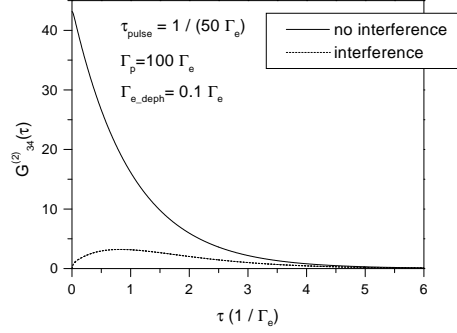


Figure 7.5: $G_{34_avg}^{(2)}(\tau)$ calculated using $\tau_{pulse} = 1/(50\Gamma_e)$, $\Gamma_p = 100\Gamma_e$, and $\Gamma_{e_deph} = 0.1\Gamma_e$ (dashed curve). Classical no-interference case is also plotted for normalization (straight curve).

in its unnormalized form. In this analysis, we first calculate $G^{(1)}(t, \tau)$ using Equation 7.2.19 for all t , and τ . $G_{34}^{(2)}(t, \tau)$ is then calculated by substituting $G^{(1)}(t, \tau)$ in Equation 7.2.17. Integration of $G_{34}^{(2)}(t, \tau)$ over all t reveals $G_{34_avg}^{(2)}(\tau)$ that corresponds to the distribution of detected coincidence in the experiment. An exemplary solution of $G_{34_avg}^{(2)}(\tau)$ is shown in Figure 7.5. $G_{34_avg}^{(2)}(\tau)$ calculated considering no two-photon interference is also plotted in Figure 7.5 for normalization.

To observe the effect of dephasing rate (Γ_{e_deph}), and time-jitter (Γ_p), we calculated the normalized coincidence detection probability per pulse for various dephasing rates and time-jitters. In its unnormalized form, the coincidence detection probability is given as:

$$P_{34}(T_{pulse}) = \int_0^{T_{pulse}} d\tau G_{34_avg}^{(2)}(\tau) \quad (7.2.22)$$

The results of the calculations are depicted in Figure 7.6 showing the strong dependence of the coincidence detection rate, on γ_{e_deph} , and Γ_p . In Figure 7.6, p_{34} is normalized such that $p_{34} = 0.5$ corresponds to no two-photon interference as shown in Figure 7.5.

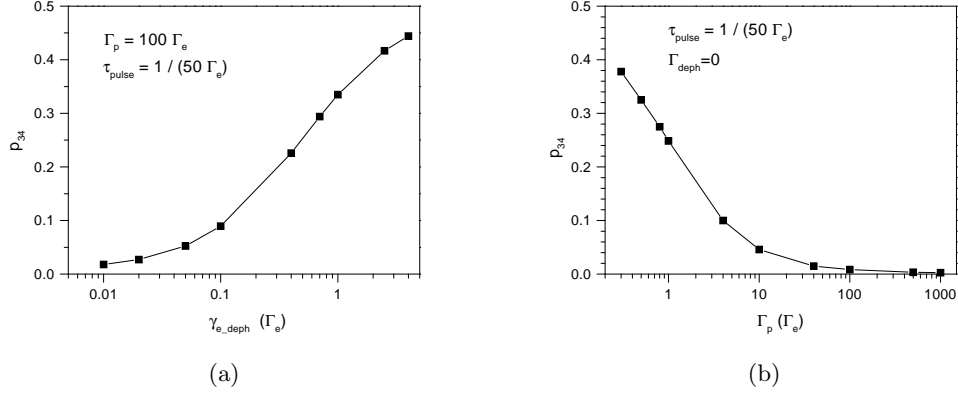


Figure 7.6: Effect of the (a) dephasing rate (γ_{e_deph}), and (b) time-jitter (Γ_p) to two-photon interference. $p_{34} = 0.5$ corresponds to no interference.

7.3 Dephasing in Single Quantum Dots

As denoted in the previous section, the first step in implementing our two-photon interference scheme is to have transform limited emission from the quantum dots. For that reason we have performed linewidth measurements on the quantum dot emission lines using a scanning Fabry-Perot interferometer. The results of these measurements that revealed linewidths at least 5 times larger than the transform limited linewidth of quantum dot emission are presented in this section. We should note that recently a transform limited quantum dot linewidth has been reported under continuous wave p-shell excitation conditions at 2 K [106].

We have used a Scanning Fabry-Perot interferometer (Burleigh TL-0300-S-NIR Laser Spectrum Analyzer, Free Spectral Range = 15 GHz = 62 μ eV, Finesse=70, center wavelength = 950 nm) to measure the quantum dot linewidths. In the setup plotted in Figure 7.7, the quantum dot emission is filtered using 0.5 nm, and 1 nm interference filters, and then sent to an APD passing through the scanning Fabry-Perot interferometer. The APD output is stored in a multi-channel scaler (Stanford instruments model SR430) that is triggered by the Scanning Fabry-Perot ramp signal.

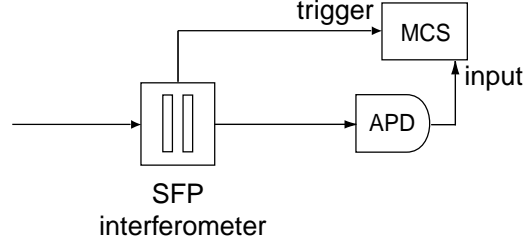


Figure 7.7: Experimental setup using the Scanning Fabry-Perot Interferometer

Quantum Dot	Measured Linewidth			
	charged X		neutral X	
	(ps)	(μeV)	(ps)	(μeV)
Figures 6.3-6.8	53	12	11	60
Figure 6.9	111	5.7	18	35
Figure 6.10	98	6.5	80	8

Table 7.1: Measured linewidths of three quantum dots

After several minutes of integration the spectrum in the multi-channel scaler reveals the linewidth information.

Under continuous wave excitation conditions using diode laser (at 785 nm), a large variety of linewidth values ranging between 5.7 - 60 μeV were measured from various quantum dots. Among these quantum dots, the ones in which we could clearly identify the charged and neutral single-exciton emissions, using photon correlation spectroscopy, had the linewidths shown in Table 7.1.

Table 7.1 demonstrates linewidth values we obtained from three quantum dots' charged and neutral exciton emissions under nonresonant continuous wave excitation (diode laser at 785 nm). The first, second, and third quantum dots in Table 7.1 are the ones analyzed in Figures 6.3-6.8, Figure 6.9, and Figure 6.10 respectively. The identification of the charged and neutral single exciton lines of these quantum dots has been done using the photon correlation spectroscopy techniques as discussed in

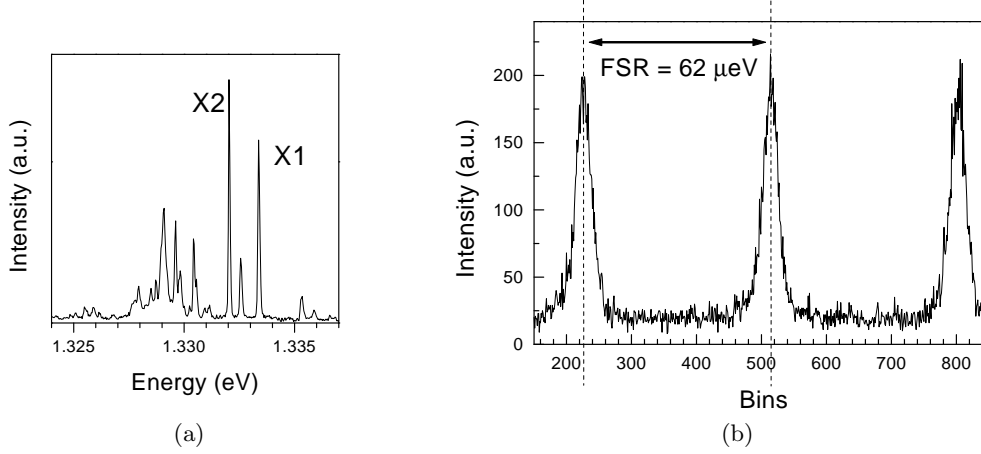


Figure 7.8: (a) Photoluminescence spectrum of the quantum dot under continuous wave excitation using diode laser. Charged excitonic (X2) and excitonic (X1) emissions are visible. (b) A linewidth of $5.7 \mu\text{eV}$ is measured for the X2 emission under continuous wave excitation conditions using the scanning Fabry-Perot interferometer.

Chapter 6. We should note here that the linewidth values shown in Table 7.1 are not representative of a general average quantum dot from our samples.

The value $5.7 \mu\text{eV}$ in Table 7.1 is the smallest linewidth value we have been able to measure from any quantum dot under nonresonant continuous wave excitation. This measurement together with the photoluminescence spectrum of this quantum dot are depicted in Figure 7.8. In this excitation condition this value is also smaller than all other linewidth values reported in the literature. For this specific charged exciton emission, lifetime ($\sim 2 \text{ ns}$) corresponds to a transform limited linewidth of $0.32 \mu\text{eV}$. Hence the measured linewidth ($5.7 \mu\text{eV}$) is still mainly determined by the dephasing processes in the quantum dot, dephasing processes are ~ 18 times faster than spontaneous emission.

Although the values in Table 7.1 are rather different from one quantum dot to another, a general trend between charged exciton and neutral exciton linewidths can be deduced: charged exciton emission lines consistently have smaller broadenings

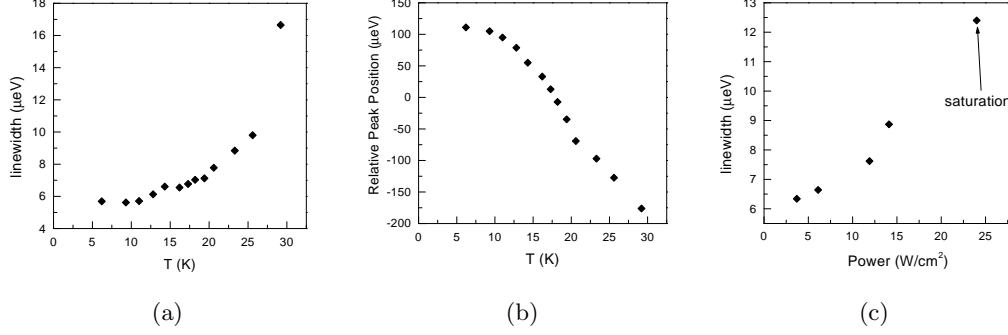


Figure 7.9: Analysis of the X2 line in Figure 7.8(a). Temperature dependent (a) linewidth (b) emission energy, and (c) power dependent linewidth are plotted under continuous wave diode laser excitation.

than the neutral exciton emission lines for these three cases. Such a trend has also been observed by another research group [107]. Detailed calculations should be done to clarify this phenomenon. However as a first reasoning, it can be argued that the existence of an extra charge in the s-shell reduces the dephasing rate by decreasing the interaction between the quantum dot exciton and other free carriers.

In the remaining of this section we will discuss further linewidth experiments performed on the X2 line in Figure 7.8(a) that showed the smallest linewidth. To identify the main cause of broadening, we performed power and temperature dependent linewidth measurements. The results of these measurements are plotted in Figure 7.9. The temperature dependence depicted in Figure 7.9(a) shows that the linewidth stays constant up to 10 K and then starts increasing, hence for this quantum dot, dephasing caused by lattice interaction is not important up to 10 K. In contrast, linewidth has a strong power dependence under continuous wave excitation conditions (Figure 7.9(c)) suggesting that free-carriers are the dominant factor determining the quantum dot linewidth. Temperature dependent drift of the emission energy is also visible in Figure 7.9(b).

We also performed linewidth measurements under pulsed excitation condi-

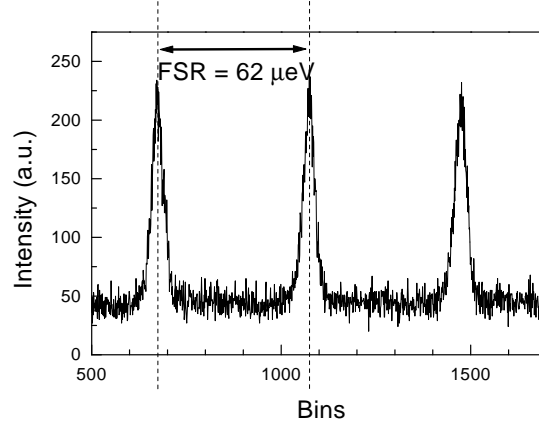


Figure 7.10: Linewidth measurement of the line in Figure 7.8(a) under pulsed Ti:Sa excitation, revealing a linewidth of $5.6 \mu\text{eV}$.

tions in order to prevent the dephasing effects due to free carriers. As depicted in Figure 7.10 this measurement revealed a linewidth of $5.6 \mu\text{eV}$ in the low excitation regime. The fact that this value is still 16 times larger than the transform limited linewidth can be explained by the trapped charges having trapping times comparable to single-excitonic lifetime. We have indeed measured carrier lifetimes as large as 1 ns from some low energy states of the wetting layer; such states can be the reason of the dephasing we observe.

7.4 Experimental Results

In this section we intend to discuss our first attempts to obtain two-photon interference that to our dismay revealed no interference signatures. For these experiments we have changed the proposed setup in Figure 7.1 in order to optimize the experimental conditions. We have replaced the first beam splitter by a combination of polarizing beam splitter and $\frac{\lambda}{2}$ waveplate in the long arm in order not to loose counts by putting polarizers at both arms. Furthermore we have placed two

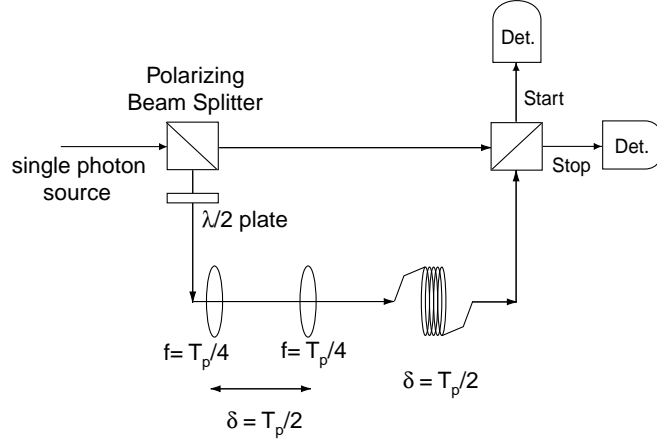


Figure 7.11: Modified form of the two-photon interference proposal

lenses with focal lengths of $f = T_{pulse_sep}/4$ to the longer arm with a separation of $T_{pulse_sep}/2$ between them in order to correct for the divergence of the Gaussian beam. The necessity of a 3.69 m (12.3 ns) long delay line makes the mode matching conditions quite hard to satisfy using free space optics.

For the experimental configuration depicted in Figure 7.1, coincidence detection probability of two non-interfering photons can be readily predicted. For general coefficients η_{short} , η_{long} , η_{start} , and η_{stop} corresponding to the total collection efficiency in the long arm, total collection efficiency in the short arm, detection efficiency of the start APD, and detection efficiency of the stop APD respectively, considering an ideal beam splitter, the probability of a coincidence detection at times $\tau = 0$, $\tau = T_{pulse_sep}$, $\tau = -T_{pulse_sep}$, and $|\tau| > 2T_{pulse_sep}$ are given as:

$$\begin{aligned}
 P_{12}(\tau = 0) &= \left(\frac{1}{2}\eta_{short}\frac{1}{2}\eta_{start} \right) \left(\frac{1}{2}\eta_{long}\frac{1}{2}\eta_{stop} \right) + \\
 &\quad \left(\frac{1}{2}\eta_{long}\frac{1}{2}\eta_{start} \right) \left(\frac{1}{2}\eta_{short}\frac{1}{2}\eta_{stop} \right) \\
 P_{12}(\tau = T_{pulse_sep}) &= \left(\frac{1}{2}\eta_{short}\frac{1}{2}\eta_{start} \right) \left(\frac{1}{2}\eta_{long}\frac{1}{2}\eta_{stop} \right) +
 \end{aligned}$$

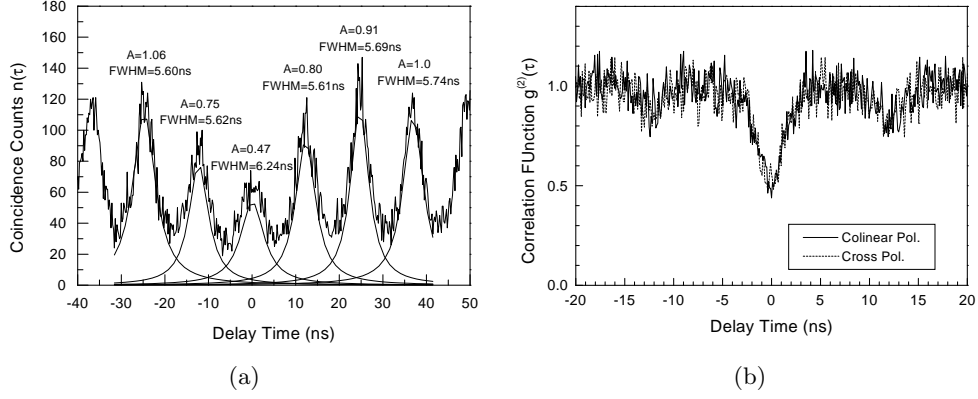


Figure 7.12: Failing results of two-photon interference experiments revealing no interference under (a) pulsed and (b) continuous wave excitations.

$$\begin{aligned}
 P_{12}(\tau = -T_{pulsesep}) &= \left(\frac{1}{2}\eta_{long}\frac{1}{2}\eta_{start} \right) \left(\left(\frac{1}{2}\eta_{long}\frac{1}{2}\eta_{stop} \right) + \left(\frac{1}{2}\eta_{short}\frac{1}{2}\eta_{stop} \right) \right) \\
 &+ \left(\frac{1}{2}\eta_{short}\frac{1}{2}\eta_{start} \right) \left(\left(\frac{1}{2}\eta_{short}\frac{1}{2}\eta_{stop} \right) + \left(\frac{1}{2}\eta_{long}\frac{1}{2}\eta_{stop} \right) \right) + \\
 &\left(\frac{1}{2}\eta_{long}\frac{1}{2}\eta_{start} \right) \left(\frac{1}{2}\eta_{long}\frac{1}{2}\eta_{stop} \right) \\
 P_{12}(|\tau| > 2T_{pulsesep}) &= \left(\frac{1}{2}\eta_{short}\frac{1}{2}\eta_{start} \right) \left(\left(\frac{1}{2}\eta_{short}\frac{1}{2}\eta_{stop} \right) + \left(\frac{1}{2}\eta_{long}\frac{1}{2}\eta_{stop} \right) \right) + \\
 &\left(\left(\frac{1}{2}\eta_{long}\frac{1}{2}\eta_{stop} \right) + \left(\frac{1}{2}\eta_{short}\frac{1}{2}\eta_{stop} \right) \right)
 \end{aligned}$$

Hence for $\eta_{short} = \eta_{long}$, coincidence detection probabilities of non-interfering photons are:

$$\begin{aligned}
 \frac{P_{12}(\tau = 0)}{P_{12}(|\tau| > 2T_{pulsesep})} &= 0.5 \\
 \frac{P_{12}(\tau = T_{pulsesep})}{P_{12}(|\tau| > 2T_{pulsesep})} &= \frac{P_{12}(\tau = T_{pulsesep})}{P_{12}(|\tau| > 2T_{pulsesep})} = 0.75
 \end{aligned}$$

In the case of identical photons emitted by the single photon source, only the coincidence detection probability at $\tau = 0$ will be equal to 0. Therefore coincidence

detection probabilities for interfering photons are:

$$\frac{P_{12}(\tau = 0)}{P_{12}(|\tau| > 2T_{pulsesep})} = 0$$

$$\frac{P_{12}(\tau = T_{pulsesep})}{P_{12}(|\tau| > 2T_{pulsesep})} = \frac{P_{12}(\tau = T_{pulsesep})}{P_{12}(|\tau| > 2T_{pulsesep})} = 0.75$$

The results of our initial two-photon interference experiments are depicted in Figure 7.12(a). In these experiments the values $g^{(2)}(0) = 0.5$, and $g^{(2)}(T_{pulsesep}) = 0.75$ are clear signatures of non-interfering photons. Figure 7.12(b) shows the results of our two-photon interference experiments under continuous wave excitation. In this case although we do not have a triggered single photon source, coincidences detected at $\tau = 0$ are still due to non-interfering single photons. In Figure 7.12(b) we also observe no difference between the detected coincidences in co-linear and orthonormal polarizations, this is another indications that there is no two-photon interference. As discussed in the previous sections, the reason for our failure in observing two-photon interference phenomenon was mainly the large dephasing rates of the quantum dot emissions under nonresonant continuous wave and pulsed excitation conditions.

As a further step towards observing two-photon interference, we have used the X2 emission whose linewidth properties had been extensively analyzed in Section 7.12(b) (Figures 7.8, 7.10). We have first filtered this emission line using the scanning Fabry-Perot interferometer in the non-scanning mode. By this way we obtained a filtered linewidth of $1 \mu eV$ (corresponds to 637 ps dephasing time) at the output of the Fabry-Perot interferometer. Despite the fact that we have been able to increase the dephasing time up to $0.3\tau_{spon}$ in this experiment, we still did not observe two-photon interference.

7.5 p-shell Excitation

As it is apparent from the previous sections, nonresonant excitation conditions reveal too large broadenings in the (charged, neutral) single excitonic emission

lines, mainly because of the interaction between the free-carriers and quantum dot carriers. To resolve this problem it is possible to locally excite a single quantum dot by its higher excited states [108] so that no free-carriers are generated during the excitation cycle. Such an excitation scheme has indeed revealed transform limited linewidth from single excitonic emission of InAs quantum dots [106].

Chapter 8

Conclusion

As pointed out many times in this thesis, during our research we found out the convenience of single self-assembled InAs quantum dots for quantum optical applications. Due to their size variations, charging effects, lattice interactions, it is rather difficult to predict individual quantum dots' properties to the utmost detail. However, as we demonstrated in this work, prototype two-level, and three-level systems exist in quantum dots, and they are experimentally easy to access with a regular cryogenic micro-photoluminescence setup. Quantum dots naturally do not have trapping requirements as atoms. In this concluding chapter we comment on some main discussions faced during this research.

8.1 Cavity-QED Experiments

Cavity-QED using quantum dots still stands as a topic in its infancy. Several problems have to be overcome before a strongly coupled microcavity - quantum dot system can be investigated. Such a strong coupling cavity-QED regime is routinely achieved in atomic cavity-QED experiments [109]. In those experiments, atoms cooled in a magneto-optical trap are dropped to a high finesse Fabry-Perot cavity, allowing for some atoms to pass through the cavity field maximum. As a result, when

passing through the field maximum, some atoms strongly interact with the cavity mode that is resonantly tuned to the atomic transition.

The first obstacle to overcome in order to achieve strong coupling using InAs quantum dots is spatial positioning of individual quantum dots. The quantum dots we are reporting in this thesis are randomly distributed in plane, with a certain adjustable density. This is not preferable for cavity-QED analysis due to the fact that the placement of the quantum dot to the field maximum is essential to observe maximum cavity - quantum dot coupling. Hence, in order to ensure the spatial overlap, quantum dots should be placed at specific locations on the sample, and the alignment of the semiconductor microcavities should be done accordingly. A next generation of quantum dots that are self-assembled in ordered fashion can be used for this purpose in future experiments [110].

A robust tuning method is also needed to tune either the quantum dot or cavity mode energies over relatively large ranges without changing the properties of the cavity and the quantum dot. In our experiments we have achieved such a tuning by changing the temperature. This method provides a limited range of ~ 3 meV tunability between 4 - 50 K. Even though the lifetime of the quantum dot transition is shown to be constant in that temperature range (Chapter 5), the linewidth of the quantum dot transition increases with increasing temperature (Chapter 7). This would cause a problem for investigating coupling to very high quality cavity modes. Better tuning methods that have weaker effects on the quantum dot and cavity properties can be investigated for this purpose. Changing the quantum dot energy by using the AC stark effect, or changing the mode energy by applying strain to the microcavity can be such solutions.

In the end of these comments on cavity-QED using quantum dots, we would like to discuss the inhibited spontaneous emission phenomenon. In our experiments, we demonstrated that quantum dots located in thin microdisks have larger lifetimes due to inhibited spontaneous emission. This was an effect we were not particularly looking for at the beginning. Our experiments revealed inhibition factors of 2 – 4

which is approximately equal to n_{GaAs} , in agreement with a radially oriented dipole located in a thin ($d < \lambda/2$) slab waveguide. We believe this inhibited spontaneous emission phenomenon is itself an interesting field of study. By making systematically smaller semiconductor structures inhibition effects can be investigated, inhibition factors as large as 80 can be expected from GaAs based semiconductors. It can even be imagined to locate the quantum dots in the middle of two conductors in order to observe inhibition factors larger than 80.

8.2 Two-Photon Interference Experiments

Our two-photon interference experiments did not reveal successful results mainly due to the large linewidths of the single excitonic emission under nonresonant excitation conditions. Large linewidths observed under nonresonant continuous wave excitation conditions can be explained by dephasing caused by free carriers. However the effect of free carriers on the linewidth is expected to be smaller under nonresonant pulsed excitation. That is mainly due to the fact that, free carriers have much smaller lifetimes than the ground state carriers, hence the recombination of ground state excitons should be less effected by those carriers. The fact that under nonresonant pulsed excitation we observed linewidths as large as the linewidths we observed under nonresonant continuous wave excitation conditions can be due to the interaction of ground state carriers with trapped charges in some nearby trap states that causes spectral diffusion of the emission lines. The fact that we have measured carrier lifetimes as large as 1 ns in the low energy states of the wetting layer supports such an explanation. Furthermore, from our two-photon interference experiments we can deduce that the states responsible for broad single-excitonic emission probably have trapping times < 10 ns. If the trapping times were larger (> 10 ns), the broad single-excitonic emission lines would probably not prevent the observation of two-photon interference phenomenon. However, we cannot disregard other possible sources that failed our two-photon interference experiments.

Bibliography

- [1] H. J. Kimble, M. Dagenais, and L. Mandel, Phys. Rev. Lett. **39**, 691 (1977).
- [2] W. Neuhauser, M. Hohenstatt, P. Toschek, and H. Dehmelt, Phys. Rev. A **22**, 1137 (1980).
- [3] F. Diedrich and H. Walther, Phys. Rev. Lett. **58**, 203 (1987).
- [4] A. Kuhn, M. Hennrich, and G. Rempe, Phys. Rev. Lett. **89**, 067901 (2002).
- [5] P. Michler, A. Imamoglu, M. D. Mason, P. J. Carson, G. F. Strouse, and S. K. Buratto, Nature(London) **406**, 968 (2000).
- [6] P. Michler, A. Kiraz, C. Becher, W. V. Schoenfeld, P. M. Petroff, L. Zhang, E. Hu, and A. Imamoglu, Science **290**, 2282 (2000).
- [7] E. Knill, R. Laflamme, and G. J. Milburn, Nature (London) **409**, 46 (2001).
- [8] M. A. Kastner, Phys. Today **72**, 24 (1993).
- [9] H. Drexler, D. Leonard, W. Hansen, J. P. Kotthaus, and P. M. Petroff, Phys. Rev. Lett. **73**, 2252 (1994).
- [10] D. Gammon, E. S. Snow, B. V. Shanabrook, D. S. Katzer, and D. Park, Science **273**, 87 (1996).
- [11] A. Zrenner, L. V. Butov, M. Hagn, G. Abstreiter, G. Böhm, and G. Weimann, Phys. Rev. Lett. **72**, 3382 (1994).

- [12] E. Dekel, D. Gershoni, E. Ehrenfreund, D. Spektor, J. M. Garcia, and P. M. Petroff, Phys. Rev. Lett. **80**, 4991 (1998).
- [13] P. M. Petroff, A. Lorke, and A. Imamoğlu, Phys. Today **54**, 46 (2001).
- [14] J. M. Garcia, G. Medeiros-Ribeiro, K. Schmidt, T. Ngo, J. L. Feng, A. Lorke, J. Kotthaus, and P. M. Petroff, Appl. Phys. Lett. **71**, 2014 (1997).
- [15] J. M. Garcia, T. Mankad, P. O. Holtz, P. J. Wellman, and P. M. Petroff, Appl. Phys. Lett. **72**, 3172 (1998).
- [16] A. Lorke, R. J. Luyken, A. O. Govorov, J. P. Kotthaus, J. M. Garcia, and P. M. Petroff, Phys. Rev. Lett. **84**, 2223 (2000).
- [17] A. Zrenner, J. of Chem. Phys. **112**, 7790 (2000).
- [18] S. Raymond, S. Fafard, P. J. Poole, A. Wojs, P. Hawrylak, S. Charbonneau, D. Leonard, R. Leon, P. M. Petroff, and J. L. Merz, Phys. Rev. B **54**, 11548 (1996).
- [19] B. Gayral, J.-M. Gérard, A. Lematre, C. Dupuis, L. Manin, and J. L. Pelouard, Appl. Phys. Lett. **75**, 1908 (1999).
- [20] P. Michler, A. Kiraz, L. Zhang, C. Becher, E. Hu, and A. Imamoğlu, Appl. Phys. Lett. **77**, 184 (2000).
- [21] H. J. Kimble and L. Mandel, Phys. Rev. A **13**, 2123 (1976).
- [22] T. Basché, W. Moerner, M. Orrit, and H. Talon, Phys. Rev. Lett. **69**, 1516 (1992).
- [23] L. Fleury, J.-M. Segura, G. Zumofen, B. Hecht, and U. P. Wild, Phys. Rev. Lett. **84**, 1148 (2000).
- [24] C. Kurtsiefer, S. Mayer, P. Zarda, and H. Weinfurter, Phys. Rev. Lett. **85**, 290 (2000).

- [25] R. Brouri, A. Beveratos, J.-P. Poizat, and P. Grangier, *Opt. Lett.* **25**, 1294 (2000).
- [26] C. Becher, A. Kiraz, P. Michler, A. Imamoglu, W. V. Schoenfeld, P. M. Petroff, L. Zhang, and E. Hu, *Phys. Rev. B* **63**, 121312(R) (2001).
- [27] V. Zwiller, H. Blom, P. Jonsson, N. Panev, S. Jeppesen, T. Tsegaye, E. Goobar, M.-E. Pistol, L. Samuelson, and G. Bjrk, *Appl. Phys. Lett.* **78**, 2476 (2001).
- [28] R. Loudon, *The quantum theory of light*, 2nd ed. (Oxford University Press, New York, 1983).
- [29] Y. Yamamoto and A. Imamoglu, *Mesoscopic Quantum Optics* (Wiley-Interscience, New York, 1999).
- [30] D. V. Regelman, U. Mizrahi, D. Gershoni, E. Ehrenfreund, W. V. Schoenfeld, and P. M. Petroff, *Phys. Rev. Lett.* **87**, 257401 (2001).
- [31] R. H. Brown and R. Q. Twiss, *Nature (London)* **178**, 1447 (1956).
- [32] E. Dekel, D. V. Regelman, D. Gershoni, E. Ehrenfreund, , W. V. Schoenfeld, and P. M. Petroff, *Phys. Rev. B* **62**, 11038 (2000).
- [33] E. Dekel, D. V. Regelman, D. G. E. Ehrenfreund, W. V. Schoenfeld, and P. M. Petroff, *Solid State Commun.* **117**, 395 (2001).
- [34] D. V. O'Connor and D. Phillips, *Time Correlated Single Photon Counting* (Academic Press, London, 1974).
- [35] D. Bouwmeester, A. Ekert, and A. Zeilinger, *The Physics of Quantum Information* (Springer, Berlin, 2000).
- [36] A. Imamoglu and Y. Yamamoto, *Phys. Rev. Lett.* **72**, 210 (1994).
- [37] C. H. Bennett and G. Brassard, *Proc. IEEE Int. Conference on Computers, Systems and Signal Processing*, 175 (IEEE, New York, 1984) .

- [38] J. Kim, O. Benson, H. Kan, and Y. Yamamoto, *Nature (London)* **397**, 500 (1999).
- [39] F. D. Martini, G. D. Giuseppe, and M. Marrocco, *Phys. Rev. Lett.* **76**, 900 (1996).
- [40] C. Brunel, B. Lounis, P. Tamarat, and M. Orrit, *Phys. Rev. Lett.* **83**, 2722 (1999).
- [41] B. Lounis and W. E. Moerner, *Nature (London)* **407**, 491 (2000).
- [42] R. Brouri, A. Beveratos, J.-P. Poizat, and P. Grangier, *Phys. Rev. A* **62**, 063817 (2000).
- [43] C. K. Law and J. H. Eberly, *Phys. Rev. Lett.* **76**, 1055 (1996).
- [44] C. K. Law and H. J. Kimble, *J. of Mod. Opt.* **44**, 2067 (1997).
- [45] A. Kuhn, M. Hennrich, T. Bondo, and G. Rempe, *Appl. Phys. B* **69**, 373 (1999).
- [46] C. Santori, M. Pelton, G. Solomon, Y. Dale, and Y. Yamamoto, *Phys. Rev. Lett.* **86**, 1502 (2001).
- [47] E. Moreau, I. Robert, J.-M. Gérard, I. Abram, L. Manin, and V. Thierry-Mieg, *Appl. Phys. Lett.* **79**, 2865 (2001).
- [48] J.-M. Gérard and B. Gayral, *IEEE J. of Lightwave Technol.* **17**, 2089 (1999).
- [49] Z. L. Yuan, B. E. Kardynal, R. M. Stevenson, A. J. Shields, C. J. Lobo, K. Cooper, N. S. Beattie, D. A. Ritchie, and M. Pepper, *Science* **295**, 102 (2002).
- [50] A. Beveratos, S. Kuhn, R. Brouri, T. Gacoin, J.-P. Poizat, and P. Grangier, *European Phys. Jour. D* **18**, 191 (2002).

- [51] A. Imamoglu, H. Schmidt, G. Woods, and M. Deutsch, Phys. Rev. Lett. **79**, 1467 (1997).
- [52] S. Raymond, K. Hinzer, S. Fafard, and J. L. Merz, Phys. Rev. B **61**, 16331(R) (2000).
- [53] O. Benson, C. Santori, M. Pelton, and Y. Yamamoto, Phys. Rev. Lett. **84**, 2513 (2000).
- [54] G. S. Solomon, M. Pelton, and Y. Yamamoto, Phys. Rev. Lett. **86**, 3903 (2001).
- [55] A. Kiraz, P. Michler, C. Becher, B. Gayral, A. Imamoglu, L. Zhang, E. Hu, W. V. Schoenfeld, and P. M. Petroff, Appl. Phys. Lett. **78**, 3932 (2001).
- [56] C. Fabre, *Confined Photon Systems, edited by H. Benisty, J.-M. Gérard, R. Houdré, J. Rarity, C. Weisbuch* (Springer, Berlin, 1999).
- [57] S. Haroche and D. Kleppner, Phys. Today **42**, 24 (1989).
- [58] Q. A. Turchette, C. J. Hood, W. Lange, H. Mabuchi, and H. J. Kimble, Phys. Rev. Lett. **75**, 4710 (1995).
- [59] A. Rauschenbeutel, G. Nogues, S. Osnaghi, P. Bertet, M. Brune, J.-M. Raymond, and S. Haroche, Science **288**, 2024 (2000).
- [60] A. Imamoglu, D. D. Awschalom, G. Burkard, D. P. DiVincenzo, D. Loss, M. Sherwin, and A. Small, Phys. Rev. Lett. **83**, 4204 (1999).
- [61] N. Schlosser, G. Reymond, I. Protsenko, and P. Grangier, Nature (London) **411**, 1024 (2001).
- [62] J.-M. Gérard, B. Sermage, B. Gayral, B. Legrand, E. Costard, and V. Thiery-Mieg, Phys. Rev. Lett. **81**, 1110 (1998).
- [63] W. Fang, J. Y. Xu, A. Yamilov, H. Cao, Y. Ma, S. T. Ho, and G. S. Solomon, Opt. Lett. **27**, 948 (2002).

- [64] L. C. Andreani, G. Panzarini, and J.-M. Gérard, *Phys. Rev. B* **60**, 13276 (1999).
- [65] E. M. Purcell, *Phys. Rev.* **69**, 681 (1946).
- [66] S. L. McCall, A. F. J. Levi, R. E. Slusher, S. J. Pearton, and R. A. Logan, *Appl. Phys. Lett.* **60**, 289 (1992).
- [67] R. E. Slusher, A. F. J. Levi, U. Mohideen, S. L. McCall, S. J. Pearton, and R. A. Logan, *Appl. Phys. Lett.* **63**, 1310 (1993).
- [68] G. Bacher, R. Weigand, J. Seufert, V. D. Kulakovskii, N. A. Gippius, A. Forchel, K. Leonardi, and D. Hommel, *Phys. Rev. Lett.* **83**, 4417 (1999).
- [69] G. Wang, S. Fafard, D. Leonard, J. E. Bowers, J. L. Merz, and P. M. Petroff, *Appl. Phys. Lett.* **64**, 2815 (1994).
- [70] J. Arlett, F. Yang, A. K. Hinter, S. Fafard, Y. Feng, S. Charbonneau, and R. Leon, *J. Vac. Sci. Technology B* **16**, 578 (1998).
- [71] A. Fiore, P. Borri, W. L. J. M. Hvam, U. Oesterle, R. Houdre, R. P. Stanley, and M. Ilegems, *Appl. Phys. Lett.* **76**, 3430 (2000).
- [72] E. S. Moskalenko, K. F. Karlsson, P. O. Holtz, B. M. W. V. Schoenfeld, J. M. Garcia, and P. M. Petroff, *Phys. Rev. B* **64**, 085302 (2000).
- [73] R. J. Warburton, C. Schafflein, D. Haft, F. Bickel, A. Lorke, K. Karrai, J. M. Garcia, W. Schoenfeld, and P. M. Petroff, *Physica E* **9**, 124 (2001).
- [74] D. Kleppner, *Phys. Rev. Lett.* **47**, 233 (1981).
- [75] E. Yablonovitch, T. J. Gmitter, and R. Bhat, *Phys. Rev. Lett.* **61**, 2546 (1988).
- [76] R. G. Hulet, E. S. Hilfer, and D. Kleppner, *Phys. Rev. Lett.* **55**, 2137 (1985).

- [77] W. Jhe, A. Anderson, E. A. Hinds, D. Meschede, L. Moi, and S. Haroche, *Phys. Rev. Lett.* **58**, 666 (1987).
- [78] W. A. Saunders, K. J. Vahala, H. A. Atwater, and R. C. Flagan, *J. Appl. Phys.* **72**, 806 (1992).
- [79] J. D. Jackson, in *Classical Electrodynamics*, 3 ed. (John Wiley and Sons, Inc., New York, 1999), Chap. 4, p. 158.
- [80] D. Y. Chu and S.-T. Ho, *J. Opt. Soc. Am. B* **10**, 381 (1993).
- [81] D. J. Heinzen, J. J. Childs, J. E. Thomas, and M. S. Feld, *Phys. Rev. Lett.* **58**, 1320 (1987).
- [82] D. J. Heinzen and M. S. Feld, *Phys. Rev. Lett.* **59**, 2623 (1987).
- [83] Y. Xu, R. K. Lee, and A. Yariv, *Phys. Rev. A* **61**, 033808 (2000).
- [84] Y. Xu, J. S. Vuckovic, R. K. Lee, O. J. Painter, A. Scherer, and A. Yariv, *J. Opt. Soc. Am. B* **16**, 465 (2000).
- [85] A. Beveratos, R. Brouri, T. Gacoin, J.-P. Poizat, and P. Grangier, *Phys. Rev. A* **64**, 061802(R) (2001).
- [86] A. Kiraz, S. Falth, C. Becher, B. Gayral, L. Z. E. Hu, W. V. Schoenfeld, P. M. Petroff, and A. Imamoglu, *Phys. Rev. B* **65**, 161303(R) (2002).
- [87] D. T. Pegg, R. Loudon, and P. L. Knight, *Phys. Rev. A* **33**, 4085 (1986).
- [88] C. Santori, G. S. Solomon, M. Pelton, and Y. Yamamoto, *Phys. Rev. B* **65**, 073310 (2002).
- [89] R. M. Thompson, R. M. Stevenson, A. J. Shields, I. Farrer, C. J. Lobo, D. A. Ritchie, M. L. Leadbeater, and M. Pepper, *Phys. Rev. B* **64**, 201302(R) (2001).

- [90] E. Moreau, I. Robert, L. Manin, V. Thierry-Mieg, J. M. Gérard, and I. Abram, Phys. Rev. Lett **87**, 183601 (2001).
- [91] D. V. Regelman, U. Mizrahi, D. Gershoni, E. Ehrenfreund, W. V. Schoenfeld, and P. M. Petroff, Phys. Rev. Lett **87**, 257401 (2001).
- [92] J. F. Clauser, Phys. Rev. D **9**, 853 (1974).
- [93] S. J. Freedman and J. F. Clauser, Phys. Rev. Lett. **28**, 938 (1972).
- [94] A. Aspect, G. Roger, S. Reynaud, J. Dalibard, and C. Cohen-Tannoudji, Phys. Rev. Lett. **45**, 617 (1980).
- [95] A. Aspect, P. Grangier, and G. Roger, Phys. Rev. Lett. **47**, 460 (1981).
- [96] A. Aspect, P. Grangier, and G. Roger, Phys. Rev. Lett. **49**, 91 (1982).
- [97] A. Aspect, J. Dalibard, and G. Roger, Phys. Rev. Lett. **49**, 1804 (1982).
- [98] M. Paillard, X. Marie, P. Renucci, T. Amand, A. Jbeli, and J. M. Gérard, Phys. Rev. Lett **86**, 1634 (2001).
- [99] C. Santori, D. Fattal, M. Pelton, G. S. Solomon, and Y. Yamamoto, cond-mat/0111242 (2001).
- [100] R. M. Stevenson, R. M. Thompson, A. J. Shields, I. Farrer, B. E. Kardynal, D. A. Ritchie, and M. Pepper, Phys. Rev. B **66**, 081302(R) (2002).
- [101] R. Ghosh and L. Mandel, Phys. Rev. Lett. **59**, 1903 (1987).
- [102] C. K. Hong, Z. Y. Ou, and L. Mandel, Phys. Rev. Lett. **59**, 2044 (1987).
- [103] L. Mandel, Rev. of Mod. Phys. **71**, S274 (1999).
- [104] J.-W. Pan, M. Daniell, S. Gasparoni, G. Weihs, and A. Zeilinger, Phys. Rev. Lett. **86**, 4435 (2001).

- [105] A. N. Boto, P. Kok, D. S. Abrams, S. L. Braunstein, C. P. Williams, and J. P. Dowling, Phys. Rev. Lett. **85**, 2733 (2000).
- [106] M. Bayer and A. Forchel, Phys. Rev. B **65**, 041308(R) (2002).
- [107] Y. Yamamoto, (Private Communication).
- [108] P. Hawrylak, G. A. Narvaez, M. Bayer, and A. Forchel, Phys. Rev. Lett. **85**, 389 (2000).
- [109] H. Mabuchi, Q. A. Turchette, M. S. Chapman, and H. J. Kimble, Opt. Lett. **21**, 1393 (1996).
- [110] H. Lee, J. A. Johnson, M. Y. He, J. S. Speck, and P. M. Petroff, App. Phys. Lett. **78**, 105 (2001).

Appendix A

Calculation of $g^{(2)}(\tau)$

In this appendix a general procedure to calculate second order correlation functions under continuous wave excitation is explained [29]. A single two-level system is investigated under little and severe dephasing conditions, then the procedure applied to a single two-level system is generalized to a general many-level emitter.

A.1 Two-Level System with Little Dephasing

Considering a general single two-level emitter that has spontaneous emission, and other dephasing mechanisms, excited nonresonantly with a small detuning (Figure A.1), the Hamiltonian of the system is:

$$\hat{H} = \hbar\omega_{eg}\hat{\sigma}_{ee} + \hbar\omega_L\hat{a}^\dagger\hat{a} + \sum_{\mathbf{k}} \hbar\omega_{\mathbf{k}}\hat{a}_{\mathbf{k}}^\dagger\hat{a}_{\mathbf{k}} + \sum_{\mathbf{k}} \hbar g_{\mathbf{k}}(\hat{a}_{\mathbf{k}}^\dagger\hat{\sigma}_{ge} + \hat{\sigma}_{eg}\hat{a}_{\mathbf{k}}) + \hbar g(\hat{a}^\dagger\hat{\sigma}_{ge} + \hat{\sigma}_{eg}\hat{a})$$

Here a and \hat{a}^\dagger represent the photon annihilation and creation operators respectively while $\hat{\sigma}_{ge} = |g\rangle\langle e|$ and $\hat{\sigma}_{eg} = |e\rangle\langle g|$ are atomic projection operators. g_k and g correspond to the coupling strength between the two-level emitter and the vacuum mode k , and the laser field respectively. \mathbf{k} is in general a vector quantity, it is reduced to k for simplicity, polarization of the vacuum modes is also contained in k . In the rotating frame, $\tilde{\sigma}_{eg} = e^{-i\omega_L t}\hat{\sigma}_{eg}$, and $\tilde{\sigma}_{ge} = e^{i\omega_L t}\hat{\sigma}_{ge}$ after using the Markov approximation, considering a classical single mode laser field ($\gamma_L \ll \gamma_{tot}, \Gamma_{spont}$) the

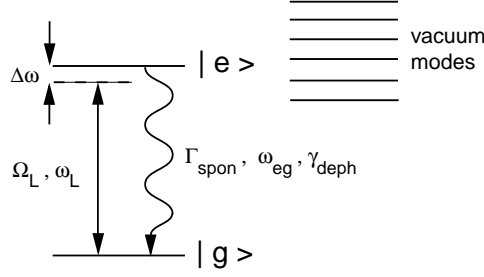


Figure A.1: Laser driven two-level emitter

time evolution of the system operators are given as:

$$\begin{aligned} \frac{d}{dt} \begin{bmatrix} \tilde{\sigma}_{eg}(t) \\ \hat{\sigma}_{ee}(t) - \hat{\sigma}_{gg}(t) \\ \tilde{\sigma}_{ge}(t) \end{bmatrix} &= \begin{bmatrix} i\Delta w - \gamma_{tot} & -i\frac{\Omega_L}{2} & 0 \\ -i\Omega_L & -\Gamma_{spon} & i\Omega_L \\ 0 & i\frac{\Omega_L}{2} & -i\Delta w - \gamma_{tot} \end{bmatrix} \begin{bmatrix} \tilde{\sigma}_{eg}(t) \\ \hat{\sigma}_{ee}(t) - \hat{\sigma}_{gg}(t) \\ \tilde{\sigma}_{ge}(t) \end{bmatrix} \\ &+ \begin{bmatrix} f^\dagger(t) \\ 2g(t) - \Gamma_{spon} \\ f(t) \end{bmatrix} \end{aligned} \quad (\text{A.1.1})$$

where $\Delta w = w_{eg} - w_L$, $\gamma_{tot} = \frac{\Gamma_{spon}}{2} + \gamma_{deph}$, and $\hbar\Omega_L = 2\hbar g = 2\langle \mathbf{e} | \mathbf{r} \cdot \mathbf{D} \rangle = 2|\mu_{eg} \cdot \epsilon||E_{max}|$ denote laser detuning, coherence dephasing rate, and the Rabi frequency respectively. $\mu_{eg} = \langle e | \mathbf{r} | g \rangle$ is the dipole matrix element, E_{max} maximum field intensity per photon, and ϵ field polarization vector. The functions $f(t)$, and $g(t)$ correspond to fluctuation terms as a result of the dissipation induced by the spontaneous emission. $f(t)$, $g(t)$, and Γ_{spon} are given by:

$$\begin{aligned} f(t) &= -i \sum_k g_k \hat{a}_k(0) (\hat{\sigma}_{gg}(t) - \hat{\sigma}_{ee}(t)) e^{-i(w_k - w_l)t} \\ g(t) &= i \sum_k g_k \hat{a}_k^\dagger(0) \tilde{\sigma}_{ge}(t) e^{i(w_k - w_l)t} - i \sum_k g_k \tilde{\sigma}_{eg}(t) \hat{a}_k(0) e^{-i(w_k - w_l)t} \\ \frac{\Gamma_{spon}}{2} &= \sum_k g_k^2 \int_{-\infty}^t dt' e^{i(w_k - w_l)(t-t')} \end{aligned}$$

Equation A.1.1 reduces to the Bloch equations when the average over the dissipative modes is taken, using $\langle f(t) \rangle = \langle g(t) \rangle = 0$:

$$\begin{aligned} \frac{d}{dt} \begin{bmatrix} \langle \tilde{\sigma}_{eg}(t) \rangle \\ \langle \hat{\sigma}_{ee}(t) \rangle - \langle \hat{\sigma}_{gg}(t) \rangle \\ \langle \tilde{\sigma}_{ge}(t) \rangle \end{bmatrix} &= \begin{bmatrix} i\Delta w - \gamma_{tot} & -i\frac{\Omega_L}{2} & 0 \\ -i\Omega_L & -\Gamma_{spon} & i\Omega_L \\ 0 & i\frac{\Omega_L}{2} & -i\Delta w - \gamma_{tot} \end{bmatrix} \begin{bmatrix} \langle \tilde{\sigma}_{eg}(t) \rangle \\ \langle \hat{\sigma}_{ee}(t) \rangle - \langle \hat{\sigma}_{gg}(t) \rangle \\ \langle \tilde{\sigma}_{ge}(t) \rangle \end{bmatrix} \\ &+ \begin{bmatrix} 0 \\ -\Gamma_{spon} \\ 0 \end{bmatrix} \end{aligned} \quad (\text{A.1.2})$$

The unnormalized second order correlation function $G^{(2)}(\tau) = \langle \hat{\sigma}_{eg}(t') \hat{\sigma}_{ee}(t' + \tau) \hat{\sigma}_{ge}(t') \rangle$ can be obtained from Equation A.1.1 by multiplying with $\hat{\sigma}_{eg}(t')$ from left and $\hat{\sigma}_{ge}(t')$ from right, and taking the average over all dissipative modes. Quantum Regression Theorem reveals $\langle \hat{\sigma}_{eg}(t') f(t) \hat{\sigma}_{ge}(t') \rangle = \langle \hat{\sigma}_{eg}(t') g(t) \hat{\sigma}_{ge}(t') \rangle = 0$. Introducing the variable $\tau = t - t'$, the equation becomes:

$$\begin{aligned} \frac{d}{d\tau} \begin{bmatrix} \tilde{G}_{eg}(\tau) \\ G_{ee}(\tau) - G_{gg}(\tau) \\ \tilde{G}_{ge}(\tau) \end{bmatrix} &= \begin{bmatrix} i\Delta w - \gamma_{tot} & -i\frac{\Omega_L}{2} & 0 \\ -i\Omega_L & -\Gamma_{spon} & i\Omega_L \\ 0 & i\frac{\Omega_L}{2} & -i\Delta w - \gamma_{tot} \end{bmatrix} \begin{bmatrix} \tilde{G}_{eg}(\tau) \\ G_{ee}(\tau) - G_{gg}(\tau) \\ \tilde{G}_{ge}(\tau) \end{bmatrix} \\ &+ \begin{bmatrix} 0 \\ -\Gamma_{spon} \langle \hat{\sigma}_{ee}(t') \rangle \\ 0 \end{bmatrix} \end{aligned} \quad (\text{A.1.3})$$

in the above equations

$$\begin{aligned} \tilde{G}_{eg}(\tau) &= \langle \hat{\sigma}_{eg}(t') \tilde{\sigma}_{eg}(t) \hat{\sigma}_{ge}(t') \rangle \\ G_{ee}(\tau) - G_{gg}(\tau) &= \langle \hat{\sigma}_{eg}(t') (\hat{\sigma}_{ee}(t) - \hat{\sigma}_{gg}(t)) \hat{\sigma}_{ge}(t') \rangle \\ \tilde{G}_{ge}(\tau) &= \langle \hat{\sigma}_{eg}(t') \tilde{\sigma}_{ge}(t) \hat{\sigma}_{ge}(t') \rangle \end{aligned}$$

Assuming that the correlation functions are calculated after the system reached its steady state, in Equation A.1.3 $\langle \hat{\sigma}_{ee}(t') \rangle$ can be replaced by its steady-state value, and the initial values for the equation are (at $t=t'$):

$$\begin{aligned} \tilde{G}_{eg}(\tau = 0) &= \langle \hat{\sigma}_{ee}(t') \rangle \\ G_{ee}(\tau = 0) - G_{gg}(\tau = 0) &= 0 \\ \tilde{G}_{ge}(\tau = 0) &= 0 \end{aligned}$$

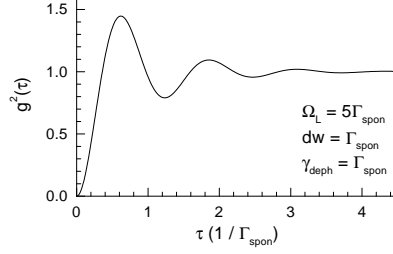


Figure A.2: Photon antibunching in resonance fluorescence

$G^{(2)}(\tau) = G_{ee}(\tau) = \langle \hat{\sigma}_{eg}(t') \hat{\sigma}_{ee}(t'+\tau) \hat{\sigma}_{ge}(t') \rangle$ can then be calculated using the solution for $G_{ee}(\tau) - G_{gg}(\tau)$ and the closed system relationship:

$$\langle \hat{\sigma}_{ee}(t) \rangle + \langle \hat{\sigma}_{gg}(t) \rangle = 1 \Rightarrow G_{ee}(\tau) + G_{gg}(\tau) = \langle \hat{\sigma}_{ee}(t') \rangle.$$

An exemplary simulation of Equation A.1.3 is shown in Figure A.2. In that Figure, due to the coherent nature of the excitation, Rabi oscillations are apparent together with the dip around $\tau = 0$ which is the signature of photon antibunching.

A.2 Dephased Two-Level System

For a two-level system in which coherence dephasing rates are much larger than the Rabi frequency ($\gamma_{tot} \gg \Omega_L$), $\frac{d\tilde{\sigma}_{eg}(t)}{dt} = \frac{d\tilde{\sigma}_{ge}(t)}{dt} \approx 0$, the Bloch equations become simple rate equations:

$$\frac{d}{dt} \begin{bmatrix} \langle \hat{\sigma}_{ee}(t) \rangle \\ \langle \hat{\sigma}_{gg}(t) \rangle \end{bmatrix} = \begin{bmatrix} -\Gamma_{spon} - \frac{\Omega_L^2}{\gamma_{tot}} & \frac{\Omega_L^2}{\gamma_{tot}} \\ \Gamma_{spon} + \frac{\Omega_L^2}{\gamma_{tot}} & -\frac{\Omega_L^2}{\gamma_{tot}} \end{bmatrix} \begin{bmatrix} \langle \hat{\sigma}_{ee}(t) \rangle \\ \langle \hat{\sigma}_{gg}(t) \rangle \end{bmatrix} \quad (\text{A.2.1})$$

After application of quantum regression theorem as in Section A.1, the differential equation for $G^{(2)}(\tau)$ reads:

$$\frac{d}{dt} G^{(2)}(\tau) = -(\Gamma_{spon} + \frac{\Omega_L^2}{\gamma_{tot}}) G^{(2)}(\tau) + \frac{\Omega_L^2}{2\gamma_{tot}} \langle \hat{\sigma}_{ee}(t') \rangle$$

substituting $\langle \hat{\sigma}_{ee}(t') \rangle = \langle \hat{\sigma}_{ee}(t') \rangle_{ss} = \frac{\frac{\Omega_L^2}{2\gamma_{tot}}}{\Gamma_{spon} + \frac{\Omega_L^2}{\gamma_{tot}}}$ solving for the initial condition $G^{(2)}(\tau = 0) = 0$, the normalized second order correlation function is found to be:

$$g^{(2)}(\tau) = 1 - e^{-(\Gamma_{spon} + \frac{\Omega_L^2}{\gamma_{tot}})\tau}$$

A.3 Comments on the Calculation of Second Order Correlation Functions

The general procedure outlined in previous sections can also be applied to a general single emitter that has more than two-levels. It suffices to write the Bloch equations for a non-dephased emitter, or rate equations for a dephased emitter, and then obtain the correlation functions by multiplying from left and right with appropriate density matrix elements using the quantum regression theorem, and solve the new set of equations by substituting the initial conditions for density matrix elements with their steady state values, under the condition that the system has been turned on for long enough period of time. Hence, for a general dephased system, the problem becomes the analysis of the evolution of the system from the ground level up to its steady state, the relevant time scales are therefore the recovery times of the system from the ground state.

Appendix B

Jaynes-Cummings Hamiltonian

In this appendix the basic properties of the strong coupling between a two-level emitter and a cavity mode are discussed under the idealized conditions that assumes no cavity decay and no spontaneous emission. The Hamiltonian of the system to be studied is (Figure 5.1):

$$\hat{H} = \hbar\omega_{eg}\hat{\sigma}_{ee} + \hbar\omega_c\hat{a}^\dagger\hat{a} - i\hbar g(\hat{\sigma}_{eg}\hat{a} + \hat{a}^\dagger\hat{\sigma}_{ge}) \quad (\text{B.0.1})$$

which is the Jaynes-Cummings Hamiltonian. The coupling constant g is given as: $\hbar g = \frac{\hbar\Omega_c}{2} = \langle e|\mathbf{r} \cdot \mathbf{D}\rangle = |\mu_{eg} \cdot \epsilon||E_{max}|$, where $\mu_{eg} = \langle e|\mathbf{r}|g\rangle$ is the dipole matrix element, E_{max} maximum field intensity per photon, and ϵ field polarization vector. In the remaining part of this appendix we solve for the Rabi oscillations and normal mode splitting phenomena which are the main signatures of a strongly coupled dipole - cavity system, we also introduce the *dressed state* formalism. At the end of the appendix we also introduce the AC Stark effect.

B.1 Rabi Oscillations

In order to see the Rabi oscillations, it is convenient to start from the eigenfunctions of the noninteracting part of the Jaynes-Cummings hamiltonian. These

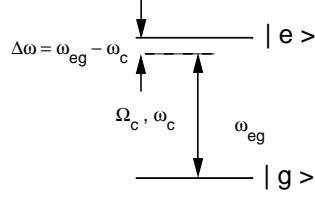


Figure B.1: Strongly coupled dipole and a cavity mode

eigenfunctions are $|g, n\rangle$, and $|e, n\rangle$ and they are called the *bare* states. The interaction hamiltonian:

$$\hat{H}_{int} = -i\hbar g(\hat{\sigma}_{eg}\hat{a} + \hat{a}^\dagger\hat{\sigma}_{ge})$$

gives nonzero matrix elements $\langle i|\hat{H}_{int}|j\rangle$ only between the eigenstates $|g, n+1\rangle$, and $|e, n\rangle$ for $n=0,1,2,\dots$. Hence in an energy level diagram as shown in Figure B.2 only the states at the same manifold are coupled with each other. Starting from the time-dependent wave function:

$$|\psi(t)\rangle = a_n(t)e^{-i(n\omega_c + \omega_{eg})t}|e, n\rangle + b_n(t)e^{-i(n+1)\omega_{ct}}|g, n+1\rangle \quad (\text{B.1.1})$$

Substituting Equation B.1.1 into Schrödinger equation, coupled amplitude equations below are obtained:

$$\begin{aligned} i\hbar \frac{d}{dt} \begin{bmatrix} a_n(t) \\ b_n(t) \end{bmatrix} &= \begin{bmatrix} 0 & e^{i\Delta\omega t} \langle e, n | \hat{H}_{int} | g, n+1 \rangle \\ e^{-i\Delta\omega t} \langle g, n+1 | \hat{H}_{int} | e, n \rangle & 0 \end{bmatrix} \begin{bmatrix} a_n(t) \\ b_n(t) \end{bmatrix} \\ &= \begin{bmatrix} 0 & -ie^{i\Delta\omega t} \hbar g \sqrt{n+1} \\ ie^{-i\Delta\omega t} \hbar g \sqrt{n+1} & 0 \end{bmatrix} \begin{bmatrix} a_n(t) \\ b_n(t) \end{bmatrix} \end{aligned}$$

where $\Delta\omega = \omega_{eg} - \omega_c$. Switching to the rotating frame $\tilde{a}_n(t) = a_n(t)e^{-i\frac{\Delta\omega}{2}t}$, and $\tilde{b}_n(t) = b_n(t)e^{i\frac{\Delta\omega}{2}t}$, the equations become:

$$\frac{d}{dt} \begin{bmatrix} \tilde{a}_n(t) \\ \tilde{b}_n(t) \end{bmatrix} = \begin{bmatrix} -i\frac{\Delta\omega}{2} & -g\sqrt{n+1} \\ g\sqrt{n+1} & i\frac{\Delta\omega}{2} \end{bmatrix} \begin{bmatrix} \tilde{a}_n(t) \\ \tilde{b}_n(t) \end{bmatrix}$$

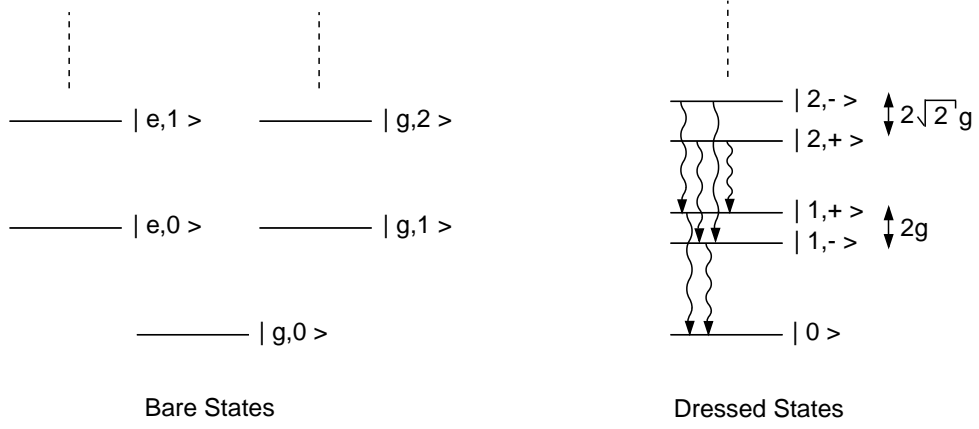


Figure B.2: Bare states and dressed states picture

These equations have the sinusoidal solution for the arbitrary initial conditions $a_n(0) = 1$, $b_n(0) = 0$:

$$\begin{aligned}\tilde{a}_n(t) &= \cos(\Omega_n t) \\ \tilde{b}_n(t) &= \sin(\Omega_n t)\end{aligned}$$

where

$$\Omega_n = \sqrt{\left(\frac{\Delta\omega}{2}\right)^2 + g^2(n+1)} \quad (\text{B.1.2})$$

Hence, in each manifold Rabi oscillations with angular frequency equal to Ω_n is observed. In the special case, when the average number of photons in the cavity mode is less than 1, the Rabi oscillations are called *vacuum Rabi oscillations*.

B.2 Normal Model Splitting

In the strong coupling regime, the eigenenergies of each manifold is split by a certain value. This can be analyzed by diagonalizing the Jaynes-Cummings

hamiltonian. Starting from the bare states of the n^{th} manifold given in Equation B.1.1, and once more introducing the rotating frame $\tilde{a}_n(t) = a_n(t)e^{-i\frac{\Delta\omega}{2}t}$, and $\tilde{b}_n(t) = b_n(t)e^{i\frac{\Delta\omega}{2}t}$:

$$\begin{aligned} \hat{H}|\psi(t)\rangle &= E_n|\psi(t)\rangle \\ \Rightarrow \begin{bmatrix} \hbar(n\omega_c + \frac{\omega_{eg} + \omega_c}{2} + \frac{\Delta\omega}{2}) & \hbar g\sqrt{n+1} \\ \hbar g\sqrt{n+1} & \hbar(n\omega_c + \frac{\omega_{eg} + \omega_c}{2} - \frac{\Delta\omega}{2}) \end{bmatrix} \begin{bmatrix} \tilde{a}_n(t) \\ \tilde{b}_n(t) \end{bmatrix} &= E_n \begin{bmatrix} \tilde{a}_n(t) \\ \tilde{b}_n(t) \end{bmatrix} \\ \Rightarrow E_{n\pm} &= E_{n0} \pm \hbar\Omega_n \end{aligned}$$

where Ω_n is the Rabi frequency given in Equation B.1.2, and $E_{n0} = \hbar(n\omega_c + \frac{\omega_{eg} + \omega_c}{2})$. Giving the general eigenfunctions:

$$\begin{aligned} |n+\rangle &= \sin\theta_n|e, n\rangle + \cos\theta_n|g, n+1\rangle \\ |n-\rangle &= \cos\theta_n|e, n\rangle - \sin\theta_n|g, n+1\rangle \end{aligned}$$

where:

$$\begin{aligned} \cos 2\theta_n &= -\frac{\Delta\omega}{2\Omega_n} \\ \sin 2\theta_n &= \frac{g\sqrt{n+1}}{\Omega_n} \end{aligned}$$

for $\Delta\omega = 0$ the eigenfunctions reduce to:

$$\begin{aligned} |n+\rangle &= \frac{1}{\sqrt{2}}(|e, n\rangle + |g, n+1\rangle) \\ |n-\rangle &= \frac{1}{\sqrt{2}}(|e, n\rangle - |g, n+1\rangle) \end{aligned}$$

B.3 AC Stark Effect

We can replace the cavity field in the previous sections by a laser field, and analyze the AC Stark effect in resonance fluorescence. This is the effect of changing the emission energy of a two-level system by a nonresonant intense laser field. Its

analysis relies on the energy eigenvalues of the Jaynes-Cummings Hamiltonian. For the 0^{th} manifold in the dressed atom picture:

$$E_{\pm} = E_{middle} \pm \hbar\Omega_0$$

where $E_{middle} = \hbar(\frac{\omega_{eg} + \omega_L}{2})$, and $\Omega_0 = \sqrt{\left(\frac{\Delta\omega}{2}\right)^2 + g^2}$. For large detunings, $\frac{\Delta\omega}{2} \gg g$, the energy eigenvalues are approximately equal to:

$$\begin{aligned} E_+ &= \hbar\left(\omega_{eg} + \frac{2g^2}{\Delta\omega^2}\right) \\ E_- &= \hbar\omega_L \end{aligned}$$

Hence the two-level system's transition energy is increased by $\frac{2g^2}{\Delta\omega^2}$, which is called the AC Stark shift.